Soft Matter

A long side chain imidazolium-based graft-type anion-exchange membrane: novel electrolyte and alkaline-durable properties and structural elucidation using SANS contrast variation

Journal:	*Soft Matter*
Manuscript ID	SM-ART-05-2020-000947.R1
Article Type:	Paper
Date Submitted by the Author:	20-Jul-2020

Complete List of Authors:	Zhao, Yue; National institute for quantum and radiological science and technology, Department of Advanced Functional Materials Research Yoshimura, Kimio; Japan Atomic Energy Agency, Mahmoud, Ahmed; National Institutes for Quantum and Radiological Science and Technology Takasaki Advanced Radiation Research Institute, Department of Advanced Functional Materials Research; Clean Energy Research Center, Yamanashi , Japan, functional Polymer materials for fuel cells Yu, Hwan-Chul; National Institutes for Quantum and Radiological Science and Technology Takasaki Advanced Radiation Research Institute, Department of Advanced Functional Materials Research Okushima, Shun; National Institutes for Quantum and Radiological Science and Technology Takasaki Advanced Radiation Research Institute, Department of Advanced Functional Materials Research Hiroki, Akihiro; Kokuritsu Kenkyu Kaihatsu Hojin Ryoshi Kagaku Gijutsu Kenkyu Kaihatsu Kiko, Department of Advanced Functional Materials Research Kishiyama, Yoshihiro; Daihatsu Kogyo Kabushiki Kaisha Shiga Ryuo Kojo Shishitani, Hideyuki; Daihatsu Kogyo Kabushiki Kaisha Shiga Ryuo Kojo Yamaguchi, Susumu; Daihatsu Kogyo Kabushiki Kaisha Shiga Ryuo Kojo Tanaka, Hirohisa; Kansei Gakuin Daigaku, Nanotechnology for Sustainable Energy Noda, Yohei; Ibaraki University Koizumi, Satoshi; Comprehensive Research Organization for Science and Society (CROSS), Research Center for Neutron Science & Technology; Ibaraki University College of Engineering, Radulescu, Aurel; Forschungszentrum Jülich GmbH, Institut für Festkörperforschung Maekawa, Yasunari; QST, Department of Advanced Functional Materials Research

A long side chain imidazolium-based graft-type anion-exchange membrane: novel electrolyte and alkaline-durable properties and structural elucidation using SANS contrast variation

Yue Zhao,[1,*] Kimio Yoshimura,[1] Ahmed Mohamed Ahmed Mahmoud,[1] Hwan-Chul Yu,[1] Shun Okushima,[1] Akihiro Hiroki,[1] Yoshihiro Kishiyama,[2] Hideyuki Shishitani,[2] Susumu Yamaguchi,[2] Hirohisa Tanaka,[3] Yohei Noda,[4] Satoshi Koizumi,[4] Aurel Radulescu,[5] Yasunari Maekawa[1,*]

[1]*Department of Advanced Functional Materials Research, Takasaki Advanced Radiation Research Institute, National Institutes for Quantum and Radiological Science and Technology (QST), Watanuki-machi 1233, Takasaki, Gunma, 370-1292, Japan*
[2]*Daihatsu Motor Co., Ltd., Ryuo Gamo, Shiga 520-2593, Japan*
[3]*School of Science and Technology, Kwansei Gakuin University, 2-1 Gakuen, Sanda, Hyogo 669-1337 Japan*
[4]*Department of Engineering, Ibaraki University, Hitachi 316-8511, Japan*
[5]*Forschungszentrum Jülich GmbH, Jülich Centre for Neutron Science @ MLZ, Lichtenbergstraße 1, D-85747 Garching, Germany*

*To whom all correspondence should be addressed: Yue Zhao (zhao.yue@qst.go.jp); Yasunari Maekawa (maekawa.yasunari@qst.go.jp)

ABSTRACT: Newly designed styrylimidazolium-based grafted anion-exchange membranes (StIm-AEMs), in which imidazolium ionic groups are attached to styrene at the far side from the graft chains, were prepared by radiation-induced graft polymerization of *p*-(2-imidazoliumyl) styrene onto poly(ethylene-*co*-tetrafluoloethylene) (ETFE) films, followed by *N*-alkylation and ion-exchange reactions. StIm-AEM having an ion exchange capacity (IEC) of 0.54 mmol/g with a grafting degree (GD) of ~18%, possesses practical conductivity (>50 mS/cm) even with a very low water uptake (~10%) and high stability over 600 h in a 1-M KOH solution at 80°C. There exists a critical IEC (IEC_c) in the range of 0.7–0.8 mmol/g over which the membrane showed high water uptake, which resulted in pronounced susceptibility to hydrolysis. Using small-angle neutron scattering technique with a contrast variation method, we found the hydrophilic phase in StIm-AEMs with IECs lower and higher than IEC_c shows "reverse-micelles" with water domains dispersed in the polymer matrix and "micelles" with graft polymer aggregates dispersed in the water matrix, respectively. The further analysis of micelle structures using the hard-sphere liquid model and Porod limit analysis reveals that the interfacial structures of ionic groups are essential for the electrochemical properties and durability of StIm-AEMs. In addition, StIm-AEM with an IEC of 0.95 mmol/g and the maximum power density of 80 mW/cm^2 in the hydrazine hydrate fuel cell test, exhibited long-term durability under constant current (8.0 mA) up to 455 h, which, thus far, is the best durability at 80°C for platinum-free alkaline-type liquid fuel cells.

I. Introduction

Anion-exchange membrane (AEM) fuel cells represent a new generation of potentially disruptive, low-temperature fuel cell technology with the potential to eliminate the high-cost barriers of mainstream proton exchange membrane (PEM) fuel cells.[1-13] However, the performance of AEM fuel cells is not as good as that of PEM fuel cells, especially the membrane conductivity and long-term durability. The knowledge of AEM materials is still limited, including molecular design, hierarchical structures in the membrane, and structure/property relationships.[8-13]

To fabricate AEMs, a radiation grafting technique is a promising method. It allows to introduce many ion-conducting groups (as graft polymers to achieve high ion conductivity) into mechanically and thermally stable polymer base films with the retention of the original properties of these polymers.[14-28] In the past years, we intensively developed both AEMs and PEMs that were based on fluorinated polymers or fully aromatic hydrocarbon polymer films using this method.[15–21] Recently, we applied the radiation grafting method to prepare imidazolium-type AEMs on poly(ethylene-*co*-tetrafluoroethylene) (ETFE) base films. AEMs exhibited lower water uptake (WU) and higher alkaline stability than the corresponding AEMs containing trimethylammonium hydroxide owing to the low basicity of imidazolium hydroxide as an Arrhenius base.[8-10] Furthermore, AEMs containing weak base imidazolium groups induced low damage to polymer backbones through self-base-catalyzed degradation.[10] To suppress β-elimination and ring-opening hydrolysis of imidazolium groups,[17] we improved AEMs by grafting 2-methyl-*N*-vinylimidazole (Im), which has a methyl-protecting group at the imidazole C-2 position and co-grafting with hydrophobic styrene (St) into ETFE to obtain Im/St-AEMs.[17-21]

We investigated detailed structures and interplay between the structure and properties of these Im/St-AEMs in our latest work using the small-angle neutron scattering (SANS) technique with a contrast variation method.[18, 20] The main structural features were summarized

as follows. (1) The membranes can be characterized as a "conducting/non-conducting two-phase" system, as illustrated in Scheme 1. The conducting phase is composed of water and the majority of graft polymers where both Im and St units are covalently bonded to each other and behave coordinately. The non-conducting phase is made of ETFE chains, and the rest parts of graft polymers are constrained in amorphous ETFE domains. This model allows to evaluate the distribution of graft polymers in both conducting and non-conducting phases in a quantitative manner and is generally applicable for grafted polymer materials. (2) AEMs containing grafts with low hydrophobicity (*i.e.*, low St content) exhibit a homogeneous conducting phase with hydrated dispersed ions; thus, conductivity increases with an increase in the hydration level. In contrast, AEMs containing graft polymers with more hydrophobic units (St) exhibit a heterogeneous conducting phase, in which 3–4-nm in diameter water puddles are dispersed in the hydrophilic water/graft polymer phase. It was also determined that anion transport and membrane alkaline durability were suppressed by the water puddle structure.[21] Therefore, an increase in the hydrophobicity of graft polymers introduces the morphological transition from a homogeneous to heterogeneous conducting phase, and the resultant water puddles enhance β-elimination and hydrolysis degradation reactions.[21]

To further improve alkaline durability, in this study, we design a new molecular structure, styrylimidazolium (StIm), in which imidazolium groups are connected with St groups in perpendicular orientations, as shown in Scheme 2. This molecular design satisfies the complete removal of β-elimination reactions and hydrolysis of imidazolium rings. Contrary to the parallelly arranged Im and St groups in previous copolymer-type Im/St-AEMs, new AEMs are expected to have a clear phase separation between hydrophilic cationic headgroups and hydrophobic graft polymer chains, which may efficiently reduce WU and hydrolysis reaction. Because the ion-exchange capacity (IEC) of AEMs is the most crucial parameter, which determines their properties (e.g., conductivity, WU, mechanical strength, and durability), we systematically prepared a series of AEMs containing different GDs, which almost linearly

correspond to IEC, to investigate electrochemical properties and durability of AEMs and to elucidate the relationship between these properties and hierarchical structures of the membranes. Such studies are important and relevant to establish improved design rules for fuel cell membranes.

II. Experimental details

II-1 Materials

ETFE films [Tefzel 100LZ, mass density (d_{ETFE}) = 1.7 g/cm^3, crystallinity (X_c) = 0.36] with a thickness of 25 μm were purchased from DuPont and used as a base film. Iodopropane was purchased from Tokyo Chemical Industry Co., Ltd. Sodium hydride (50–72% in oil), St, hexane, *N,N*-dimethylformamide (DMF), ethanol, potassium carbonate (K_2CO_3), potassium hydroxide (KOH), hydrochloric acid (HCl), and a 0.1 mol/L sodium hydroxide solution (NaOH) were purchased from Wako Pure Chemical Industries, Ltd. These chemicals were used without further purification. 1,4-Dioxane and dichloromethane (CH_2Cl_2) were obtained from Kishida Chemical Co., Ltd. Deuterated water (99.9 atom% D) was purchased from Sigma-Aldrich Co. Ltd. Water used in experiments was purified using a Millipore Milli-Q UV system and had a resistance of 18.2 MΩ cm and the total organic carbon content of <10 ppb.

II-2 Preparation of AEMs

2-(4-Ethenylphenyl)-1*H*-imidazole was prepared according to the literature.[29] Sodium hydride in oil (1.32 g, 31.5 mmol) was washed with hexane (2 mL × 2) in a two-necked round bottom flask (100 mL) under nitrogen atmosphere. Then, DMF (20 mL) was added to the flask. 2-(4-Ethenylphenyl)-1*H*-imidazole (5.10 g, 30.0 mmol) was slowly added with a spatula over 10 min under stirring. The resultant solution was stirred for 30 min at room temperature; then, iodopropane (5.18 g, 30.5 mmol) in DMF (5 mL) was injected via syringe for 10 min. After additional 16 h of stirring at room temperature, the solution was quenched by water (15 mL). The aqueous layer was saturated with K_2CO_3 and extracted with CH_2Cl_2 (200 mL × 2). The extract was dried over magnesium sulfate (10 g). After CH_2Cl_2 was evaporated, the obtained

brown oil was dissolved in hexane (400 mL) and passed through Celite® Hyflo Supercel to obtain pure 2-(4-ethenylphenyl)-*N*-propylimidazole (StIm) as an orange-colored oil (4.78 g, 75% yield).

ETFE films (5.0 cm × 5.0 cm) were put in a Schlenk tube and irradiated using a ^{60}Co γ-ray source (QST Takasaki, Gunma, Japan) at room temperature in argon atmosphere with a total dose of 50 kGy at the dose rate of 10 kGy h^{-1}. Pre-irradiated ETFE films were immediately immersed in argon-purged monomer solutions (7 mL) consisting of StIm in 1,4-dioxane (50 wt%), followed by heating under argon atmosphere at 60°C for 0.67 to 16 h. Grafted ETFE was taken out, washed three times using 100 mL of 1,4-dioxane at room temperature, and refluxed in 200 mL of ethanol for 2 h to extract residual monomers and homopolymers. The obtained films were dried under vacuum at 80°C for 4 h.

For *N*-alkylation, grafted films were immersed in a 1-M dioxane solution of iodopropane (120 mL) at 60°C for 24 h. The films were washed several times using 30 mL of dioxane. Then, the films were immersed in 120 mL of a 1-M HCl/dioxane solution (50/50 vol%) to be transform from iodide (I^-) to chloride (Cl^-) forms. The solution was replaced three times every hour to ensure the completion of the ion-exchange reaction. The films were removed from the solution and washed using deionized water. Finally, the films were dried in a vacuum oven at 80°C for 24 h.

Then, AEMs in the chloride form were soaked in a 1-M KOH aqueous solution (100 mL) at room temperature for 6 h or in a 1-M $NaHCO_3$ aqueous solution (100 mL) to replace chloride (Cl^-) in the film to hydroxide (OH^-) and (HCO_3^-).[17-21] The molecular structure of graft polymers was confirmed by ^{13}C solid-state NMR spectroscopy, as shown in Figure S1 in the Supporting Information.

ETFE-based benzyltrimethylammonium (BTMA) ionomer for fuel cell performance test was prepared as follows: The pre-irradiated ETFE film was first immersed in argon-purged chloromethylstyrene solution (50% v/v in xylene) at 60 °C for 16h. The grafted films were

washed with toluene several times and dried under vacuum, and then immersed in trimethylamine (40 wt%) solution at room temperature for 24h to obtain quaternized BTMA in chloride form.

II-3. Characterization of AEMs

The completion of ion-exchange reactions was confirmed by monitoring iodide atoms of graft-type AEMs along the cross-sectional direction using a scanning electron microscopy (SEM, JEOL, JSM-5600) instrument equipped with an energy dispersive X-ray analyzer (EDX). Solid-state ^{13}C cross polarization/magic angle spinning (MAS) NMR experiments were performed using a Bruker AVANCE 300 spectrometer at the operating frequency of 75.5 MHz. The samples were packed as powders in a ZrO_2 rotor with a diameter of 4 mm. The MAS frequency was set to 10 kHz, and the sample temperature was 25°C. A total of 15−20K scans were collected in the spectral width of 23 kHz with a recycle delay of 5 s. All spectra were obtained at the cross polarization time of 2 ms through broadband proton decoupling. The spectra were externally referenced to glycine (176.0 ppm).

The GD of AEM was estimated from the weight change in grafted films by the following equation:

$$GD(\%) = \frac{W_g - W_0}{W_0} \times 100\% \qquad (1)$$

where w_0 and w_g are the weights of membranes before and after grafting in the dry state, respectively.

The IEC of AEM was determined using a standard back titration method. The membrane in the OH^- form was immersed in 15 mL of a 0.1-N HCl solution (V_{ref}, mL) for 24 h. Then, the solution was titrated with a standard NaOH (0.1 N) solution (V_{mem}, mL) to pH = 7.0 by an automatic titrator (HIRANUMA COM-555). Subsequently, the membranes were washed and immersed in deionized water for 24 h to remove residual HCl and then dried under vacuum at 50°C overnight and weighed to determine dry masses in the Cl^- form. The experimental IEC

(IEC_{exp}) value was calculated using the following equation:

$$IEC_{exp} = C \times (V_{ref} - V_{mem}) / W_{dry} \qquad (2)$$

where C is the concentration of the NaOH solution, and W_{dry} is the mass of dry AEMs.[17–21]

The WU of AEM was calculated by the weight measurements using the following equation:

$$WU(\%) = \frac{W_{wet} - W_{dry}}{W_{dry}} \times 100\% \qquad (3)$$

where W_{wet} represents the weight of AEM in the hydrated state. To measure WU, AEM was completely hydrated in water and lightly wiped with Kimwipes to remove excess water on the surface before weighing. The hydration number (λ_w) was calculated by WU and IEC_{exp} using the following equation:

$$\lambda_w = \frac{10WU}{M_w IEC_{exp}} \qquad (4)$$

where M_w (18 g/mol) is the molecular weight of water. Thus, the total water volume fraction (ϕ_w) of wet AEM can be calculated by equation (5).

$$\phi_w = \frac{\frac{WU/100(1+GD/100)}{d_w}}{\frac{1}{d_{ETFE}} + \frac{GD/100}{d_{graft}} + \frac{WU/100(1+GD/100)}{d_w}} \qquad (5)$$

where d_w and d_{graft} are the mass density of water and the graft chains, both of which are approximately 1.0 g/cm^3. Similarly, the volume fractions of ETFE ($\phi_{ETFE} = \frac{\frac{1}{d_{ETFE}}}{\frac{1}{d_{ETFE}} + \frac{GD/100}{d_{graft}} + \frac{WU/100(1+GD/100)}{d_w}}$) and grafts ($\phi_{graft} = \frac{\frac{GD/100}{d_{graft}}}{\frac{1}{d_{ETFE}} + \frac{GD/100}{d_{graft}} + \frac{WU/100(1+GD/100)}{d_w}}$) in the water-swollen state can be deduced as well.

The anion conductivity of AEM was measured in the plane direction at 100 kHz using four-point probe alternating current electrochemical impedance spectroscopy with an electrode system connected to an LCR meter (HIOKI 3522 LCR HiTESTER) at the desired temperature.[17] AEM was fully hydrated in nitrogen-saturated deionized water and placed between two platinum electrodes. The anion conductivity σ (mS/cm) was calculated from the

obtained resistance R (Ω) according to the following equation.

$$\sigma\ (mS/cm) = L / (S \times R) \times 10^3 \qquad (6)$$

where L (cm) is the distance between two electrodes, and S (cm^2) is the cross-sectional area of the membrane obtained by multiplying the membrane thickness by the membrane width.

The alkaline stability of AEM was examined by soaking the membrane in a 1-M KOH solution in a vial at 80°C for up to ~600 h and evaluated by measuring a change in the anion conductivity at 60°C. Before the conductivity measurement, the membrane was thoroughly washed with N_2-bubbled deionized water.

II-4. SANS measurement

SANS measurements were mainly performed on a KWS-2 SANS diffractometer operated by Juelich Center for Neutron Science at the neutron source Heinz Maier-Leibnitz (FRM II reactor) in Garching, Germany.[30] The incident neutron beam at KWS-2 was monochromatized with a velocity selector to have the average wavelength (λ) of 5 Å with a wavelength resolution of $\Delta\lambda/\lambda$ = 20%. The scattering patterns were collected with a two-dimensional scintillation detector and circularly averaged to obtain scattering intensity profiles as a function of q, where q is the scattering vector, which is defined by $q = (4\pi/\lambda)\sin(\theta/2)$. λ and θ are the neutron wavelength and scattering angles, respectively. Some SANS measurements were performed on an IBARAKI materials design diffractometer (iMATERIA) at the Japan Proton Accelerator Research Complex (J-PARC) under a user program (proposal No. 2017B0210) to confirm the scattering spectra at high-q range. To follow the membrane structure at the real experimental condition, AEMs were measured in a hydroxide form. To prevent degradation, excess hydroxide ions were completely removed by washing AEMs in degassed water under N_2 flow. The obtained scattering profiles were corrected for the instrument background, detector sensitivity, and scattering from empty cell, and finally calibrated to absolute scale (cm^{-1}) using a Plexiglas secondary standard. The incoherent scattering intensity of each sample was estimated by the flat part of the profile at high-q range and was subtracted from the absolute

scattering intensity profile. All SANS measurements were performed at 25 ± 0.5°C.

II-5. Membrane electrode assembly fabrication and fuel cell test

The membrane electrode assembly (MEA) was fabricated using the catalyzed gas diffusion electrode (GDE) method. AEM98 (1.71 mmol/g) and BTMA (2.74 mmol/g) in chloride form were frozen in liquid N_2 and ground into powder for 5 min using a freezer mill (JFC-300, Japan Analytical Industry) and used as ionomer. The catalyst and ionomer powder were mixed and grinded for 5 min with a mortar and pestle; then, 1 mL of deionized water was added, and grinding continued for 5 min to obtain a homogenous slurry. Then, 7 mL of 2-propanol was added with grinding. The ink was homogenized by ultrasonication (WT-100M) for 1 h at room temperature. The catalyst ink was sprayed on the gas diffusion layer (GDL, SIGRACET®, GDL35BC) and dried in air to prepare GDE. The ionomer ratio was adjusted to be 10 wt% on the basis of anode and cathode. For the anode side, Ni–C catalyst (64.5% Ni) was used, and the catalyst loading was adjusted to 2.5 ± 0.1 mg/cm^2. The cathode side was prepared using an NPC-2000 (Co–Fe) catalyst, and the catalyst loading was adjusted to 1.45 ± 0.1 mg/cm^2. The geometric surface areas of all GDEs were 5.0 cm^2. The GDEs and membranes were immersed in 1-M KOH overnight at room temperature, and excess KOH was gently wiped from the membranes and GDEs. Then, the membrane was sandwiched between two GDEs to fabricate MEA.

The fuel cell performance was investigated in a single cell with serpentine flow channels with 10-wt% hydrazine hydrate and a 1-M KOH aqueous solution as a fuel at 80°C. The flow rate of hydrazine hydrate fuel was adjusted to 20 mL/min. At the cathode side, the humidified oxygen gas flow rate and the back pressure were optimized to be 100 mL/min and 10 kPa, respectively, to obtain the maximum performance. Current–voltage curves were recorded using an electronic load. Durability was evaluated by the OCV-hold test with an oxygen flow rate of 100 mL/min without back pressure. Voltage loss was recorded under constant current density of 8.0 mA/cm^2 for 455 h.

III. Results and discussion

III-1 Preparation and characterization of AEMs

III-1.1 Preparation

As shown in Scheme 2, the radiation-induced graft polymerization of StIm into pre-irradiated ETFE films was conducted in the monomer solution of StIm in 1,4-dioxane at 60°C for 0.67–16 h to obtain StIm-grafted ETFE films with GDs in the range of 8–98%. The molecular structure of the graft polymers was confirmed by ^{13}C solid-state NMR spectrum as shown in Figure S1 in the supporting information. Generally, GD rapidly increases with time in the first 12 h, meaning that in this time span, the reaction time is a crucial factor to vary GD. The longer the reaction time is, the larger is GD. While after 12 h, an increase in GD with time slows down, and GD is up to ~98% at 16 h, close to the saturation value under the current radiation condition. The plot of GD as a function of reaction time is shown in Figure S2 in the Supporting Information.

The obtained StIm-grafted ETFE, the films were *N*-methylated with iodopropane in 1,4-dioxane to give AEMs in the iodide form. The N-alkylation reaction of StIm units of the grafts in homopolymer-grafted film proceeded quantitatively, evidenced by the weight change measurement.[18] Because the ion-exchange reaction of AEMs from iodide to hydroxide in grafted-type AEMs was slow, we conducted the ion-exchange reaction for the hydroxide form via the corresponding chloride form of AEMs (namely, $I^- \rightarrow Cl^- \rightarrow OH^-$). The completion of reactions was confirmed by the SEM-EDX spectrum, as previously reported.[18]

The representative IEC_{exp} values determined by the conventional titrimetric analysis shown in Table 1 were plotted as a function of GD in Figure S3 in the Supporting Information. These IEC_{exp} values are at 76–93% levels of the expected IEC (IEC_{cal}) calculated using the millimolar amount of a quaternary ammonium salt in the unit weight (1 g) of AEM. A similar phenomenon was also observed for AEMs containing imidazolium or anilinium hydroxide in graft polymers.[20, 31-33] In our latest report, we elucidated that this phenomenon was due to the

distribution of a part of graft polymers (which are non-conductive) in the non-conductive phase.[20] We also stated that the ratio of IEC_{exp} to IEC_{cal} (IEC_{exp}/IEC_{cal}) increases with GD and approximately characterizes the ratio of graft polymers in the conducting phase to the total graft polymers. Therefore, an increase in GD is an effective way to increase the fraction of "conductive" graft polymers over the total graft polymers made.[20]

III-1.2 Conductivity, WU, and hydration number

The characteristics of these AEMs are listed in Table 1. The initial OH^- conductivity (σ_{OH^-}) of AEMs with different GDs at 25°C was plotted as a function of IEC_{exp} in Figure 1(a). Similar to previous PEMs and AEMs, σ_{OH^-} increases with an increase in IEC_{exp} owing to the increased number density of ionic groups, and also with an increase in the temperature, *i.e.* 60°C as shown in Figure S4 in the Supporting Information, owing to the enhanced ion transfer at elevated temperature. By linear extrapolation of the data in Figure 1(a) toward zero, one can obtain a similar threshold value of 0.2 for $\sigma_{OH^-} = 0$, which represents the onset of anion transport. The existence of this threshold for the anion transport results from disconnected ion channels in AEMs with very low IECs.

The WU and λ_w of AEMs were plotted as a function of IEC_{exp} in Figures 1(b) and 1(c), respectively. Figure 1(b) shows a slow increase in WU at IEC_{exp} values lower than 0.54 mmol/g, and then a rapid increase in WU with an increase in IEC_{exp}. Figure 1(c) shows a discontinuous increase in λ_w with an increase in IEC_{exp}, namely, AEMs showed λ_w of approximately 10 at IEC_{exp} lower than 0.54 mmol/g, and those of 22–27 at IEC_{exp} higher than 0.9 mmol/g. The λ_w of AEM with IEC_{exp} of 0.8 mmol/g represents a value (~14) at the transition. This discontinuous change in λ_w may indicate the existence of a significant structural modification, which enables the membrane to adsorb more water. To explain these changes, we define characteristic IEC (IEC_c), which is the crossover of two linear relationships in Figure 1(b), to be approximately 0.7–0.8 mmol/g. Thus, the corresponding characteristic GD (GD_c) is in the range of 20–25%. We presume distinct changes in both the structure and properties before and after characteristic

IEC_c or GD_c, which will be discussed in detail in later sections.

In contrast to WU and λ_w, the IEC_{exp} dependence of conductivity seems more continuous, as shown in Figure 1(a). This suggests that the structural change predicted from the unusual jump of λ_w does not affect the anion-conducting behavior. A similar phenomenon was also reported by Amel *et al.*, in which they observed a steep increase in WU but not conductivity in quaternary ammonium poly(sulfone) based AEMs with IEC.[34]

Compared with the previously reported Im/St-AEMs with similar IEC,[17-21] these new AEMs show similar conductivities but much lower WU and λ_w. This occurs probably because the hydrophilic/hydrophobic phase separation is much stronger in the current AEMs because the homopolymer graft chains with more regularly arranged hydrophilic Im groups are perpendicularly connected to hydrophobic St units rather than those in Im/St-AEMs, which contain copolymer grafts with parallelly connected Im and St segments in a random manner. Thus the reinforced hydrophobic domains in the graft chains together with semi-crystalline domains in ETFE base films constrain the mechanical and dimensional change of AEMs against the water swelling. This effect is like the addition of cross-linkers to polyethylene-based AEMs, which increased the ion density so that the conductivity, but decreased the water swelling.[35] It is rational that a clear microphase separation between ionic groups and polymer backbone is an efficient way to create water/ion channels and reduce WU.

III-1.3 Long-term alkaline durability

The alkaline durability of these AEMs was evaluated by following the change in the membrane conductivity when AEMs were immersed in 1-M KOH at 80°C.[8-13] Figure 2 shows a change in the relative conductivities of AEMs with different GDs of 18, 30, 42, and 56%, designated as AEM18, AEM30, AEM42, and AEM56 at 60°C on the basis of their initial conductivities, respectively. AEM18 shows an excellent alkaline stability over 600 h, judging from its constant conductivity (50–60 mS/cm at 60°C) during the entire immersion period, although the surface of the membrane appears to be slightly rougher than its initial state.

AEM18 with moderate conductivity and high stability in an alkaline solution containing low WU is almost the best AEM up to now compared with the other AEMs reported in the literature.[8-21] However, all other three AEMs with IECs > IEC_c show poor durability in the alkaline solution. After 600 h, the relative conductivities of those AEMs decreased to less than 10% level of their initial values. The evaluation of membrane durability for all AEMs was marked in Table 1. The results show that similar to WU and λ_w, the long-term alkaline durability also exhibits a dramatic change across IEC_c.

III-2 Structural analysis of StIm-AEMs with different IECs in dry and water-swollen states

As mentioned above, the WU, λ_w, and alkaline durability of AEMs have transition points at IEC_c (0.7–0.8 mmol/g) or GD_c (20–25%), as shown in Figure 1. Because the unusual IEC_{exp} dependence of membrane properties cannot be explained by only chemical structures and their primary properties, the effect of higher-order structural transition may be profound in the membrane. Thus, to clarify whether the expected structural change occurs or not, three AEMs with GDs of 8, 11, and 14% and four AEMs with GDs of 30, 42, 56, and 86%, which have lower and higher IECs than IEC_c, were selected to perform SANS measurements.

Figures 3(a) and 3(b) show the SANS profiles of these AEMs in dry and fully water-swollen states at room temperature, respectively. For water-swollen AEMs, D_2O was used as a solvent to obtain higher scattering intensity and lower incoherent scattering background. To catch the structural features at high-q range, the incoherent scattering intensity was removed for all profiles. The original scattering profiles before the incoherent scattering correction for AEMs in dry and wet states are shown in Figures S5(a) and S5(b) in the Supporting Information, respectively. According to the scattering features, as discussed in our previous papers, we expediently separate these SANS profiles into two q-regions. Region I at $q < 1.3$ nm^{-1} is related to the microphase separation between conducting/non-conducting phases, and Region II at $q >$ 1.3 nm^{-1} is related to the local structures in the conducting phase.[20]

III-2.1 Dry AEMs

In Region I, a broad correlation peak at approximately 0.15–0.25 nm^{-1} was observed for all dry AEMs in Figure 3(a). These typical broad peaks with a *d*-spacing of approximately 30 nm were well characterized as the microphase separation between ETFE base material and graft polymers constrained by the alternation of crystalline phase and amorphous phase, as mentioned in our previous studies.[18-20] The peak intensity increased with IEC at 0 < IEC < 0.95 mmol/g, and then kept as a constant or even slightly decreased level when IEC further increased. A similar phenomenon has been reported before in ETFE-based poly(styrene sulfonic acid)-grafted PEM, which was attributed to the possible formation of extra PS graft polymer domains when IEC was high.[16] Similar to our previous reports, the peak position shifted to the low *q*-range with an increase in IEC especially at IEC < 0.95 mmol/g (GD < 42%), and the broadness of the peak increased, which suggests that the incorporation of more graft polymers in amorphous domains expanded the stacking distance and perturbed the ordering arrangement.[18–20] At IEC > 0.95, the low-*q* shift of the peak was not clear, which confirmed that graft polymerization in lamellar stacks nearly stopped, and the polymerization proceeded most likely outside of lamellar stacks.[18] All profiles of dry AEMs at $q > 0.2$ nm^{-1} obeyed Porod's law, *i.e.*, $I(q) \sim q^{-4}$,[36] which characterizes the distinct phase separation between graft polymers and ETFE base materials with a sharp boundary.

At the high-*q* range of $q > 1.3$ nm^{-1} (Region II), no specific structure feature of $I(q)$ profiles was observed regardless of IEC or GD, even though there were many reports showing ionomer peaks in this *q*-region. This occurred probably because no obvious ion channels were formed without water. Thus, dry AEMs with different IECs show similar local structures and distribution of graft chains.

III-2.2 AEMs equilibrated in D_2O

At the *q*-range of 0.15–0.25 nm^{-1} (Region I), by comparing Figures 3(a) and 3(b), it is determined that D_2O-equilibrated AEMs exhibited the correlation peak at lower *q* compared to

the corresponding dry AEMs because the incorporation of water with the graft polymers in the amorphous domains expanded the periodic lamellar *d*-spacing of crystalline and amorphous phases. Because the scattering profiles of all wet AEMs also showed similar Porod's behavior to those of dry AEMs in this region, it can be concluded that the incorporation of water does not deteriorate the sharp boundary between hydrated graft polymers and hydrophobic ETFE base materials.

At the high-q range (Region II), a water-swelling-induced peak, which was not observed in dry AEMs, newly appeared. Specifically, all D_2O-equilibrated AEMs showed a clear scattering maximum (i.e., ionomer peak), which indicated the formation of ionic clusters in the conducting phase.[37-43] The ion clustering effect has been regarded as an effective factor for the fast diffusion of water and conduction of ions through the membrane.[44-51] The ionomer peak of AEM08 seemed to be slightly broader than other AEMs and had the lowest intensity. The peak position, q_2, is ~3.0 nm^{-1}, which indicated that the mean distance between two ionic domains, d_2 ($=2\pi/q_2$), was approximately 2.1 nm. The peak became sharper with higher intensity when IEC increased, which suggested the formation of more distinct well-separated nanodomains. We summarized all d_2 of wet AEMs in Table 2 and plotted them as a function of IEC in Figure 3(c). This result shows that d_2 barely changes at IEC < IEC_c (or GD < GD_c), and then steadily increases at IEC > IEC_c. Thus, the IEC (or GD) dependence of d_2 should also relate to the structural change across IEC_c, similar to what we observed in the WU and durability measurements.

III-3 Characteristic hierarchical structures interpreted by contrast variation method

III-3.1 Conducting/non-conducting two-phase feature and the distribution of graft polymers in both phases

To reveal the structural difference in these AEMs, the contrast variation SANS measurements were performed for AEMs with lower IECs (*i.e.*, AEM14) or higher IECs (*i.e.*, AEM42 and AEM86) than IEC_c. The scattering profiles of these three AEMs equilibrated in

different H_2O/D_2O mixtures are shown in Figure S6 in the Supporting Information. As mentioned in Scheme 1, the structural analysis in Region I allowed us to clarify the microphase separation characteristics of the membranes. Our recently reported structural model of "conducting/non-conducting two-phase system" can be used to describe microphase separation and the distribution of graft polymers in each phase for graft-type AEMs with Im/St copolymer grafts onto ETFE.[20] The model was verified by ruling out other possible structural models in ref. 20. Here, we apply this model to analyze the structure of current membranes. We omit the detailed description of the model and only mention the two important facts. Specifically, (1) the non-conducting phase (phase 1) is made of ETFE base polymers and non-conductive graft polymers. The conducting phase (phase 2) is made of conductive graft polymers and water. Phases 1 and 2 are clearly separated. (2) The volume fractions of graft polymers distributed in conducting ($\phi_{c\text{-graft}}$) and non-conducting ($\phi_{nc\text{-graft}}$) phases can be evaluated in a quantitative manner by the contrast variation and contrast matching SANS method, as shown in Figures S6 and S7 in the Supporting Information.

As listed in Table 2, we estimated $\phi_{nc\text{-graft}}$ and $\phi_{c\text{-graft}}$ of each AEM (the calculation methods were described in the Supporting Information) for the distribution of graft polymers in either conducting or non-conducting phases. With an increase in IEC, $\phi_{c\text{-graft}}$ increased from 0.133 (AEM14) to 0.274 (AEM86), whereas $\phi_{nc\text{-graft}}$ was relatively constant with a value of approximately 0.03.

III-3.2 Nanophase separated structure in the conducting phase

In Region II (q > 1.3 nm^{-1}), all SANS profiles of water-swollen AEMs showed a clear ionomer peak, which is the typical structural feature of the conducting phase, as shown in Figures 3(b) and S6. Compared to previously reported Im/St-AEMs,[20] the ionomer peaks of current StIm-AEMs are much sharp, which indicates a more distinct nanophase separation in the conducting phase owing to the linear chemical arrangement of St and Im moieties. The contrast variation experiments for the representative membranes AEM14, AEM42, and AEM86

showed that the profiles around the ionomer peak were superimposed with one another by the vertical shifting of the curves [Figures S8(a)–S8(c)], which confirmed that the conducting phase can be treated as a two-component system, *i.e.*, it consists of hydrophilic (water) and hydrophobic (graft polymer) components.

The origin of the ionomer peak is attributed to the correlation of one of these two components. According to Babinet's principle,[36] it is not possible to distinguish which component corresponds to the correlation peak from a scattering curve alone. Namely, for AEMs, it is not clear from only Figure 3 whether the hydrophilic domains are dispersed in the hydrophobic matrix ("reverse-micelles") or the opposite ("micelles"), as illustrated in Figures 4(a) and 4(b), respectively. However, considering the volume fraction of scattering objects and the matrix, which generally correspond to minor and major components in a system, one can estimate that either a hydrophilic or a hydrophobic domain is a sphere (*i.e.*, the exact component for the origin of the ionomer peak). In the following sections, we apply the hard-sphere liquid model and Porod limit analysis to assign the origin of the ionomer peak.

Hard-sphere liquid model analysis

First, we employ the hard-sphere (HS) liquid model developed by Kinning and Thomas using the Percus–Yevick correlation function, which describes the structure of ionic conducting materials.[20, 36, 52-58] In this model, scattering objects are assumed to be spherical particles with an average radius (R_S) randomly distributed in the conducting phase. The particles are considered to be liquid-like with isotropic spatial distribution, and the average distance between the nearest-neighbor pair (r_0) is larger than $2R_s$. In this study, d_2, which is determined from the ionomer peak maximum, is used as r_0. Thus, the observed scattering intensity, $I(q)$, is expressed as a function of the volume fraction of spheres in the conducting phase (V_S) and R_S.[20, 54-56] The details of how to apply this model to grafted AEMs for the determination of R_S and V_S can be found in ref. 20. The ionomer peaks in the scattering profiles in Figure 3(b) were fitted well by the HS-liquid model, as highlighted in Figure 5. The values of R_S and V_S, obtained by the best-

fitting curves for the scattering data, are listed in Table 3. The R_S values of AEMs increased from 10.2 Å to 12.6 Å with an increase in IEC from 0.24 to 1.72 mmol/g. V_S seemed to be a more constant value as a function of IECs with a slight increase from 0.33 to 0.41 in the low IEC range.

The component in the sphere can be specified as water or graft polymers by comparing their volume fractions in the conducting phase with V_S. Specifically, we first estimate the volume fractions of water (V_w) and graft polymers ($V_{graft} = 1-V_w$) and then check whether V_w or V_{graft} matches the value of V_S. V_w can be independently estimated from $\phi_{c-graft}$, which is determined from contrast variation experiments (Method-1) or from λ_w, which is determined from the WU measurements (Method-2) using the following equations:

Method-1) $$V_{w1} = \frac{\phi_w}{\phi_w + \phi_{c-graft}} \quad (7)$$

Method-2) $$V_{w2} = \frac{18\lambda_w}{18\lambda_w + M_{seg}} \quad (8)$$

where M_{seg} = 255 (g/mol) is the molecular weight of one repeating unit with an ionic imidazolium head on the graft polymer chain. As listed in Table 2, the V_{w1} values are almost the same as the values of V_{w2}, which confirms not only the correctness of V_w, but also validity of the quantitative analysis in the conducting/non-conducting microphase separation structure model using the contrast variation method in Section-III.3.1. The average value of V_{w1} and V_{w2} was defined as V_w for AEM14, AEM42, and AEM86, while the V_{w2} value was utilized as V_w for other AEMs, as listed in Table 3.

Similar to the IEC dependence of WU and λ_w shown in Figure 1, V_w exhibited minor (0.43–0.45) and major (0.61–0.65) components for StIm-AEMs with lower and higher IECs than IEC_c, respectively. The comparison of V_S with V_w or V_{graft} in Table 3 was plotted in Figure 7(a) as a function of GD. It shows that V_S is close to V_w for AEMs with low IEC < IEC_c and to V_{graft} for AEMs with high IEC > IEC_c. This result indicates that the structure of the conducting phase in these AEMs varies from “reverse-micelles” (water puddles dispersed in the polymer

matrix) to "micelles" (graft polymer aggregates dispersed in water) across the critical point of IEC (IEC_c). Note that V_S of AEM08 is slightly smaller than V_w probably because the spherical water domains in AEM08 are not well-developed and less connected due to the small number density of cation groups in the membrane. Instead, AEM30 with the IEC, close to transition value (IEC_c) showed larger V_w (~0.5) than the corresponding V_S, probably resulting from the mixed structures of "micelles" and "reverse-micelles" in the membrane.

Porod limit analysis

To confirm the component of the spheres in the conducting phase of AEMs and its GD dependence obtained above by the hard sphere liquid model in the last section, we apply the Porod limit analysis to estimate the component of the spheres and the averaged radius of spheres, defined as R_{Porod}, to distinguish it from R_S obtained by the hard sphere liquid model.[36, 58]

Because ideal two-component systems (e.g., charged colloidal system and an ionic membrane/solution) discussed in this study possess a clear interfacial boundary, $I(q)$ should decrease as $\sim q^{-4}$ for large q (so-called Porod law) with the proportionality constant, which is related to the total area of the graft polymer/water interface (A) in the scattering volume (V).[36, 58] Thus, as $q \to \infty$,

$$\lim_{q\to\infty} I(q) \to 2\pi\Delta b^2 \Sigma / q^4 \qquad (9)$$

where $\Sigma = A/V$, and Δb is the scattering length density difference between graft polymers and water (D_2O), which is $\sim 5.27 \times 10^{10}$ cm^{-2} in this study. In Figure 6, we plot Iq^4 versus q for all AEMs. All profiles exhibit a constant behavior at high-q range, which indicates the sharp polymer/water interface. Thus, Σ of each AEM was extracted using eq. (9) and is listed in Table 4.

Owing to the energetic requirement of the spherical shape to minimize the interfacial free energy, the spherical structures of "reverse-micelle" or "micelle" models are widely accepted as typical microscopic structures for polymers consisting of hydrophilic/hydrophobic units, as

illustrated in Figures 4(a) and 4(b), respectively. The size and component of spherical domains are related to Σ, as will be discussed in detail below. The mixed structures may exist in AEM30; thus, this analysis is not applied to the AEM30 membrane.

For the "reverse-micelles" model, the spherical domains are composed of water, as illustrated in Figure 4(a). Thus, the Porod radius of water spheres, $R_{Porod,w}$, can be estimated from the interface quantity of Σ on the basis of the following equation[59–61]

$$R_{Porod,w} = \frac{3\phi_w}{\Sigma} \qquad (10)$$

$R_{Porod,w}$ values for all AEMs are listed in Table 4. The $R_{Porod,w}$ values of AEMs with low IECs < IEC_c are nearly constant at approximately 11.8 Å, which is comparable to R_S (approximately 10.5 Å) obtained from the HS-liquid model. Whereas, those of AEMs with high IECs > IEC_c are estimated to be 23.8–26.3 Å, which is much larger than the corresponding R_S, as shown in Figure 7(b). The values for AEMs with high IECs exceed the upper limit of the mean distance between two spheres (*i.e.*, d_2), which indicates that the "reverse-micelles" model does not match the case of AEMs with high IECs.

For the "micelles" model, the spherical domains are made of graft polymers, as illustrated in Figure 4(b). The Porod radius of graft polymer spheres, $R_{Porod,g}$, can be estimated by the following equation:

$$R_{Porod,g} = \frac{3\phi_{c-graft}}{\Sigma} \qquad (11)$$

As listed in Table 4 and plotted in Figure 7(b), the resultant $R_{Porod,g}$ values of AEMs with high IECs > IEC_c are in the range of 14.2–14.8 Å, which is comparable to R_S values and confirms the validity of the "micelles" model. Both $R_{Porod,w}$ and $R_{Porod,g}$ are larger than $d_2/2$, which means that spherical domains should be connected to one another and, thus, well-percolated. On the basis of the abovementioned comparison between R_S and R_{Porod} for all AEMs with various IECs, it is concluded that StIm-AEMs possess "reverse-micelles" and "micelles" model structures in low and high IEC ranges in the conducting phases, as schematically illustrated in Figures 8(a)

and 8(b), respectively.

Local structures around imidazolium ionic groups

Another important parameter possibly obtained from the Porod limit analysis is the interfacial area occupied per ionic head (*S*).[59-61] We assume that all ionic imidazolium groups with the total number of N_{ion} existing in the scattering volume of V are located at the graft polymer/water interface with an occupied area of *S*. Thus, the *S* value can be calculated using the following equation:

$$S = \frac{\Sigma}{N_{ion}/V} = \frac{v_0 \Sigma}{\phi_{c-graft}} \qquad (12)$$

where v_0 is the volume of graft polymer associated with one ionic group, which can be calculated from the equivalent weight of the repeating unit and its mass density of approximately 424 Å^3, and $\phi_{c\text{-graft}}$ is the effective volume fraction of graft polymer in the conducting phase, as we quantitatively determined in the abovementioned section.

The resultant *S* values are shown in Table 4 and Figure 7(c). The obtained value shows that *S* is approximately constant (80–93 Å^2), regardless of IEC and WU. The *S* values of these StIm-AEMs are relatively larger than those obtained for long-pendant side chain PFSI (55–61 Å^2)[59, 60] or short-pendant side chain PFSI (70–74 Å^2)[61] partially because of the larger size of imidazolium cationic group compared to the sulfonic acid group in those systems, and partially because of the weaker interaction between the ion-pair of imidazolium cation and OH^- than that of sulfonic acid and H_3O^+, which has been confirmed by molecular dynamics simulation studies.[62]

It is possible to estimate the average number of ionic groups per spherical domain, n_{ion}, using the following equation:

$$n_{ion} = \frac{4\pi {R_{Porod}}^2}{S} \qquad (13)$$

Thus, the obtained n_{ion} values are shown in Table 4 and Figure 7(c). For AEMs with IECs < IEC_c, n_{ion} is approximately 19–22. For AEMs with IECs > IEC_c, n_{ion} increases to 28–32.

Because *S* is almost conserved, the larger value of n_{ion} is attributed to the larger particle size of micelles relative to reverse-micelles.

The structure inversion from "reverse-micelles" to "micelles" increases the total WU and λ_w and also lowers membrane stability in alkaline solutions. Because the ionic imidazolium groups in "reverse-micelles" and "micelles" face the inner and outer interface direction of spherical domains, the former one is surrounded by fewer free spaces in the water domain than the latter one, which leads to smaller λ_w, as schematically shown in Figures 8(c) and 8(d). In other words, even though the area of interface occupied by one ionic group (*S*) is conserved, with an increase in IEC, a higher reaction rate of hydrolysis around the ionic groups is expected owing to the increased number of water molecules around the ionic groups, which considerably decreases stability in alkaline solutions. Even though the structure evolution in these StIm-AEMs is similar to those of perfluorosulfonated ionomer membranes (*i.e.*, Nafion® and its derivatives), the chemical composition and size of hydrophobic domains in these StIm-AEMs are unique.[59-61]

III-3. Hydrazine hydrate fuel cell performance and durability

The fuel cell performance is strongly dependent on the property of AEMs, such as water permeability and fuel barrier property in addition to interaction with catalyst layers. We fabricated four MEAs using StIm-AEMs, with IECs of 0.54 mmol/g (AEM18), 0.78 mmol/g (AEM30) 0.95 mmol/g (AEM42), and 1.71 mmol/g (AEM98), and the most frequently-used organic cations BTMA powder as an ionomer with Ni–C (2.5 mg/cm^2) and NPC-2000 (1.6 mg/cm^2) as an anode and cathode, respectively. The single hydrazine hydrate fuel cell performance was shown in Figure S9. MEA with AEM42 showed the best performance and achieved the maximum power density of 38 mW/cm^2 at the current density of 90 mA/cm^2, at the optimal flow rate of 50 mL/min with a back pressure of 10 KPa at the cathode side. Contrary to AEM42, MEA with AEM18 and AEM30 presented nearly no performance, and with AEM98 achieved lower performance of 25 mW/cm^2 at the current density of 60 mA/cm^2.

According to the ex situ membrane durability test results in an alkaline solution shown in Figure 2 and the abovementioned structure analysis, AEM18 is regarded as the most suitable membrane with both good conductivity and alkaline durability owing to its reverse-micelle structure. However, MEA fabricated with AEM18 showed such poor fuel cell performance, although the ex situ membrane properties were good. This result indicates that the real fuel cell operation condition should be deviated from the ex situ alkaline solution. The structural analysis of the membranes required for the durability in the real fuel cells is not sufficient. However, so far, the membrane structures in the fuel cell cannot be analyzed clearly. Thus, we believe it is one of the promising methods to estimate them in fuel cell operating condition from the evidence of the membrane structures in ex situ solutions, which are clearly analyzed. It is known that the membrane under the fuel cell operation condition is relatively dry compared to that in an alkaline solution. The lower hydration increases the hydrophobicity of the membrane surface, which decreases surface adhesion to ionomers and catalyst layers and disconnects the network structure of ionic channels in the membrane. Consequently, the in situ conducting properties of AEM18 and even AEM30, are worse than those of the fully hydrated condition in the ex situ solution test, which leads to the poor fuel cell performance. In addition, the lower hydration effect in MEA possibly shifts the structure transition point of IEC_c toward higher IEC values; Thus, AEMs with relatively higher IEC, *i.e.*, AEM42, assembled in MEA may possibly keep the stable reverse-micelle structure, which is essential for the long-term in situ durability requirement.

It should be addressed that MEA fabricated with AEM98 showed worse fuel cell performance than AEM42 probably owing to the fact that AEM98 with a micelle structure is structurally too weak to exhibit good performance in either ex situ alkaline solutions or under severe hydrazine/KOH alkaline fuel cell conditions.

In order to improve the fuel cell performance, anion-conducting ionomers typically need to have a chemical structure that is similar to that of AEMs as well as higher anion conductivity

compared to that of AEMs to achieve good adhesion and connectivity of ion-paths at the molecular level. Therefore, we re-assemble MEA using AEM42 as membrane and fine-powdered AEM98 in chloride form as anion-conducting ionomer, which was prepared by pulverization using a freezer mill according to the literature.[63] The much improved fuel cell performance was achieved with the maximum power density of 80 mW/cm^2 at the current density of 140 mA/cm^2 as shown in Figure 9(a). It also exhibited a high OCV of 0.86 V, which indicated low fuel and gas permeability. The oxygen flow rate showed a considerable effect on the cell performance in which the performance was improved at the optimal flow rate of 100 mL/min with a back pressure of 10 KPa at the cathode side.

Since MEA fabricated with AEM42 exhibits the best fuel cell performance, the further durability test was performed at the constant current density of 8.0 mA/cm^2 at 80°C. As shown in Figure 9(b), this single cell exhibited excellent durability up to 455 h and maintained 64.7% (0.68 V) of the initial voltage. To our knowledge, this is one of the most durable alkaline-type fuel cells.[64–66] These results showed that Im/St-AEMs and their ionomer powders are promising materials for alkaline fuel cell applications in terms of performance and long-term durability. This result also confirms our previous presumption that AEMs under the in situ durability test condition are less hydrated than those in the ex situ (solution) test; thus AEMs with higher IEC, *i.e.* AEM42, still possess stable reverse-micelle structure and maintain long-term durability. It is essential and complicated to understand the membrane performance and in situ durability under the fuel cell conditions.[67] Therefore, the ex situ examinations of conducting properties, durability, and membrane morphologies are important to offer a mechanistic insight in the membrane properties–morphology relationships.

IV. Conclusions

In this study, we prepared new graft-type AEMs, composed of poly(2-(4-styryl)-N,N-dipropylimidazolium hydroxide) homopolymer graft chains containing different IECs, on ETFE films via the radiation-induced grafting technique. We investigated the effects of IEC on

electrochemical properties and durability in alkaline solutions. A critical IEC value, IEC_c (0.7–0.8 mmol/g) was observed. Below IEC_c, the membranes show low WU and very good alkaline stability in a 1 KOH solution at 80°C. Above this value, the membranes adsorb more water and are susceptible to hydrolysis.

This phenomenon was interpreted by structure evolution using the SANS technique with the contrast variation method. We proposed that at IECs < IEC_c, the structure of conducting phase in AEMs was characterized by the traditional "reverse-micelles" model. While at IEC > IEC_c, the structure changed to the network structure of "micelles". The further analysis using the hard-sphere liquid model and Porod limit analysis revealed that this structure inversion was dominated by the polymer/water interfacial energy, which imposed the conservation of interface area per ionic group. Thus, AEMs with the "reverse-micelles" structure were more alkaline-durable owing to the lower number of water molecules around one ionic group, which resulted in a slower hydrolysis reaction rate. The results in this study indicated that the molecular design in this type of AEMs to prevent ionic structure inversion from "reverse-micelles" to "micelles" is crucial to suppress WU and the susceptibility of the hydrolysis reaction. An increase in the hydrophobicity of the graft polymer backbone and the introduction of larger chemical hindrance around ionic groups might be a practical way to keep the "reverse-micelles" structure and improve the membrane stability in alkaline solutions.

MEA fabricated with AEM18 showed very poor fuel cell performance, although the ex situ membrane properties were good. However, AEM42 with the IEC of 0.95 mmol/g, with the maximum power density of 80 mW/cm^2 in the hydrazine hydrate fuel cell test, exhibited long-term durability under constant current (8.0 mA) up to 455 h, which thus far showed the best durability at 80°C compared to other platinum-free alkaline-type liquid fuel cells. In the typical platinum-free hydrazine hydrate fuel cell test, the membrane hydration level in MEA was less than that in an alkaline solution. Accordingly, IEC_c most likely shifted to higher IEC values, *i.e.*, > 0.95 mmol/g.

Notes

The authors declare no competing financial interest.

Acknowledgments

This work was partially supported by Grant-in-Aid for Scientific Research (A) from Japan Society for the Promotion of Science (JSPS) (KAKENHI Grant Number: 18H03850) and partially supported by “Advanced functional polymer materials alliance” project under QST innovation hub program in collaboration with participant companies.

References.

1. Steele, B. C. H.; Heinzel, A. Materials for fuel-cell technologies, *Nature* **2001**, *414*, 345-352.
2. Vielstich, W.; Lamm, A.; Gasteiger, H. *Handbook of Fuel Cells: Fundamentals, Technology, Applications*; John Wiley: 2004.
3. Peighambardoust, S. J.; Rowshanzamir, S.; Amjadi, M. Review of the proton exchange membranes for fuel cell applications, *Int. J. Hydrogen Energy* **2010**, *35*, 9349-9384.
4. Gasteiger, H. A.; Panels, J. E.; Yan, S. G. Dependence of PEM fuel cell performance on catalyst loading, *J. Power Sources* **2004**, *127*, 162-171.
5. Jacobson, M. Z.; Colella, W. G.; Golden, D. M. Cleaning the air and improving health with hydrogen fuel-cell vehicles, *Science* **2005**, *308*, 1901-1905.
6. Wee, J. H. Applications of proton exchange membrane fuel cell systems, *Renewable & Sustainable Energy Reviews* **2007**, *11*, 1720-1738.
7. Wang, Y.; Chen, K.; Mishler, J.; Cho, S. C.; Adroher, X. C. A review of polymer electrolyte membrane fuel cells: Technology, applications, and needs on fundamental research, *Appl. Energy* **2011**, *88*, 981-1007.
8. Varcoe, J. R.; Slade, R. C. T. Prospects for alkaline anion-exchange membranes in low temperature fuel cells, *Fuel Cells* **2005**, *5*, 187-200.
9. Si, Z; Qiu, L.; Dong, H.; Gu, F.; Li, Y.; Yan, F Effects of Substituents and Substitution Positions on Alkaline Stability of Imidazolium Cations and Their Corresponding Anion-Exchange Membranes, *ACS Appl. Mater. Interfaces* **2014**, *6*, 4346-4355.
10. Varcoe, J. R.; Atanassov, P.; Dekel, D. R.; Herring, A. M.; Hickner, M. A.; Kohl, P. A.; Kucernak, A. R.; Mustain, W. E.; Nijmeijer, K.; Scott, K.; Xu, T.; Zhuang, L. Anion-exchange membranes in electrochemical energy systems, *Energy Environ. Sci.* **2014**, *7*, 3135-3191.
11. Couture, G.; Alaaeddine, A.; Boschet, F.; Ameduri, B. Polymeric materials as anion-

exchange membranes for alkaline fuel cells, *Prog. Polym. Sci.* **2011**, *36*, 1521-1557.

12. Merle, G.; Wessling, M.; Nijmeijer, K. Anion exchange membranes for alkaline fuel cells: A review, *J. Membr. Sci.* **2011**, *377*, 1-35.
13. Wang, Y. J.; Qiao, J.; Baker, R.; Zhang, J. Alkaline polymer electrolyte membranes for fuel cell applications, *Chem. Soc. Rev.* **2013**, *42*, 5768-5787.
14. Balog, S.; Gasser, U.; Mortensen, K.; Gubler, L.; Scherer, G. G.; Ben youcef, H. Correlation between morphology, water uptake, and proton conductivity in radiation-grafted proton-exchange membranes, *Macromol. Chem. Phys.* **2010**, *211*, 635-643.
15. Iwase, H.; Sawada, S.; Yamaki, T.; Koizumi, S.; Ohnuma, M.; Maekawa, Y. Hierarchical structure analysis of graft-type polymer electrolyte membranes consisting of cross-linked polytetrafluoroethylene by small-angle scattering in a wide-Q range, *Macromolecules* **2012**, *45*, 9121-9127.
16. Tap, T. D.; Sawada, S.; Hasegawa, K.; Yoshimura, Y.; Oba, M.; Ohnuma, M.; Katsumura, Y.; Maekawa, Y. Hierarchical structure-property relationships in graft-type fluorinated polymer electrolyte membranes using small- and ultrasmall-angle X-ray scattering analysis, *Macromolecules* **2014**, *47*, 2373-2383.
17. Yoshimura, K.; Koshikawa, H.; Yamaki, T.; Shishitani, H.; Yamamoto, K.; Yamaguchi, S.; Tanaka, H.; Maekawa, Y. Imidazolium cation based anion-conducting electrolyte membranes prepared by radiation induced grafting for direct hydrazine hydrate fuel cells, *J. Electrochem. Soc.* **2014**, *161*, F889-F893.
18. Zhao, Y.; Yoshimura, K.; Shishitani, H.; Yamaguchi, S.; Tanaka, H.; Koizumi, S.; Szekely, N.; Radulescu, A.; Richter, D.; Maekawa, Y. Imidazolium-based anion exchange membranes for alkaline anion fuel cells: elucidation of the morphology and the interplay between the morphology and properties, *Soft Matter* **2016**, *12*, 1567-1578.
19. Yoshimura, K.; Zhao, Y.; Hasegawa, S.; Hiroki, A.; Kishiyama, Y.; Shishitani, H.; Yamaguchi, S.; Tanaka, H.; Koizumi, S.; Appavou, M.-S.; Radulescu, A.; Richter, D.;

Maekawa, Y. Imidazolium-based anion exchange membranes for alkaline anion fuel cells: (2) elucidation of the ionic structure and its impact on conducting properties, *Soft Matter* **2017**, *13*, 8463-8473.

20. Yoshimura, K.; Zhao, Y.; Hiroki, A.; Kishiyama, Y.; Shishitani, H.; Yamaguchi, S.; Tanaka, H.; Koizumi, S.; Houston, J.; Appavou, M.-S.; Radulescu, A.; Richter, D.; Maekawa, Y. Reverse relationships of water uptake and alkaline durability with hydrophilicity of imidazolium-based grafted anion-exchange membranes, *Soft Matter* **2018**, *14*, 9118-9131.
21. Zhao, Y.; Yoshimura, K.; Takamatsu, H.; Hiroki, A.; Kishiyama, Y.; Shishitani, H.; Yamaguchi, S.; Tanaka, H.; Koizumi, S.; Radulescu, A.; Appavou, M.-S.; Maekawa, Y. Imidazolium-based anion exchange membranes for alkaline anion fuel cells: interplay between the morphology and anion transport behavior, *J. Electrochem. Soc.* **2019**, *166 (8)*, F472-F478.
22. Li, N.; Yan, T.; Li, Z.; Thurn-Albrecht, T.; Binder, W. H. Comb-shaped polymers to enhance hydroxide transport in anion exchange membranes, *Energy Environ. Sci.* **2012**, *5*, 7888-7892.
23. Li, N.; Zhang, Q.; Wang, C.; Lee, Y. M.; Guiver, M. D. Phenyltrimethylammonium functionalized polysulfone anion exchange membranes, *Macromolecules* **2012**, *45*, 2411-2419.
24. Zhang, F.; Zhang, H.; Qu, C. Imidazolium functionalized polysulfone anion exchange membrane for fuel cell application, *J. Mater. Chem.* **2011**, *21*, 12744-12752.
25. Zhang, H.; Shen, P. Recent development of polymer electrolyte membranes for fuel cells, *Chem. Rev.* **2012**, *112*, 2780-2832.
26. Mortensen, K.; Gasser, U.; Guersel, S. A.; Scherer, G. G. Structural characterization of radiation-grafted block copolymer films, using SANS technique, *J. Polym Sci. Polym. Phys. Ed.* **2008**, *46*, 1660-1668.
27. Nasef, M. M.; Hegazy, E. A. Preparation and applications of ion exchange membranes by radiation-induced graft copolymerization of polar monomers onto non-polar films, *Prog.*

Polym. Sci. **2004**, *29*, 499-561.

28. Song, J. M.; Ko, B. S.; Sohn, J. Y.; Nho, Y. C.; Shin, J. A study on the morphology of polystyrene-grafted poly(ethylene-*alt*-tetrafluoroethylene) (ETFE) films prepared using a simultaneous radiation grafting method, *Rad. Phys. Chem.* **2014**, *97*, 374-380.
29. Okumura, N.; Ikeda, Y. *Japan Patent* **2015**, 2015-129100.
30. Radulescu, A.; Pipich, V.; Frielinghaus, H.; Appavou, M. S. KWS-2, the high intensity / wide Q -range smallangle neutron diffractometer for soft-matter and biology at FRM II, *Journal of Physics: Conference Series* **2012**, *351*, 012026.
31. Maekawa, Y.; Yoshimura, K.; Takeuchi, K.; Hiroki, A.; Watanabe, S.; Hagiwara, T.; Shishitani, H.; Yamaguchi, S.; Tanaka, H. Alkaline durable anion-conducting electrolyte membranes prepared by radiation induced grafting of 2-methyl-4-vinylimidazole for non-platinum direct hydrazine hydrate fuel cells, *ECS Trans.* **2017**, *80*, 979-987.
32. Wang, L.Q.; Brink, J. J.; Liu, Y.; Herring, A. M.; Ponce-Gonzalez, J.; Whelligan, D. K.; Varcoe, J. R. Non-fluorinated pre-irradiation-grafted (peroxidated) LDPE-based anion-exchange membranes with high performance and stability, *Energy Environ. Sci.* **2017**, *10*, 2154-2167.
33. Ponce-Gonzalez, J.; Whelligan, D. K.; Wang, L.Q.; Bance-Soualhi, R.; Wang, Y.; Peng, Y.Q.; Peng, H.Q.; Apperley, D. C.; Sarode, H. N.; Pandey, T. P.; Divekar, A. G.; Seifert, S.; Herring, A. M.; Zhuang, L.; Varcoe, J. R. High performance aliphatic-heterocyclic benzyl-quaternary ammonium radiation-grafted anion-exchange membranes, *Energy Environ. Sci.* **2016**, *9*, 3724-3735.
34. Amel, A.; Gavish, N.; Zhu, L.; Dekel, D. R.; Hickner, M. A.; Ein-Eli, Y. Bicarbonate and chloride anion transport in anion exchange membranes, *J. Membr. Sci.* **2016**, *514*, 125-134.
35. Zhang, M.; Kim, H. K.; Chalkova, E.; Mark, F.; Lvov, S. N.; Chung, T. C. M. New polyethylene based anion exchange membranes (PE-AEMs) with high ionic conductivity, *Macromolecules* **2011**, *44*, 5937-5946.

36. See for example, Roe, R. J. *Methods of X-ray and neutron scattering in polymer science*; Oxford Uni. Press: New York, 2000.

37. Wang, W. Q.; Liu, W. J.; Tudryn, G. J.; Colby, R. H.; Winey, K. I. Multi-length scale morphology of poly(ethylene oxide)-based sulfonate ionomers with alkali cations at room temperature, *Macromolecules* **2010**, *43*, 4223-4229.

38. Hsu, W. Y.; Gierke, T. D. Ion-transport and clustering in Nafion perfluorinated membranes, *J. Membr. Sci.* **1983**, *13*, 307-326.

39. Kim, S. Y.; Park, M. J.; Balsara, N. P.; Jackson, A. Confinement effects on watery domains in hydrated block copolymer electrolyte membranes, *Macromolecules* **2010**, *43*, 8128-8135.

40. Kusoglu, A.; Modestino, M. A.; Hexemer, A.; Segalman, R. A.; Weber, A. Z. Subsecond morphological changes in Nafion during water uptake detected by small-angle X-ray scattering, *ACS Macro Lett.* **2012**, *1*, 33-36.

41. Seitz, M. E.; Chan, C. D.; Opper, K. L.; Baughman, T. W.; Wagener, K. B.; Winey, K. I. Nanoscale morphology in precisely sequenced poly(ethylene-*co*-acrylic acid) zinc ionomers, *J. Am. Chem. Soc.* **2010**, *132*, 8165-8174.

42. Yarusso, D. J.; Cooper, S. L. Microstructure of ionomers: interpretation of small-angle x-ray scattering data, *Macromolecules* **1983**, *16*, 1871-1880.

43. Ertem, S. P.; Tsai, T. H.; Donahue, M. M.; Zhang, W.; Sarode, H.; Liu, Y.; Seifert, S.; Herring, A. M.; Coughlin, E. B. Photo-Cross-Linked Anion Exchange Membranes with Improved Water Management and Conductivity, *Macromolecules* **2016**, *49*, 153-161.

44. Elabd, Y. A.; Hickner, M. A. Block copolymers for fuel cells, *Macromolecules* **2011**, *44*, 1-11.

45. Li, N.; Wang, C.; Lee, S. Y.; Park, C. H.; Lee, Y. M.; Guiver, M. D. Enhancement of proton transport by nanochannels in comb-shaped copoly(arylene ether sulfone)s, *Angew. Chem.* **2011**, *123*, 9324-9327.

46. Chen, D.Y.; Hickner, M. A. Ion clustering in quaternary ammonium functionalized

benzylmethyl containing poly(arylene ether ketone)s, *Macromolecules* **2013**, *46*, 9270-9278.

47. Liu, L.; Ahlfield, J.; Tricker, A.; Chu, D.; Kohl, P. A. Anion conducting multiblock copolymer membranes with partial fluorination and long head-group tethers, *J. Mater. Chem. A* **2016**, *4*, 16233-16244.
48. Pan, J.; Chen, C.; Li, Y.; Wang, L.; Tan, L.; Li, G.; Tang, X.; Xiao, L.; Lu, J.; Zhuang, L. Constructing ionic highway in alkaline polymer electrolytes, *Energy Environ. Sci.* **2014**, *7*, 354-360.
49. Dang, H. S.; Weiber, E. A.; Jannasch, P. Poly(phenylene oxide) functionalized with quaternary ammonium groups *via* flexible alkyl spacers for high-performance anion exchange membranes, *J. Mater. Chem. A* **2015**, *3*, 5280-5284.
50. Dang, H. S.; Jannasch, P. Exploring different cationic alkyl side chain designs for enhanced alkaline stability and hydroxide ion conductivity of anion-exchange membrane, *Macromolecules* **2015**, *48*, 5742-5751.
51. Dang, H. S.; Jannasch, P. Alkali-stable and highly anion conducting poly(phenylene oxide)s carrying quaternary piperidinium cations, *J. Mater. Chem. A* **2016**, *4*, 11924-11938.
52. Kinning, D. J.; Thomas, E. L. Hard-sphere interactions between spherical domains in diblock copolymers, *Macromolecules* **1984**, *17*, 1712-1718.
53. Percus, J. K.; Yevich, G. J. Analysis of classical statistical mechanics by means of collective coordinates, *Phys. Rev.* **1958**, *110*, 1-13.
54. Kaler, E. W.; Bennett, K. E.; Davis, H. T.; Scriven, L. E. Toward understanding microemulsion microstructure: A small-angle x-ray scattering study, *J. Chem. Phys.* **1983**, *79*, 5673-5684.
55. Seguchi, T.; Tamura, N. Mechanism of decay of alkyl radicals in irradiated polyethylene on exposure to air as studied by electron spin resonance, *J. Phys. Chem.* **1973**, *77*, 40-44.
56. Seguchi, T.; Tamura, N. Electron spin resonance studies on radiation graft copolymerization

in polyethylene. II. Grafting initiated by allyl radicals trapped in irradiated polyethylene, *J. Polym. Sci. Polym. Chem. Ed.* **1974**, *12*, 1953-1964.

57. Smit, I.; Bezjak, A. Structural changes in the grafted copolymer polyethylene-styrene, *Polymer* **1981**, *22*, 590-596.
58. Porod, G. X-ray low angle scattering of dense colloid systems. Part I., *Kolloid Zeit* **1951**, *124*, 83-114.
59. Gebel, G.; Moore, R. B. Small-angle scattering study of short pendant chain perfuorosulfonated ionomer membranes, *Macromolecules* **2000**, *33*, 4850-4855.
60. Gebel, G. Structural evolution of water swollen perfluorosulfonated ionomers from dry membrane to solution, *Polymer* **2000**, *41*, 5829-5838.
61. Loppinet, B; Gebel, G. Rodlike colloidal structure of short pendant chain perfluorinated ionomer solutions, *Langmuir* **1998**, *14*, 1977-1983.
62. Han, K. W.; Ko, K. H.; Abu-Hakmeh, K.; Bae, C.; Sohn, Y. J.; Jang, S. S. Molecular dynamics simulation study of a polysulfone-based anion exchange membrane in comparison with the proton exchange membrane, *J. Phys. Chem. C* **2014**, *118*, 12577-12587.
63. Omasta, T. J.;, Park, A. M.; LaManna,J. M.; Zhang,Y.; Peng, X.; Wang, L.; Jacobson, D. L.; Varcoe, J. R.; Hussey, D. S.; Pivovar, B. S. ; Mustain,W. E. *Energy Environ. Sci*, **2018**, 11, 551-558.
64. Holdcroft, S.; Wright, A.; Britton, B, Weissbach, T.; Peckham, T. J.; Ward, J. W. *US Patent* **2019**, 2019/0382353 A1.
65. Huang, T.; He, G.; Xue, J.; Otoo, O.; He, X.; Jiang, H.; Zhang, J.; Yin, Y.; Jiang, Z.; Douglin, C. J.; Dekel, D. R.; Guiver, M. D. Self-crosslinked blend alkaline anion exchange membranes with bi-continuous phase separated morphology to enhance ion conductivity, *J. Membr. Sci.*, **2020**, 597, 117769.
66. Zhang, X.; Cao, Y.; Zhang, M.; Wang, Y.; Tang, H.; Li, N. Olefin metathesis-crosslinked, bulky imidazolium-based anion exchange membranes with excellent base stability and

mechanical properties, *J. Membr. Sci.*, **2020**, 598, 117793.

67. Liu, L., Chu, X., Liao, J., Huang, Y., Li, Y., Ge, Z., Hickner, M. A., Li, N. Tuning the properties of poly(2,6-dimethyl-1,4-phenylene oxide) anion exchange membranes and their performance in H_2/O_2 fuel cells, *Energy Environ. Sci.*, **2018**, 11, 435-446.

Figure caption

Scheme 1 Schematic illustration of conducting/non-conducting two-phase system

Scheme 2 Preparation procedure for AEMs

Figure 1 Plots of (a) OH^- conductivities (σ_{OH^-}); (b) WU; (c) hydration number (λ_w) at RT as a function of effective IEC_{exp}

Figure 2 Time-dependence of relative OH^- conductivity (σ_t/σ_0) of AEMs with different IECs after immersion in a 1-M KOH solution at 80°C

Figure 3 SANS profiles measured for AEMs with different IECs (a) at dry condition and (b) equilibrated in D_2O at room temperature. The vertical dashed line indicates the boundary between two *q*-Regions. (c) Plot of d_2 as a function of IEC

Figure 4 Schematic illustrations of the structure model for the ideal two-component system (a) "reverse-micelles", and (b) "micelles"

Figure 5 Highlighted SANS profiles (symbols) in Region II of Figure 3(b) for AEMs with different IECs. The best-fitted theoretical profiles (solid line), which are based on the HS-liquid model analysis, are also shown in the figure.

Figure 6 Porod plot of SANS profiles shown in Figure 3(b)

Figure 7 Plots of (a) V_S, V_w, and V_{graft}; (b) R_S, $R_{Porod,w}$, and $R_{Porod,g}$; and (c) S and n_{ion}, as a function of GD. The regions marked with dotted circles indicate good consistency of V_S with V_w or V_{graft} (part a), and of R_S with $R_{Porod,w}$ or $R_{Porod,g}$ (part b) to verify the applicability of "reverse-micelles" or "micelles" models.

Figure 8 Schematic illustrations of the structure models in the conducting phase of (a) "reverse-micelles" model for AEMs with IEC < IEC_c; (b) "micelles" model for AEMs with IEC > IEC_c; and the correlations of water uptake and membrane alkaline stability in the structure models of (c) "reverse-micelles" and (d) "micelles"

Figure 9 Performance tests of MEA fabricated with AEM42 as a membrane, and AEM98 as an ionomer: (a) Polarization curve and power density at 80°C, 100 mL/min oxygen

flow rate, and 20 mL/min hydrazine hydrate with 10 KPa backpressure at the cathode side; (b) OCV-hold test at 80°C, 100 mL/min oxygen flow rate, and 20 mL/min hydrazine hydrate without backpressure

Table 1 Characteristics of AEMs equilibrated in water at 25°C

AEMs	Grafting time (h)	GD (%)	WU (%)	λ_w	IEC_{cal} (mmol/g)	IEC_{exp} (mmol/g)	IEC_{exp} /IEC_{cal}	σ_0 (mS/cm) 60°C	RT	Time of σ_t /σ_0 ~ 20% (h)
AEM08	0.67	8	5.0	10.6	0.34	0.26	0.76	17	9	>600[1)]
AEM11	0.8	11	7.5	11.2	0.45	0.37	0.82	23	12	>600[1)]
AEM14	1.0	14	9	11.6	0.56	0.43	0.77	39	18	>600[1)]
AEM18	1.2	18	10	10.3	0.63	0.54	0.85	50	24	>600[1)]
AEM30	2.0	30	20	14.4	1.0	0.78	0.78	60	43	450
AEM42	4.0	42	42	24.6	1.15	0.95	0.83	97	56	320
AEM56	5.0	56	53	22.9	1.54	1.29	0.84	116	78	200
AEM86	10.0	86	74	26.8	1.8	1.53	0.85	156	92	< 72[1)]
AEM98	16.0	98	80	25.8	1.88	1.72	0.91	181	100	< 72[1)]

[1)] AEM08, AEM11, AEM14 and AEM18 did not show visible conductivity decrease during the durability test up to 600h. AEM86 and AEM98 were physically damaged after immersing in 1 KOH solution at 80 ºC for 3 days.

Table 2 d_2, ϕ_x of component x (x: graft, c-graft, and nc-graft) and V_w of AEMs equilibrated in water

AEMs	d_2 (Å)	ϕ_{graft}	$\phi_{c\text{-}graft}$[2)]	$\phi_{nc\text{-}graft}$[2)]	$\phi_{c\text{-}graft}$ /ϕ_{graft}	ϕ_{ETFE}	ϕ_w	V_{w1}	V_{w2}
AEM08	21.0	0.111	-	-	-	0.814	0.075	-	0.43
AEM11	21.0	0.141	-	-	-	0.753	0.106	-	0.44
AEM14	21.0	0.169	0.133	0.036	0.79	0.708	0.123	0.45	0.45
AEM30	22.0	0.261	-	-	-	0.513	0.226	-	0.50
AEM42	22.5	0.262	0.238	0.024	0.9	0.367	0.371	0.61	0.63
AEM56	23.4	0.284	-	-	-	0.298	0.418	-	0.62

AEM86	26.1	0.304	0.275	0.029	0.9	0.208	0.488	0.64	0.65

[2] $\phi_{c\text{-graft}}$ and $\phi_{nc\text{-graft}}$ are obtained from eqs. (S1)–(S4) in the Supporting Information

Table 3 R_S and V_S, obtained from the hard-sphere liquid model, and estimated V_w and V_{graft}

AEMs	R_S (Å)	V_S	V_w[3]	V_{graft}
AEM08	10.2	0.33	0.43	0.57
AEM11	10.5	0.39	0.44	0.56
AEM14	10.7	0.41	0.45	0.55
AEM30	11.0	0.38	0.50	0.50
AEM42	11.2	0.40	0.61	0.39
AEM56	11.6	0.40	0.62	0.38
AEM86	12.6	0.36	0.64	0.36

[3] Average value of V_{w1} and V_{w2} for AEM14, AEM42 and AEM86, and the value of V_{w2} for other AEMs shown in Table 3

Table 4 Parameters obtained from the Porod limit analysis

AEMs	$R_{Porod,w}$ (Å)	$R_{Porod,g}$ (Å)	Σ (Å^{-1})	S (Å^2)	n_{ion}
AEM08	11.9 Yes[4]	-	0.019	81	22
AEM11	11.8 Yes[4]	-	0.027	84	21
AEM14	11.7 Yes[4]	-	0.032	89	19
AEM30	-	-	0.029	93	-
AEM42	25.2 No[4]	14.8 Yes[4]	0.044	86	32
AEM56	23.8 No[4]	14.6 Yes[4]	0.053	87	31
AEM86	26.3 No[4]	14.2 Yes[4]	0.056	90	28

[4] Consistency with HS liquid model.

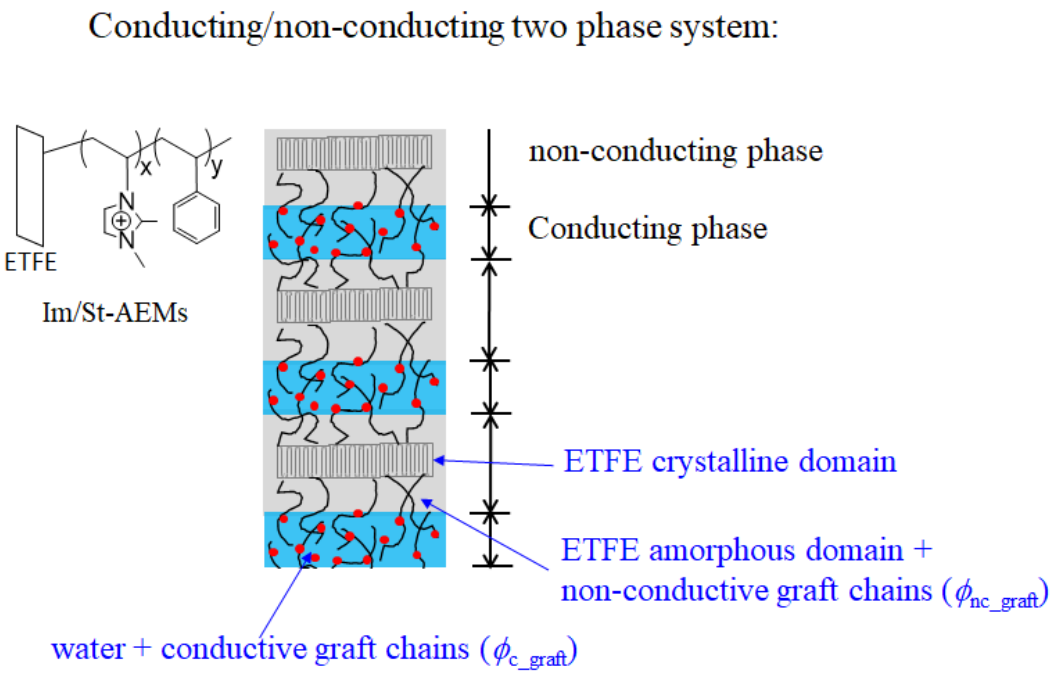

Scheme 1

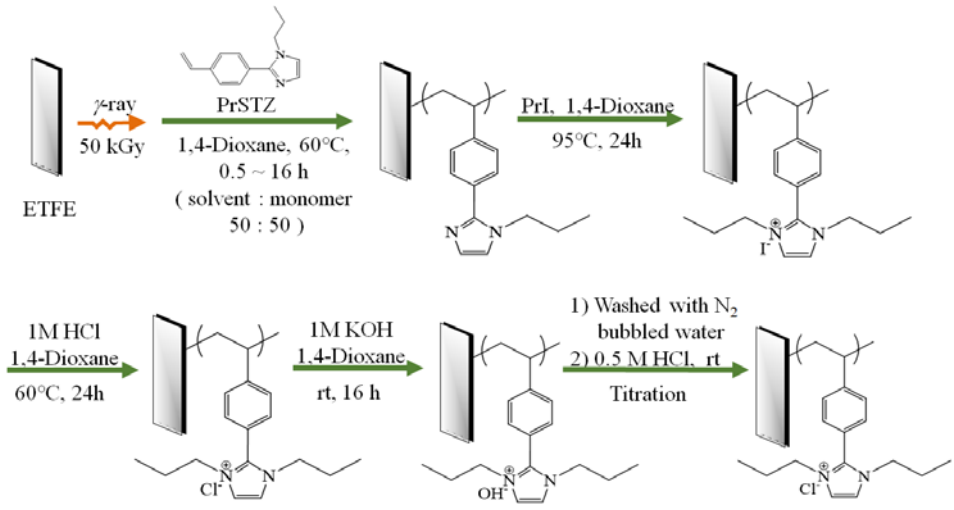

Scheme 2

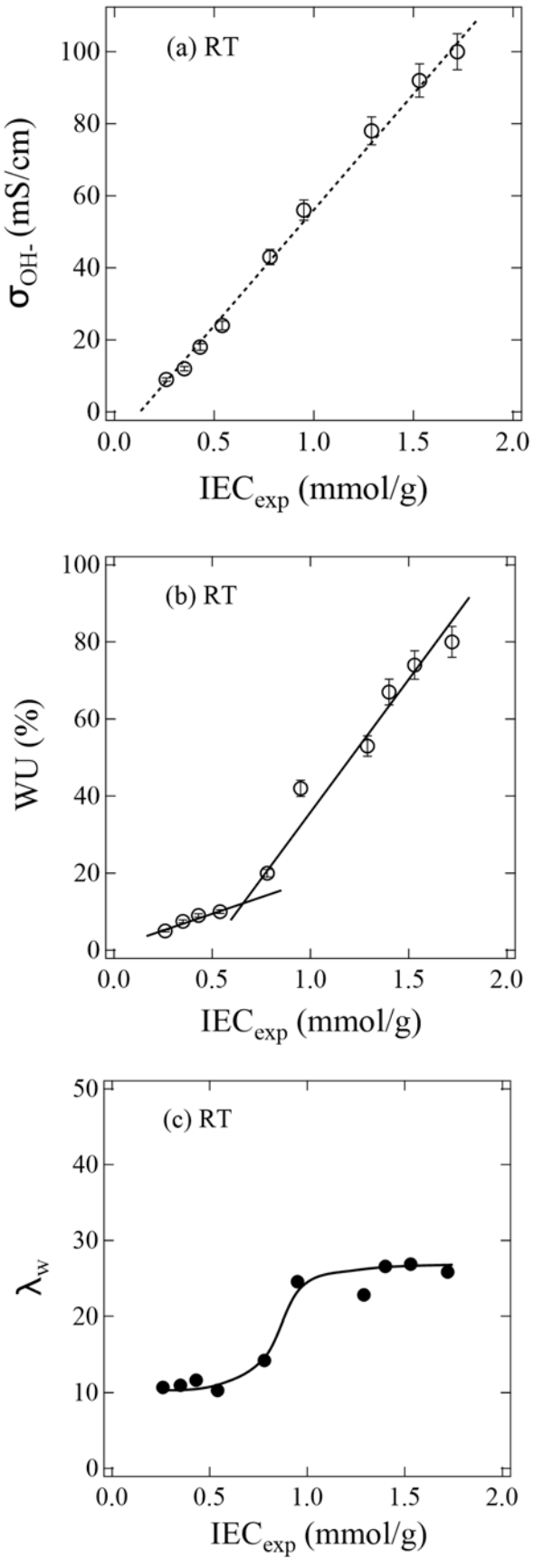
(a) RT
σ_{OH^-} (mS/cm)
IEC_{exp} (mmol/g)
(b) RT
WU (%)
IEC_{exp} (mmol/g)
(c) RT
λ_w
IEC_{exp} (mmol/g)

Figure 1

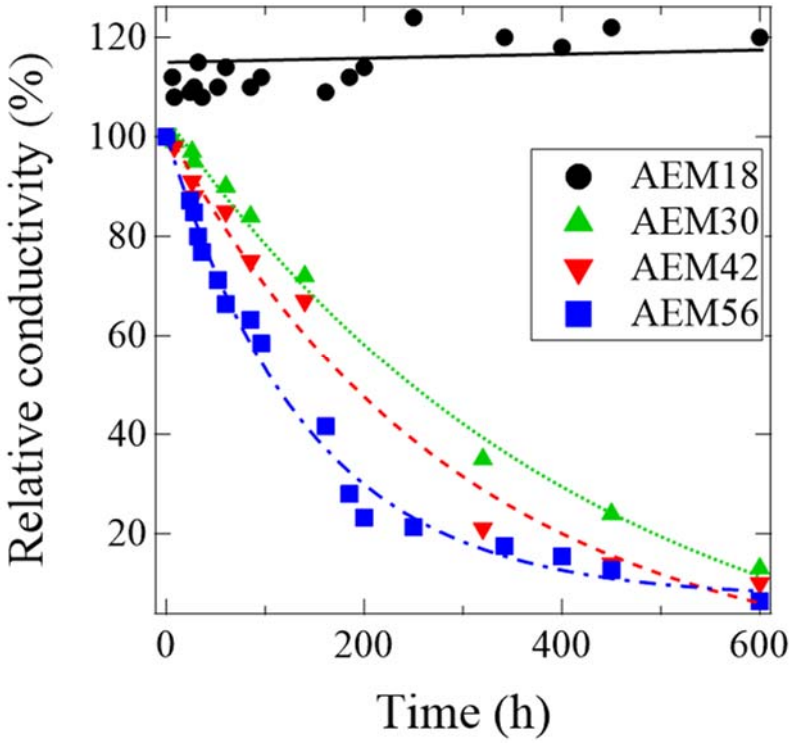
Relative conductivity (%)
120
100
80
60
40
20
0
200
400
600
Time (h)
AEM18
AEM30
AEM42
AEM56

Figure 2

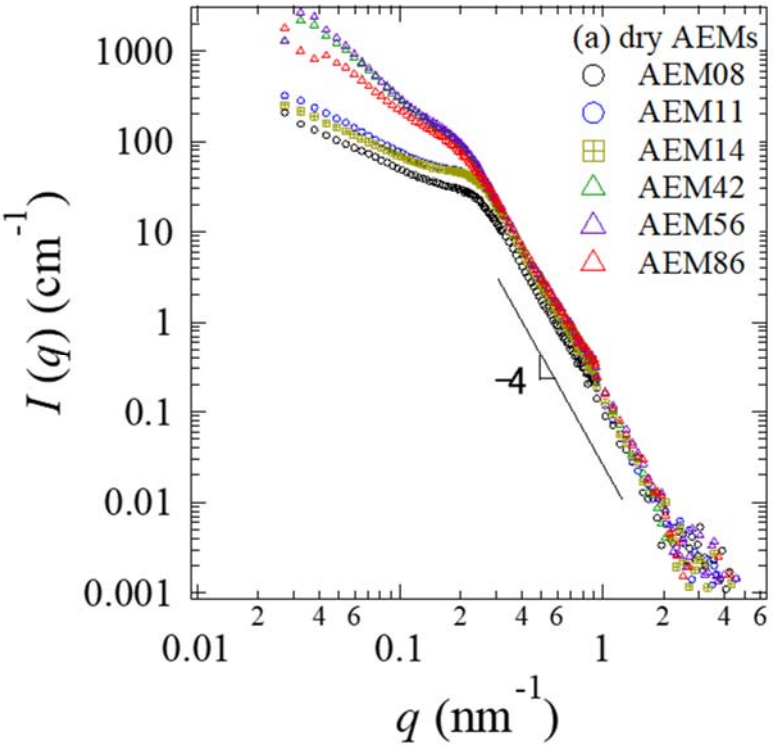
(a) dry AEMs
AEM08
AEM11
AEM14
AEM42
AEM56
AEM86
-4
1000
100
10
1
0.1
0.01
0.001
0.01
0.1
1
I (q) (cm-1)
q (nm-1)

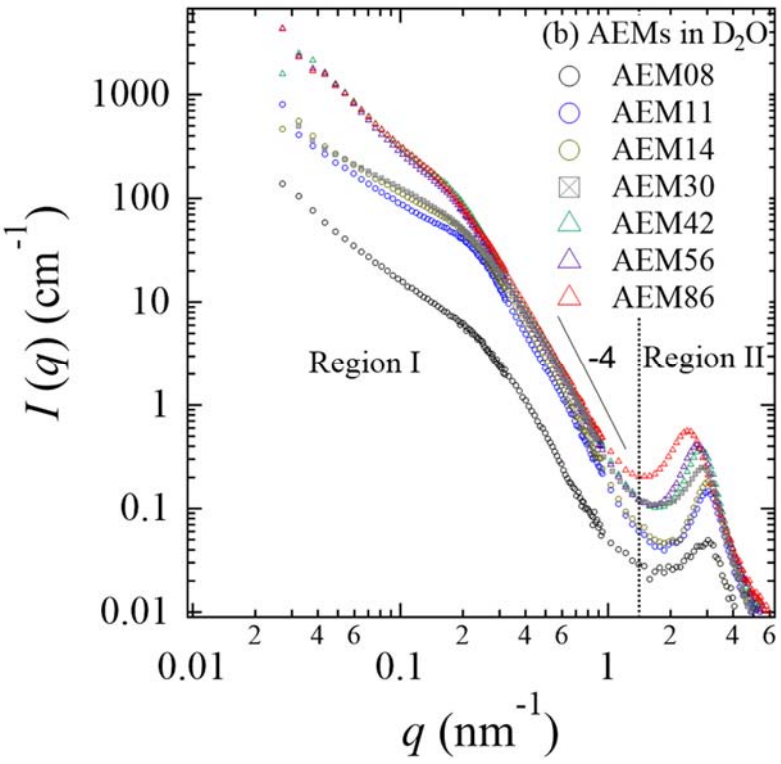
(b) AEMs in D2O
AEM08
AEM11
AEM14
AEM30
AEM42
AEM56
AEM86
Region I
-4
Region II
1000
100
10
1
0.1
0.01
0.01
0.1
1
I (q) (cm-1)
q (nm-1)

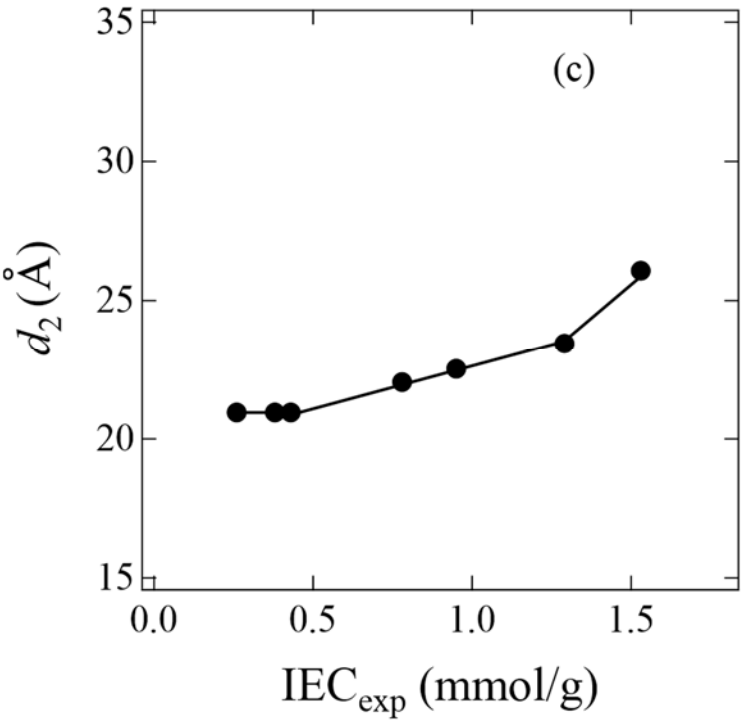

Figure 3

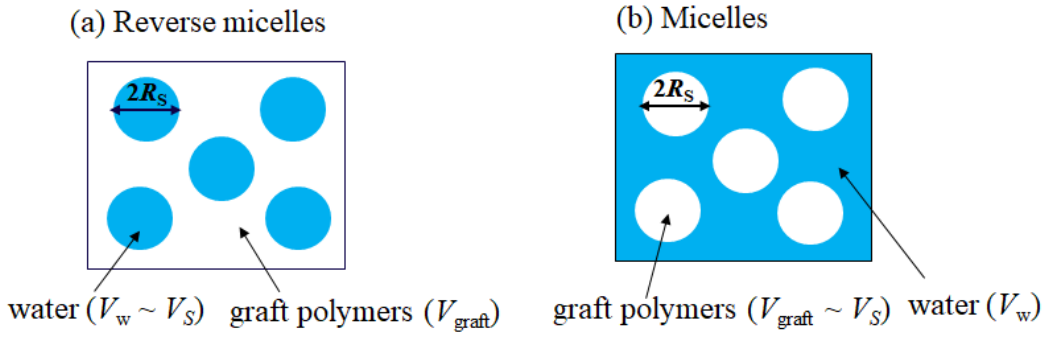

Figure 4

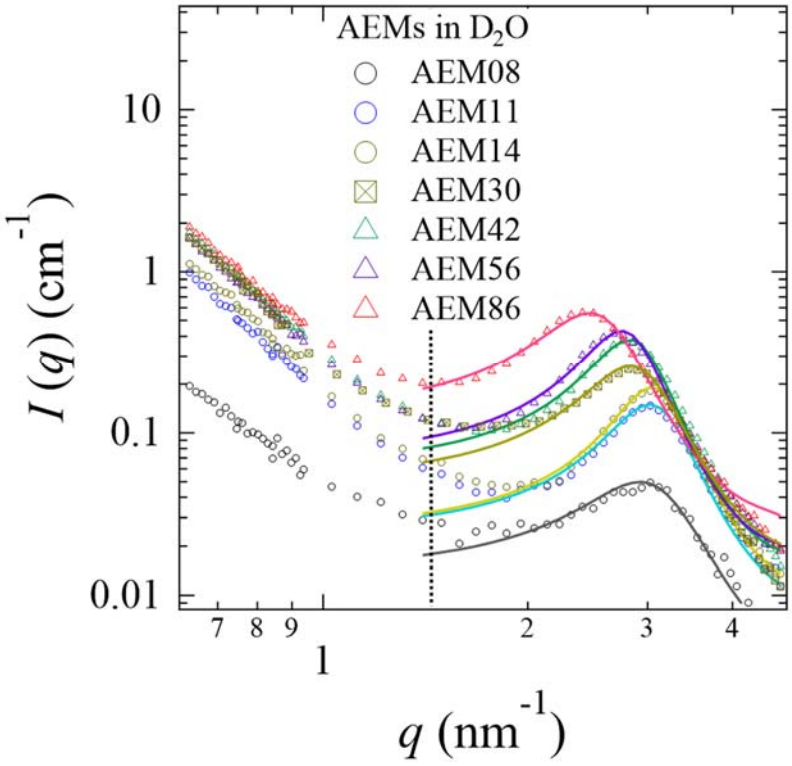
AEMs in D2O
AEM08
AEM11
AEM14
AEM30
AEM42
AEM56
AEM86
10
1
0.1
0.01
I (q) (cm-1)
7 8 9
1
2
3
4
q (nm-1)

Figure 5

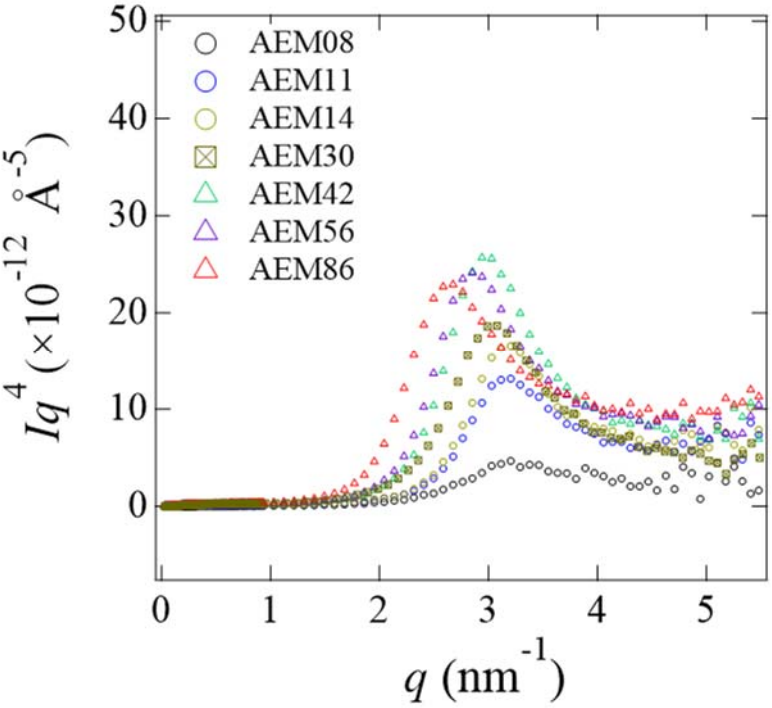
AEM08
AEM11
AEM14
AEM30
AEM42
AEM56
AEM86
Iq^4 ($\times 10^{-12}$ Å^{-5})
q (nm^{-1})
0
10
20
30
40
50
0
1
2
3
4
5

Figure 6

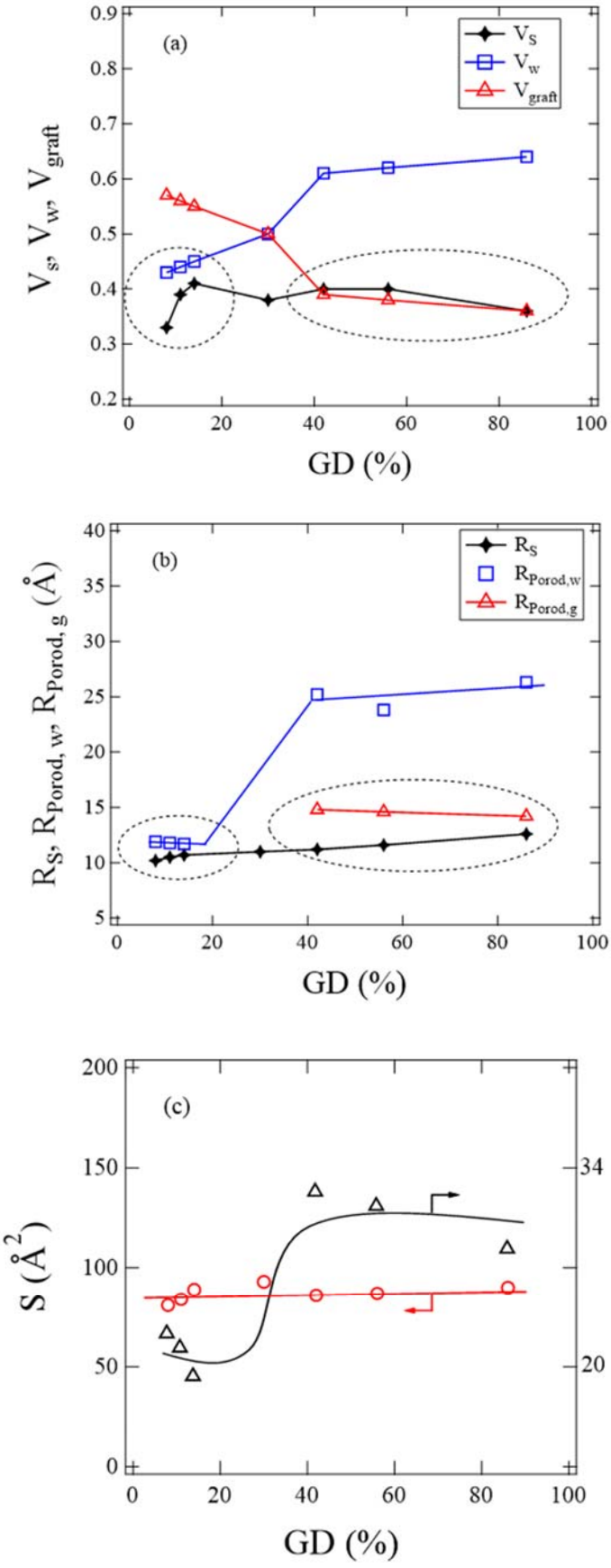
(a)
V_S
V_w
V_{graft}
V_S, V_w, V_{graft}
GD (%)
(b)
R_S
$R_{Porod,w}$
$R_{Porod,g}$
R_S, $R_{Porod,w}$, $R_{Porod,g}$ (Å)
GD (%)
(c)
S (Å^2)
n_{ion}
GD (%)

Figure 7

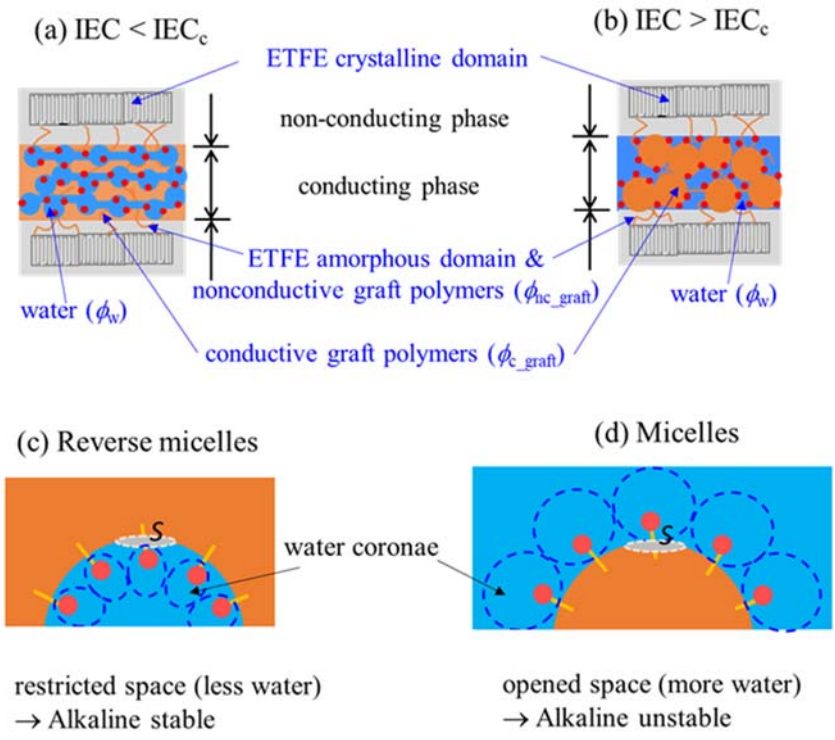
(a) IEC < IEC$_c$
(b) IEC > IEC$_c$
ETFE crystalline domain
non-conducting phase
conducting phase
ETFE amorphous domain &
nonconductive graft polymers (ϕ_{nc_graft})
conductive graft polymers (ϕ_{c_graft})
water (ϕ_w)
water (ϕ_w)
(c) Reverse micelles
(d) Micelles
water coronae
S
S
restricted space (less water)
→ Alkaline stable
opened space (more water)
→ Alkaline unstable

Figure 8

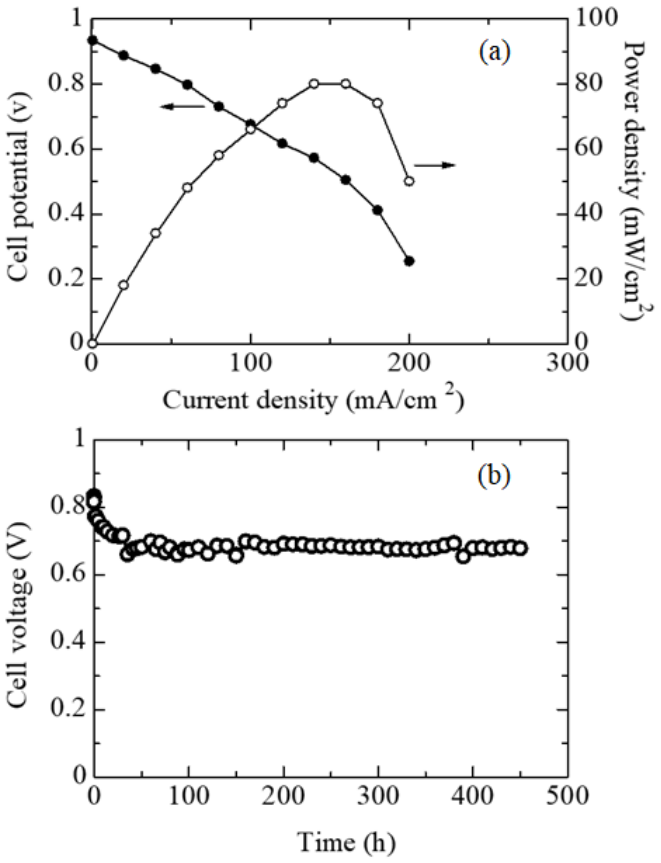
(a)
Cell potential (v)
Power density (mW/cm^2)
Current density (mA/cm ^{2})
0
0.2
0.4
0.6
0.8
1
0
20
40
60
80
100
0
100
200
300
(b)
Cell voltage (V)
Time (h)
0
100
200
300
400
500

Figure 9

A long side chain imidazolium-based graft-type anion exchange membrane: Novel electrolyte and alkaline durable properties and the structural elucidation using SANS contrast variation

Yue Zhao,[1,*] Kimio Yoshimura,[1] Ahmed Mohamed Ahmed Mahmoud,[1] Hwan-Chul Yu,[1] Shun Okushima,[1] Akihiro Hiroki,[1] Yoshihiro Kishiyama,[2] Hideyuki Shishitani,[2] Susumu Yamaguchi,[2] Hirohisa Tanaka,[3] Yohei Noda,[4] Satoshi Koizumi,[4] Aurel Radulescu,[5] Yasunari Maekawa[1,*]

S1. Determination of $\phi_{\text{nc-graft}}$ and $\phi_{\text{c-graft}}$. Same as we reported in ref. 20, a specific matching point exists in the 2-phase system to make the scattering intensity minimum, at which the scattering length density (SLD) of phase 1 (b_1) is close to that of phase 2 (b_2), namely, $b_1 \approx b_2$. This criterion allows us to determine the distribution of graft polymer in phases 1 and 2 in a quantitative manner. To search the matching point, the evolution of $I(q_1)^{1/2}$ with the volume fraction of D_2O in the water mixture, f_{D2O}, is presented in Figure S5. The volume fraction of D_2O at the matching point ($f_{D2O,m}$) was determined from the minimum value of $I(q_1)^{1/2}$ to be about 70%, 60%, and 56% for AEM14, AEM42, AEM86, respectively.

Obviously, $\phi_{\text{nc-graft}}$ and $\phi_{\text{c-graft}}$ also satisfy Eq. (S1) below:

$$\phi_{\text{nc-graft}} + \phi_{\text{c-graft}} = \phi_{\text{graft}} \qquad \text{(S1)}$$

It is worthy to note that the SLD of the non-conducting phase (b_1) is a constant, being independent of f_{D2O} due to the strong immiscibility with water. The SLD of the conducting phase (b_2), however, varies with the incorporated water. b_1 or b_2 can be given in terms of $\phi_{\text{nc-graft}}$ and $\phi_{\text{c-graft}}$ as shown in the following equations:

$$b_1 = \frac{\phi_{nc-graft} b_{graft} + \phi_{ETFE} b_{ETFE}}{\phi_{nc-graft} + \phi_{ETFE}} \qquad \text{(S2)}$$

$$b_2 = \frac{\phi_{c-graft} b_{graft} + \phi_w b_w}{\phi_{c-graft} + \phi_w} \qquad \text{(S3)}$$

where b_X (X= graft, ETFE or w, represents graft polymer, ETFE or water, respectively) means the SLD of X, which can be calculated theoretically according to the molecular structure and the mass density of X.[20] Thus $b_{graft} = 1.07 \times 10^{10}$ cm^{-2}. The exact mass density of either ETFE crystalline or amorphous chain is unknown; however, plenty of previous reports showed that the scattering intensity of the neat ETFE base films is very weak, suggesting a negligible small difference in the SLD of ETFE crystalline and amorphous domains.[14, 16, 20] Therefore, it is reasonable to use the average mass density of ETFE film of ~1.7 g/cm^3 to roughly estimate the SLD of ETFE crystalline and amorphous domains to be ~ 2.7×10^{10} cm^{-2}. b_w is a function of f_{D2O} given by

$$b_w = b_{D2O} f_{D2O} + b_{H2O}(1 - f_{D2O}) \qquad \text{(S4)}$$

where b_{D2O} and b_{H2O} are the SLD of D_2O and H_2O being 6.34 and -0.56 ($\times 10^{10}$ cm^{-2}), respectively.[36]

At the matching point of $f_{D2O,m}$, Eqs. (S2) and (S3) were equivalent to each other. In conjunction with Eq. (S1), we can accurately estimate $\phi_{nc\text{-}graft}$ and $\phi_{c\text{-}graft}$ for each AEM as listed in Table 2.

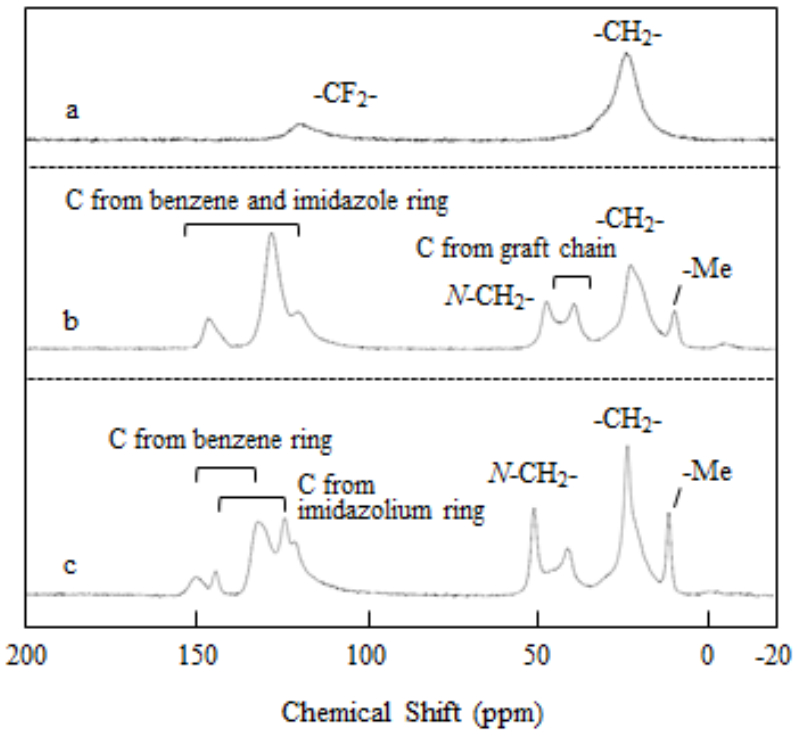

Figure S1 ^{13}C solid-state NMR spectrum of (a) ETFE, (b) poly(StIm)-grafted ETFE with a grafting degree of 46%, (c) StIm-AEM with a grafting degree of 50% in Cl^- form.

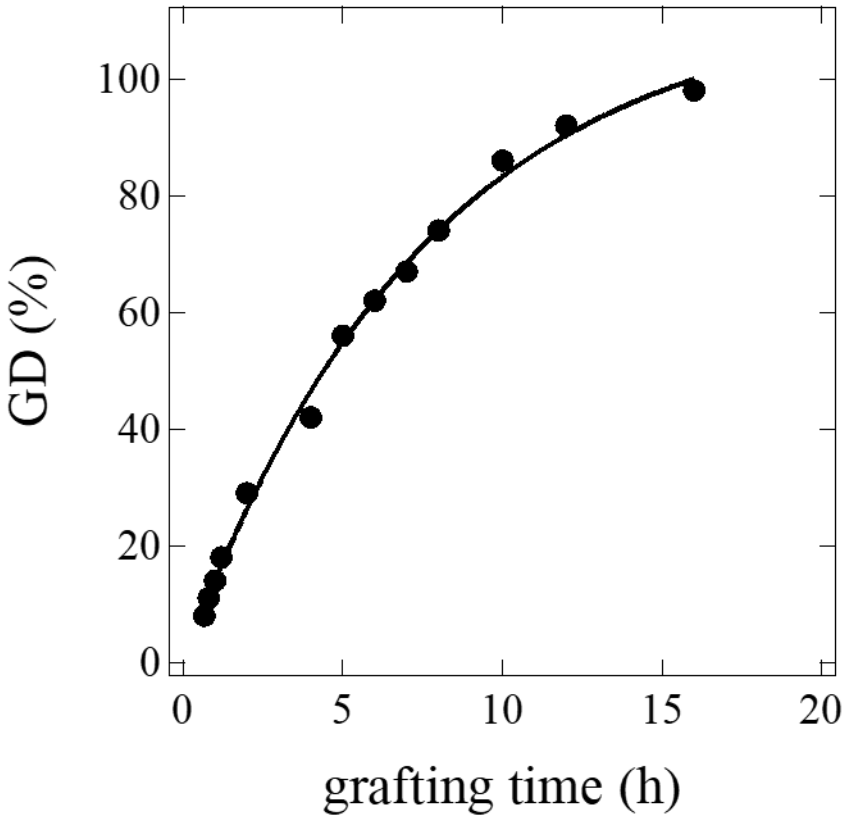

Figure S2 Plot of GD as a function of grafting polymerization time

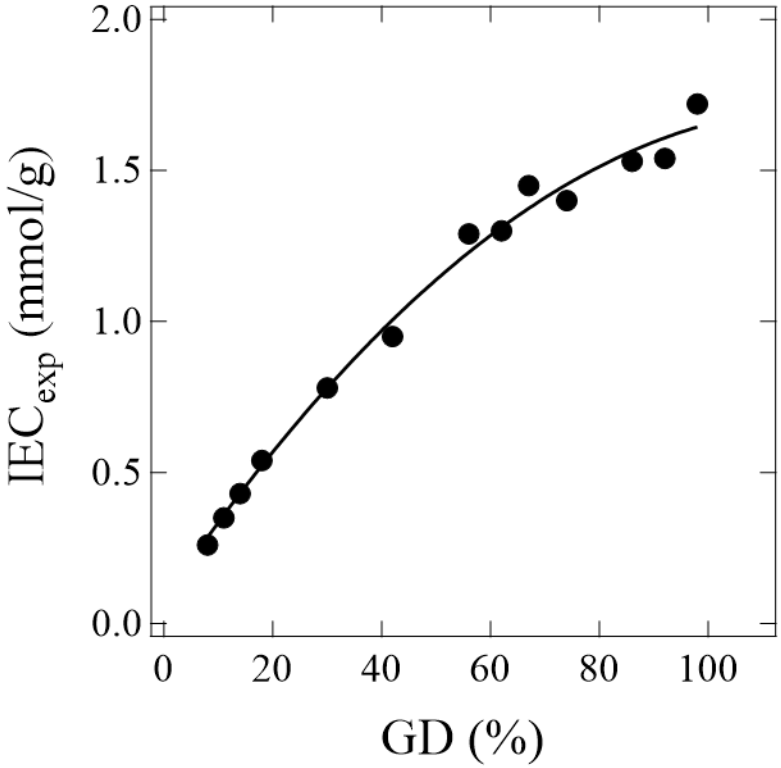

Figure S3 Plot of effective IEC_{exp} as a function of GD.

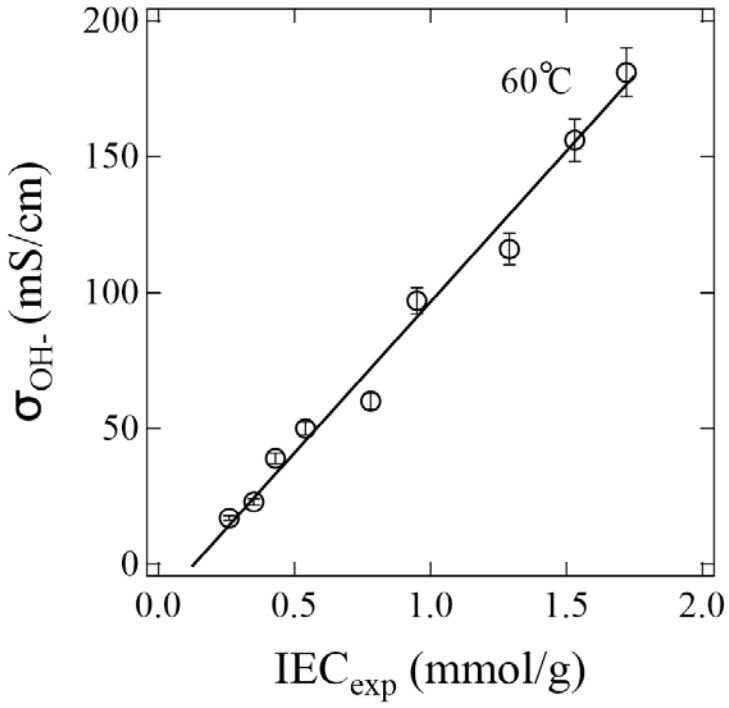

Figure S4 Plot of σ_{OH^-} at 60 °C as a function of IEC_{exp}.

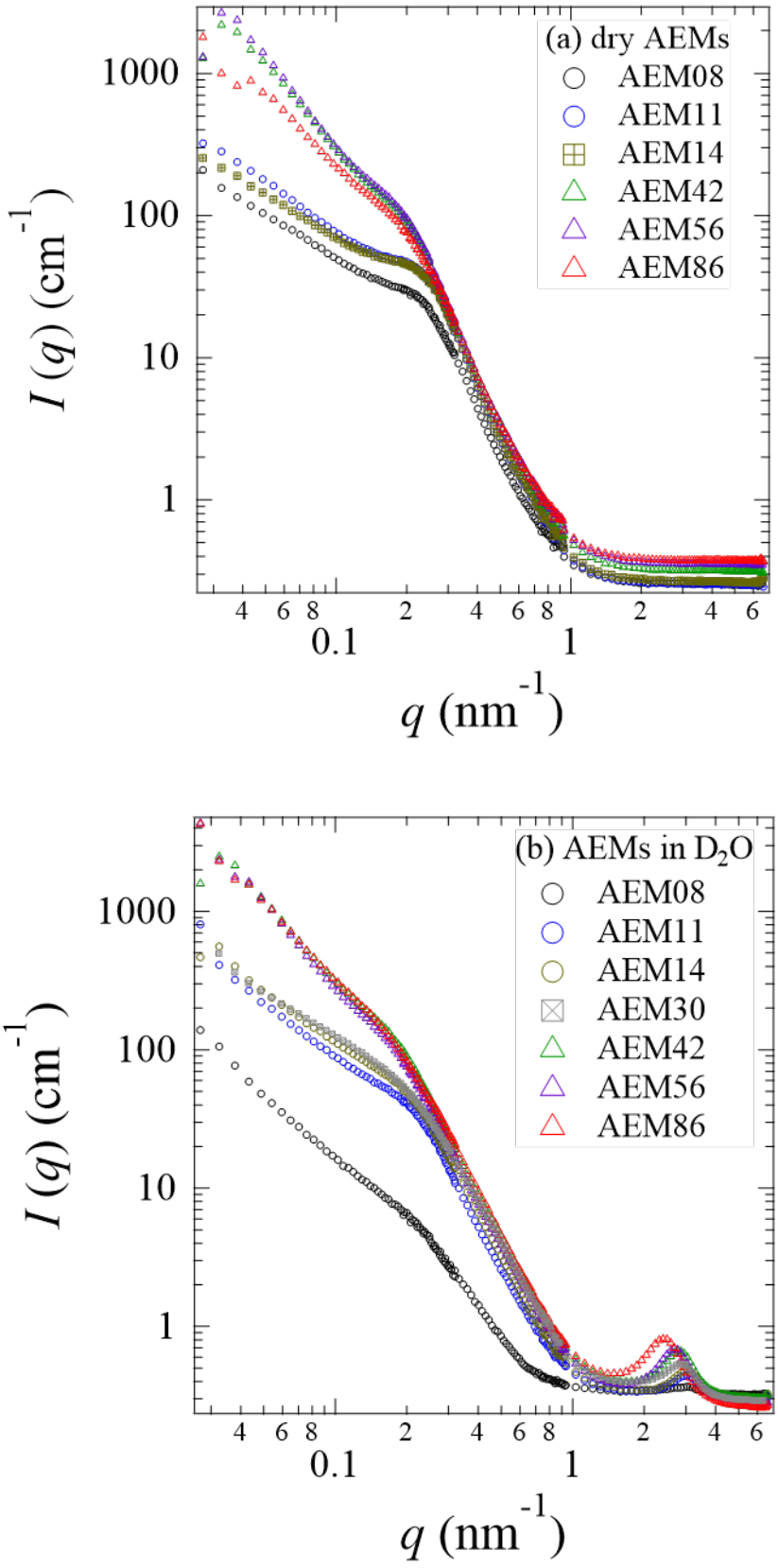

Figure S5 SANS intensity profiles of (a) dry AEMs and (b) AEMs equilibrated in D_2O, with different GDs equilibrated in D_2O before incoherent scattering correction.

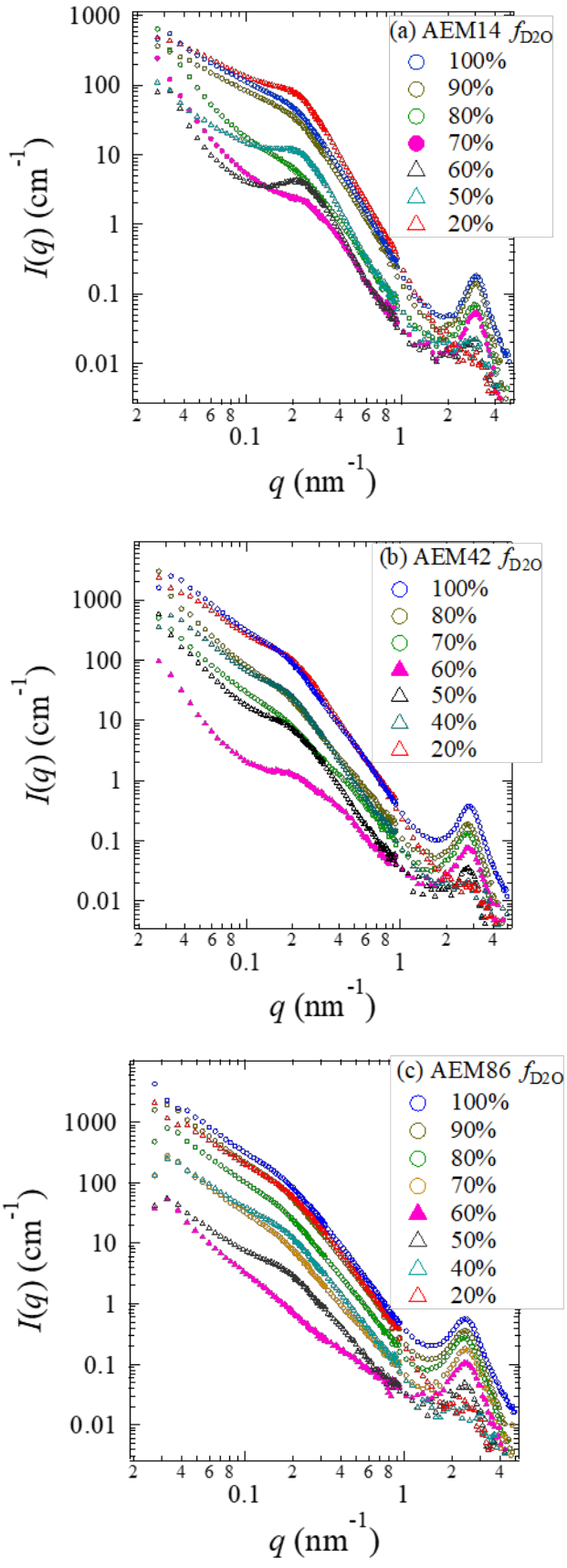

Figure S6 SANS profiles obtained from (a) AEM14; (b) AEM42; and (c) AEM86 equilibrated in water mixture with different representative f_{D2O}.

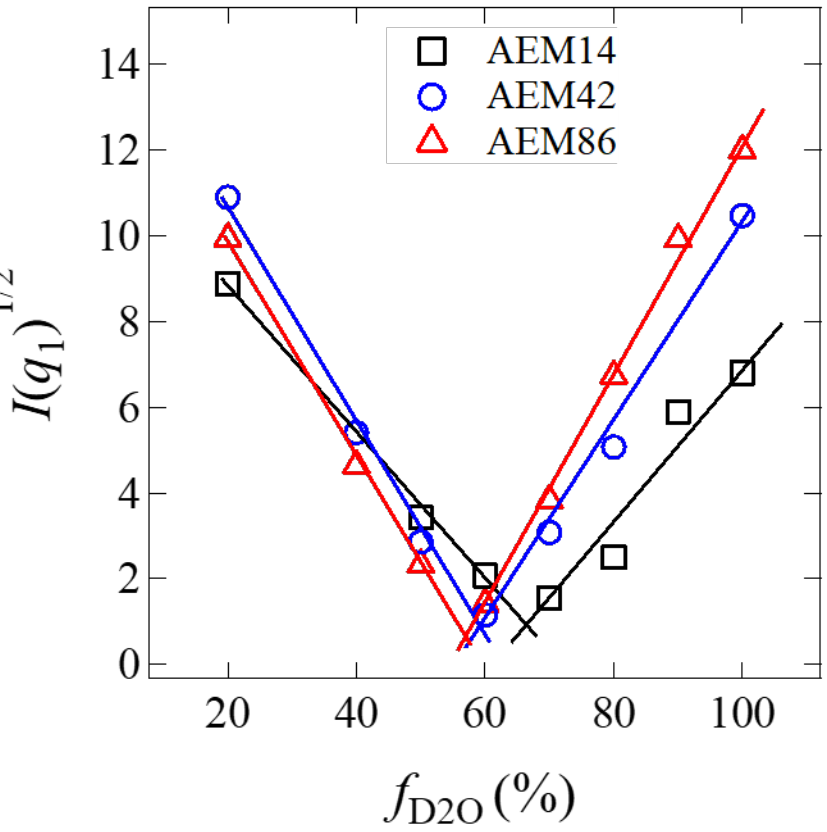

Figure S7 The volume fraction f_{D2O} dependence of $I(q_1)^{1/2}$ observed for AEMs equilibrated in H_2O/D_2O water mixtures shown in Figure S4.

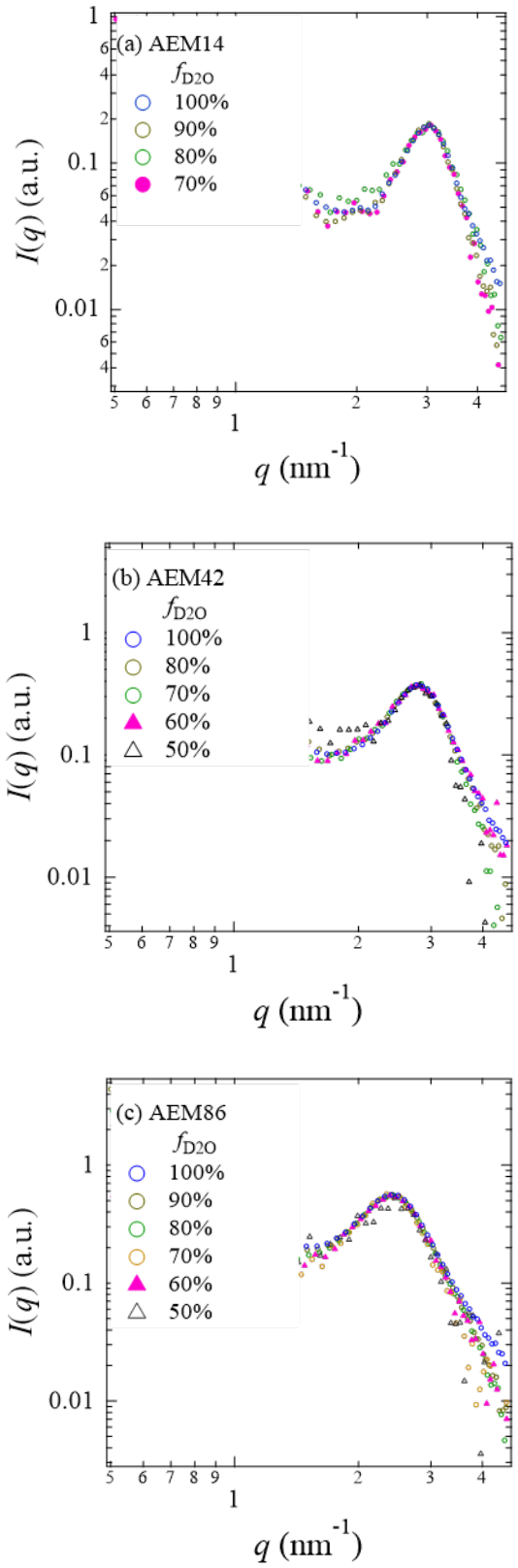

Figure S8 Vertically shifted SANS profiles around the ionomer peak for (a) AEM14; (b) AEM42; and (c) AEM86 equilibrated in H_2O/D_2O water mixtures with representative f_{D2O}.

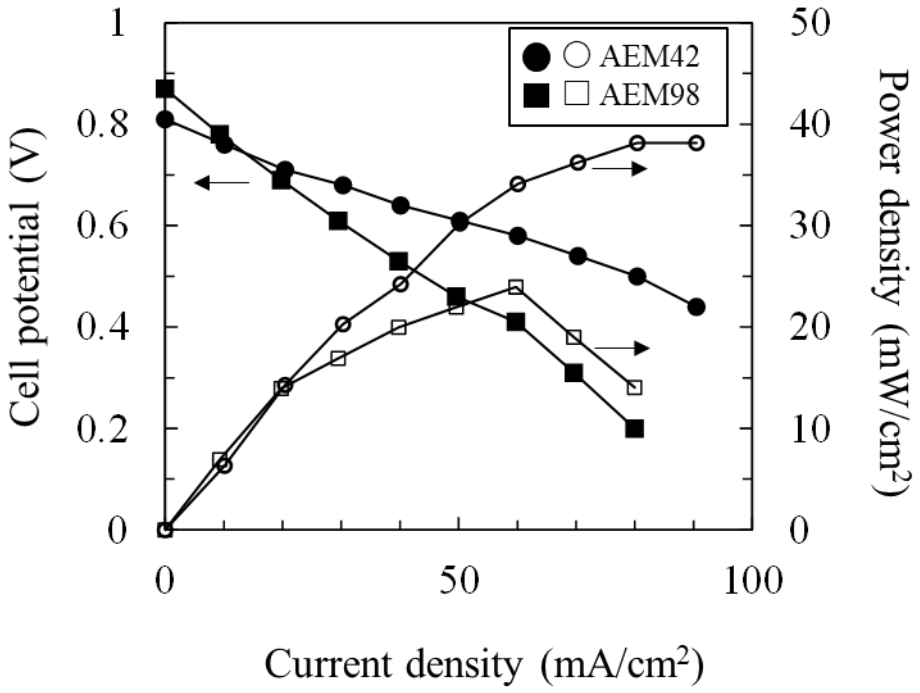

Figure S9 Polarization curve and power density of the single hydrazine hydrate fuel cell fabricated with AEM42 or AEM98 as a membrane, and BTMA as an ionomer at 80°C, 50 mL/min oxygen flow rate, and 20 mL/min hydrazine hydrate with 10 KPa backpressure at the cathode side.

A long side chain imidazolium-based graft-type anion-exchange membrane: novel electrolyte and alkaline-durable properties and structural elucidation using SANS contrast variation

Yue Zhao,[1,*] Kimio Yoshimura,[1] Ahmed Mohamed Ahmed Mahmoud,[1] Hwan-Chul Yu,[1] Shun Okushima,[1] Akihiro Hiroki,[1] Yoshihiro Kishiyama,[2] Hideyuki Shishitani,[2] Susumu Yamaguchi,[2] Hirohisa Tanaka,[3] Yohei Noda,[4] Satoshi Koizumi,[4] Aurel Radulescu,[5] Yasunari Maekawa[1,*]

[1]*Department of Advanced Functional Materials Research, Takasaki Advanced Radiation Research Institute, National Institutes for Quantum and Radiological Science and Technology (QST), Watanuki-machi 1233, Takasaki, Gunma, 370-1292, Japan*
[2]*Daihatsu Motor Co., Ltd., Ryuo Gamo, Shiga 520-2593, Japan*
[3]*School of Science and Technology, Kwansei Gakuin University, 2-1 Gakuen, Sanda, Hyogo 669-1337 Japan*
[4]*Department of Engineering, Ibaraki University, Hitachi 316-8511, Japan*
[5]*Forschungszentrum Jülich GmbH, Jülich Centre for Neutron Science @ MLZ, Lichtenbergstraße 1, D-85747 Garching, Germany*

*To whom all correspondence should be addressed: Yue Zhao (zhao.yue@qst.go.jp); Yasunari Maekawa (maekawa.yasunari@qst.go.jp)

ABSTRACT: Newly designed styrylimidazolium-based grafted anion-exchange membranes (StIm-AEMs), in which imidazolium ionic groups are attached to styrene at the far side from the graft chains, were prepared by radiation-induced graft polymerization of *p*-(2-imidazoliumyl) styrene onto poly(ethylene-*co*-tetrafluoloethylene) (ETFE) films, followed by *N*-alkylation and ion-exchange reactions. StIm-AEM having an ion exchange capacity (IEC) of 0.54 mmol/g with a grafting degree (GD) of ~18%, possesses practical conductivity (>50 mS/cm) even with a very low water uptake (~10%) and high stability over 600 h in a 1-M KOH solution at 80°C. There exists a critical IEC (IEC_c) in the range of 0.7–0.8 mmol/g over which the membrane showed high water uptake, which resulted in pronounced susceptibility to hydrolysis. Using small-angle neutron scattering technique with a contrast variation method, we found the hydrophilic phase in StIm-AEMs with IECs lower and higher than IEC_c shows "reverse-micelles" with water domains dispersed in the polymer matrix and "micelles" with graft polymer aggregates dispersed in the water matrix, respectively. The further analysis of micelle structures using the hard-sphere liquid model and Porod limit analysis reveals that the interfacial structures of ionic groups are essential for the electrochemical properties and durability of StIm-AEMs. In addition, StIm-AEM with an IEC of 0.95 mmol/g and the maximum power density of 80 mW/cm^2 in the hydrazine hydrate fuel cell test, exhibited long-term durability under constant current (8.0 mA) up to 455 h, which, thus far, is the best durability at 80°C for platinum-free alkaline-type liquid fuel cells.

I. Introduction

Anion-exchange membrane (AEM) fuel cells represent a new generation of potentially disruptive, low-temperature fuel cell technology with the potential to eliminate the high-cost barriers of mainstream proton exchange membrane (PEM) fuel cells.[1-13] However, the performance of AEM fuel cells is not as good as that of PEM fuel cells, especially the membrane conductivity and long-term durability. The knowledge of AEM materials is still limited, including molecular design, hierarchical structures in the membrane, and structure/property relationships.[8-13]

To fabricate AEMs, a radiation grafting technique is a promising method. It allows to introduce many ion-conducting groups (as graft polymers to achieve high ion conductivity) into mechanically and thermally stable polymer base films with the retention of the original properties of these polymers.[14-28] In the past years, we intensively developed both AEMs and PEMs that were based on fluorinated polymers or fully aromatic hydrocarbon polymer films using this method.[15–21] Recently, we applied the radiation grafting method to prepare imidazolium-type AEMs on poly(ethylene-*co*-tetrafluoroethylene) (ETFE) base films. AEMs exhibited lower water uptake (WU) and higher alkaline stability than the corresponding AEMs containing trimethylammonium hydroxide owing to the low basicity of imidazolium hydroxide as an Arrhenius base.[8-10] Furthermore, AEMs containing weak base imidazolium groups induced low damage to polymer backbones through self-base-catalyzed degradation.[10] To suppress β-elimination and ring-opening hydrolysis of imidazolium groups,[17] we improved AEMs by grafting 2-methyl-*N*-vinylimidazole (Im), which has a methyl-protecting group at the imidazole C-2 position and co-grafting with hydrophobic styrene (St) into ETFE to obtain Im/St-AEMs.[17-21]

We investigated detailed structures and interplay between the structure and properties of these Im/St-AEMs in our latest work using the small-angle neutron scattering (SANS) technique with a contrast variation method.[18, 20] The main structural features were summarized

as follows. (1) The membranes can be characterized as a "conducting/non-conducting two-phase" system, as illustrated in Scheme 1. The conducting phase is composed of water and the majority of graft polymers where both Im and St units are covalently bonded to each other and behave coordinately. The non-conducting phase is made of ETFE chains, and the rest parts of graft polymers are constrained in amorphous ETFE domains. This model allows to evaluate the distribution of graft polymers in both conducting and non-conducting phases in a quantitative manner and is generally applicable for grafted polymer materials. (2) AEMs containing grafts with low hydrophobicity (*i.e.*, low St content) exhibit a homogeneous conducting phase with hydrated dispersed ions; thus, conductivity increases with an increase in the hydration level. In contrast, AEMs containing graft polymers with more hydrophobic units (St) exhibit a heterogeneous conducting phase, in which 3–4-nm in diameter water puddles are dispersed in the hydrophilic water/graft polymer phase. It was also determined that anion transport and membrane alkaline durability were suppressed by the water puddle structure.[21] Therefore, an increase in the hydrophobicity of graft polymers introduces the morphological transition from a homogeneous to heterogeneous conducting phase, and the resultant water puddles enhance β-elimination and hydrolysis degradation reactions.[21]

To further improve alkaline durability, in this study, we design a new molecular structure, styrylimidazolium (StIm), in which imidazolium groups are connected with St groups in perpendicular orientations, as shown in Scheme 2. This molecular design satisfies the complete removal of β-elimination reactions and hydrolysis of imidazolium rings. Contrary to the parallelly arranged Im and St groups in previous copolymer-type Im/St-AEMs, new AEMs are expected to have a clear phase separation between hydrophilic cationic headgroups and hydrophobic graft polymer chains, which may efficiently reduce WU and hydrolysis reaction. Because the ion-exchange capacity (IEC) of AEMs is the most crucial parameter, which determines their properties (e.g., conductivity, WU, mechanical strength, and durability), we systematically prepared a series of AEMs containing different GDs, which almost linearly

correspond to IEC, to investigate electrochemical properties and durability of AEMs and to elucidate the relationship between these properties and hierarchical structures of the membranes. Such studies are important and relevant to establish improved design rules for fuel cell membranes.

II. Experimental details

II-1 Materials

ETFE films [Tefzel 100LZ, mass density (d_{ETFE}) = 1.7 g/cm^3, crystallinity (X_c) = 0.36] with a thickness of 25 μm were purchased from DuPont and used as a base film. Iodopropane was purchased from Tokyo Chemical Industry Co., Ltd. Sodium hydride (50–72% in oil), St, hexane, *N,N*-dimethylformamide (DMF), ethanol, potassium carbonate (K_2CO_3), potassium hydroxide (KOH), hydrochloric acid (HCl), and a 0.1 mol/L sodium hydroxide solution (NaOH) were purchased from Wako Pure Chemical Industries, Ltd. These chemicals were used without further purification. 1,4-Dioxane and dichloromethane (CH_2Cl_2) were obtained from Kishida Chemical Co., Ltd. Deuterated water (99.9 atom% D) was purchased from Sigma-Aldrich Co. Ltd. Water used in experiments was purified using a Millipore Milli-Q UV system and had a resistance of 18.2 MΩ cm and the total organic carbon content of <10 ppb.

II-2 Preparation of AEMs

2-(4-Ethenylphenyl)-1*H*-imidazole was prepared according to the literature.[29] Sodium hydride in oil (1.32 g, 31.5 mmol) was washed with hexane (2 mL × 2) in a two-necked round bottom flask (100 mL) under nitrogen atmosphere. Then, DMF (20 mL) was added to the flask. 2-(4-Ethenylphenyl)-1*H*-imidazole (5.10 g, 30.0 mmol) was slowly added with a spatula over 10 min under stirring. The resultant solution was stirred for 30 min at room temperature; then, iodopropane (5.18 g, 30.5 mmol) in DMF (5 mL) was injected via syringe for 10 min. After additional 16 h of stirring at room temperature, the solution was quenched by water (15 mL). The aqueous layer was saturated with K_2CO_3 and extracted with CH_2Cl_2 (200 mL × 2). The extract was dried over magnesium sulfate (10 g). After CH_2Cl_2 was evaporated, the obtained

brown oil was dissolved in hexane (400 mL) and passed through Celite® Hyflo Supercel to obtain pure 2-(4-ethenylphenyl)-*N*-propylimidazole (StIm) as an orange-colored oil (4.78 g, 75% yield).

ETFE films (5.0 cm × 5.0 cm) were put in a Schlenk tube and irradiated using a ^{60}Co γ-ray source (QST Takasaki, Gunma, Japan) at room temperature in argon atmosphere with a total dose of 50 kGy at the dose rate of 10 kGy h^{-1}. Pre-irradiated ETFE films were immediately immersed in argon-purged monomer solutions (7 mL) consisting of StIm in 1,4-dioxane (50 wt%), followed by heating under argon atmosphere at 60°C for 0.67 to 16 h. Grafted ETFE was taken out, washed three times using 100 mL of 1,4-dioxane at room temperature, and refluxed in 200 mL of ethanol for 2 h to extract residual monomers and homopolymers. The obtained films were dried under vacuum at 80°C for 4 h.

For *N*-alkylation, grafted films were immersed in a 1-M dioxane solution of iodopropane (120 mL) at 60°C for 24 h. The films were washed several times using 30 mL of dioxane. Then, the films were immersed in 120 mL of a 1-M HCl/dioxane solution (50/50 vol%) to be transform from iodide (I^-) to chloride (Cl^-) forms. The solution was replaced three times every hour to ensure the completion of the ion-exchange reaction. The films were removed from the solution and washed using deionized water. Finally, the films were dried in a vacuum oven at 80°C for 24 h.

Then, AEMs in the chloride form were soaked in a 1-M KOH aqueous solution (100 mL) at room temperature for 6 h or in a 1-M $NaHCO_3$ aqueous solution (100 mL) to replace chloride (Cl^-) in the film to hydroxide (OH^-) and (HCO_3^-).[17-21] The molecular structure of graft polymers was confirmed by ^{13}C solid-state NMR spectroscopy, as shown in Figure S1 in the Supporting Information.

ETFE-based benzyltrimethylammonium (BTMA) ionomer for fuel cell performance test was prepared as follows: The pre-irradiated ETFE film was first immersed in argon-purged chloromethylstyrene solution (50% v/v in xylene) at 60 °C for 16h. The grafted films were

washed with toluene several times and dried under vacuum, and then immersed in trimethylamine (40 wt%) solution at room temperature for 24h to obtain quaternized BTMA in chloride form.

II-3. Characterization of AEMs

The completion of ion-exchange reactions was confirmed by monitoring iodide atoms of graft-type AEMs along the cross-sectional direction using a scanning electron microscopy (SEM, JEOL, JSM-5600) instrument equipped with an energy dispersive X-ray analyzer (EDX). Solid-state ^{13}C cross polarization/magic angle spinning (MAS) NMR experiments were performed using a Bruker AVANCE 300 spectrometer at the operating frequency of 75.5 MHz. The samples were packed as powders in a ZrO_2 rotor with a diameter of 4 mm. The MAS frequency was set to 10 kHz, and the sample temperature was 25°C. A total of 15−20K scans were collected in the spectral width of 23 kHz with a recycle delay of 5 s. All spectra were obtained at the cross polarization time of 2 ms through broadband proton decoupling. The spectra were externally referenced to glycine (176.0 ppm).

The GD of AEM was estimated from the weight change in grafted films by the following equation:

$$GD(\%) = \frac{W_g - W_0}{W_0} \times 100\% \qquad (1)$$

where w_0 and w_g are the weights of membranes before and after grafting in the dry state, respectively.

The IEC of AEM was determined using a standard back titration method. The membrane in the OH^- form was immersed in 15 mL of a 0.1-N HCl solution (V_{ref}, mL) for 24 h. Then, the solution was titrated with a standard NaOH (0.1 N) solution (V_{mem}, mL) to pH = 7.0 by an automatic titrator (HIRANUMA COM-555). Subsequently, the membranes were washed and immersed in deionized water for 24 h to remove residual HCl and then dried under vacuum at 50°C overnight and weighed to determine dry masses in the Cl^- form. The experimental IEC

(IEC_{exp}) value was calculated using the following equation:

$$IEC_{exp} = C \times (V_{ref} - V_{mem}) / W_{dry} \qquad (2)$$

where C is the concentration of the NaOH solution, and W_{dry} is the mass of dry AEMs.[17–21]

The WU of AEM was calculated by the weight measurements using the following equation:

$$WU(\%) = \frac{W_{wet} - W_{dry}}{W_{dry}} \times 100\% \qquad (3)$$

where W_{wet} represents the weight of AEM in the hydrated state. To measure WU, AEM was completely hydrated in water and lightly wiped with Kimwipes to remove excess water on the surface before weighing. The hydration number (λ_w) was calculated by WU and IEC_{exp} using the following equation:

$$\lambda_w = \frac{10WU}{M_w IEC_{exp}} \qquad (4)$$

where M_w (18 g/mol) is the molecular weight of water. Thus, the total water volume fraction (ϕ_w) of wet AEM can be calculated by equation (5).

$$\phi_w = \frac{\frac{WU/100(1+GD/100)}{d_w}}{\frac{1}{d_{ETFE}} + \frac{GD/100}{d_{graft}} + \frac{WU/100(1+GD/100)}{d_w}} \qquad (5)$$

where d_w and d_{graft} are the mass density of water and the graft chains, both of which are approximately 1.0 g/cm^3. Similarly, the volume fractions of ETFE ($\phi_{ETFE} = \frac{\frac{1}{d_{ETFE}}}{\frac{1}{d_{ETFE}} + \frac{GD/100}{d_{graft}} + \frac{WU/100(1+GD/100)}{d_w}}$) and grafts ($\phi_{graft} = \frac{\frac{GD/100}{d_{graft}}}{\frac{1}{d_{ETFE}} + \frac{GD/100}{d_{graft}} + \frac{WU/100(1+GD/100)}{d_w}}$) in the water-swollen state can be deduced as well.

The anion conductivity of AEM was measured in the plane direction at 100 kHz using four-point probe alternating current electrochemical impedance spectroscopy with an electrode system connected to an LCR meter (HIOKI 3522 LCR HiTESTER) at the desired temperature.[17] AEM was fully hydrated in nitrogen-saturated deionized water and placed between two platinum electrodes. The anion conductivity σ (mS/cm) was calculated from the

obtained resistance R (Ω) according to the following equation.

$$\sigma\ (mS/cm) = L / (S \times R) \times 10^3 \qquad (6)$$

where L (cm) is the distance between two electrodes, and S (cm^2) is the cross-sectional area of the membrane obtained by multiplying the membrane thickness by the membrane width.

The alkaline stability of AEM was examined by soaking the membrane in a 1-M KOH solution in a vial at 80°C for up to ~600 h and evaluated by measuring a change in the anion conductivity at 60°C. Before the conductivity measurement, the membrane was thoroughly washed with N_2-bubbled deionized water.

II-4. SANS measurement

SANS measurements were mainly performed on a KWS-2 SANS diffractometer operated by Juelich Center for Neutron Science at the neutron source Heinz Maier-Leibnitz (FRM II reactor) in Garching, Germany.[30] The incident neutron beam at KWS-2 was monochromatized with a velocity selector to have the average wavelength (λ) of 5 Å with a wavelength resolution of $\Delta\lambda/\lambda$ = 20%. The scattering patterns were collected with a two-dimensional scintillation detector and circularly averaged to obtain scattering intensity profiles as a function of q, where q is the scattering vector, which is defined by $q = (4\pi/\lambda)\sin(\theta/2)$. λ and θ are the neutron wavelength and scattering angles, respectively. Some SANS measurements were performed on an IBARAKI materials design diffractometer (iMATERIA) at the Japan Proton Accelerator Research Complex (J-PARC) under a user program (proposal No. 2017B0210) to confirm the scattering spectra at high-q range. To follow the membrane structure at the real experimental condition, AEMs were measured in a hydroxide form. To prevent degradation, excess hydroxide ions were completely removed by washing AEMs in degassed water under N_2 flow. The obtained scattering profiles were corrected for the instrument background, detector sensitivity, and scattering from empty cell, and finally calibrated to absolute scale (cm^{-1}) using a Plexiglas secondary standard. The incoherent scattering intensity of each sample was estimated by the flat part of the profile at high-q range and was subtracted from the absolute

scattering intensity profile. All SANS measurements were performed at 25 ± 0.5°C.

II-5. Membrane electrode assembly fabrication and fuel cell test

The membrane electrode assembly (MEA) was fabricated using the catalyzed gas diffusion electrode (GDE) method. AEM98 (1.71 mmol/g) and BTMA (2.74 mmol/g) in chloride form were frozen in liquid N_2 and ground into powder for 5 min using a freezer mill (JFC-300, Japan Analytical Industry) and used as ionomer. The catalyst and ionomer powder were mixed and grinded for 5 min with a mortar and pestle; then, 1 mL of deionized water was added, and grinding continued for 5 min to obtain a homogenous slurry. Then, 7 mL of 2-propanol was added with grinding. The ink was homogenized by ultrasonication (WT-100M) for 1 h at room temperature. The catalyst ink was sprayed on the gas diffusion layer (GDL, SIGRACET®, GDL35BC) and dried in air to prepare GDE. The ionomer ratio was adjusted to be 10 wt% on the basis of anode and cathode. For the anode side, Ni–C catalyst (64.5% Ni) was used, and the catalyst loading was adjusted to 2.5 ± 0.1 mg/cm^2. The cathode side was prepared using an NPC-2000 (Co–Fe) catalyst, and the catalyst loading was adjusted to 1.45 ± 0.1 mg/cm^2. The geometric surface areas of all GDEs were 5.0 cm^2. The GDEs and membranes were immersed in 1-M KOH overnight at room temperature, and excess KOH was gently wiped from the membranes and GDEs. Then, the membrane was sandwiched between two GDEs to fabricate MEA.

The fuel cell performance was investigated in a single cell with serpentine flow channels with 10-wt% hydrazine hydrate and a 1-M KOH aqueous solution as a fuel at 80°C. The flow rate of hydrazine hydrate fuel was adjusted to 20 mL/min. At the cathode side, the humidified oxygen gas flow rate and the back pressure were optimized to be 100 mL/min and 10 kPa, respectively, to obtain the maximum performance. Current–voltage curves were recorded using an electronic load. Durability was evaluated by the OCV-hold test with an oxygen flow rate of 100 mL/min without back pressure. Voltage loss was recorded under constant current density of 8.0 mA/cm^2 for 455 h.

III. Results and discussion

III-1 Preparation and characterization of AEMs

III-1.1 Preparation

As shown in Scheme 2, the radiation-induced graft polymerization of StIm into pre-irradiated ETFE films was conducted in the monomer solution of StIm in 1,4-dioxane at 60°C for 0.67–16 h to obtain StIm-grafted ETFE films with GDs in the range of 8–98%. The molecular structure of the graft polymers was confirmed by ^{13}C solid-state NMR spectrum as shown in Figure S1 in the supporting information. Generally, GD rapidly increases with time in the first 12 h, meaning that in this time span, the reaction time is a crucial factor to vary GD. The longer the reaction time is, the larger is GD. While after 12 h, an increase in GD with time slows down, and GD is up to ~98% at 16 h, close to the saturation value under the current radiation condition. The plot of GD as a function of reaction time is shown in Figure S2 in the Supporting Information.

The obtained StIm-grafted ETFE, the films were *N*-methylated with iodopropane in 1,4-dioxane to give AEMs in the iodide form. The N-alkylation reaction of StIm units of the grafts in homopolymer-grafted film proceeded quantitatively, evidenced by the weight change measurement.[18] Because the ion-exchange reaction of AEMs from iodide to hydroxide in grafted-type AEMs was slow, we conducted the ion-exchange reaction for the hydroxide form via the corresponding chloride form of AEMs (namely, $I^- \rightarrow Cl^- \rightarrow OH^-$). The completion of reactions was confirmed by the SEM-EDX spectrum, as previously reported.[18]

The representative IEC_{exp} values determined by the conventional titrimetric analysis shown in Table 1 were plotted as a function of GD in Figure S3 in the Supporting Information. These IEC_{exp} values are at 76–93% levels of the expected IEC (IEC_{cal}) calculated using the millimolar amount of a quaternary ammonium salt in the unit weight (1 g) of AEM. A similar phenomenon was also observed for AEMs containing imidazolium or anilinium hydroxide in graft polymers.[20, 31-33] In our latest report, we elucidated that this phenomenon was due to the

distribution of a part of graft polymers (which are non-conductive) in the non-conductive phase.[20] We also stated that the ratio of IEC_{exp} to IEC_{cal} (IEC_{exp}/IEC_{cal}) increases with GD and approximately characterizes the ratio of graft polymers in the conducting phase to the total graft polymers. Therefore, an increase in GD is an effective way to increase the fraction of "conductive" graft polymers over the total graft polymers made.[20]

III-1.2 Conductivity, WU, and hydration number

The characteristics of these AEMs are listed in Table 1. The initial OH^- conductivity (σ_{OH^-}) of AEMs with different GDs at 25°C was plotted as a function of IEC_{exp} in Figure 1(a). Similar to previous PEMs and AEMs, σ_{OH^-} increases with an increase in IEC_{exp} owing to the increased number density of ionic groups, and also with an increase in the temperature, *i.e.* 60°C as shown in Figure S4 in the Supporting Information, owing to the enhanced ion transfer at elevated temperature. By linear extrapolation of the data in Figure 1(a) toward zero, one can obtain a similar threshold value of 0.2 for $\sigma_{OH^-} = 0$, which represents the onset of anion transport. The existence of this threshold for the anion transport results from disconnected ion channels in AEMs with very low IECs.

The WU and λ_w of AEMs were plotted as a function of IEC_{exp} in Figures 1(b) and 1(c), respectively. Figure 1(b) shows a slow increase in WU at IEC_{exp} values lower than 0.54 mmol/g, and then a rapid increase in WU with an increase in IEC_{exp}. Figure 1(c) shows a discontinuous increase in λ_w with an increase in IEC_{exp}, namely, AEMs showed λ_w of approximately 10 at IEC_{exp} lower than 0.54 mmol/g, and those of 22–27 at IEC_{exp} higher than 0.9 mmol/g. The λ_w of AEM with IEC_{exp} of 0.8 mmol/g represents a value (~14) at the transition. This discontinuous change in λ_w may indicate the existence of a significant structural modification, which enables the membrane to adsorb more water. To explain these changes, we define characteristic IEC (IEC_c), which is the crossover of two linear relationships in Figure 1(b), to be approximately 0.7–0.8 mmol/g. Thus, the corresponding characteristic GD (GD_c) is in the range of 20–25%. We presume distinct changes in both the structure and properties before and after characteristic

IEC_c or GD_c, which will be discussed in detail in later sections.

In contrast to WU and λ_w, the IEC_{exp} dependence of conductivity seems more continuous, as shown in Figure 1(a). This suggests that the structural change predicted from the unusual jump of λ_w does not affect the anion-conducting behavior. A similar phenomenon was also reported by Amel *et al.*, in which they observed a steep increase in WU but not conductivity in quaternary ammonium poly(sulfone) based AEMs with IEC.[34]

Compared with the previously reported Im/St-AEMs with similar IEC,[17-21] these new AEMs show similar conductivities but much lower WU and λ_w. This occurs probably because the hydrophilic/hydrophobic phase separation is much stronger in the current AEMs because the homopolymer graft chains with more regularly arranged hydrophilic Im groups are perpendicularly connected to hydrophobic St units rather than those in Im/St-AEMs, which contain copolymer grafts with parallelly connected Im and St segments in a random manner. Thus the reinforced hydrophobic domains in the graft chains together with semi-crystalline domains in ETFE base films constrain the mechanical and dimensional change of AEMs against the water swelling. This effect is like the addition of cross-linkers to polyethylene-based AEMs, which increased the ion density so that the conductivity, but decreased the water swelling.[35] It is rational that a clear microphase separation between ionic groups and polymer backbone is an efficient way to create water/ion channels and reduce WU.

III-1.3 Long-term alkaline durability

The alkaline durability of these AEMs was evaluated by following the change in the membrane conductivity when AEMs were immersed in 1-M KOH at 80°C.[8-13] Figure 2 shows a change in the relative conductivities of AEMs with different GDs of 18, 30, 42, and 56%, designated as AEM18, AEM30, AEM42, and AEM56 at 60°C on the basis of their initial conductivities, respectively. AEM18 shows an excellent alkaline stability over 600 h, judging from its constant conductivity (50–60 mS/cm at 60°C) during the entire immersion period, although the surface of the membrane appears to be slightly rougher than its initial state.

AEM18 with moderate conductivity and high stability in an alkaline solution containing low WU is almost the best AEM up to now compared with the other AEMs reported in the literature.[8-21] However, all other three AEMs with IECs > IEC_c show poor durability in the alkaline solution. After 600 h, the relative conductivities of those AEMs decreased to less than 10% level of their initial values. The evaluation of membrane durability for all AEMs was marked in Table 1. The results show that similar to WU and λ_w, the long-term alkaline durability also exhibits a dramatic change across IEC_c.

III-2 Structural analysis of StIm-AEMs with different IECs in dry and water-swollen states

As mentioned above, the WU, λ_w, and alkaline durability of AEMs have transition points at IEC_c (0.7–0.8 mmol/g) or GD_c (20–25%), as shown in Figure 1. Because the unusual IEC_{exp} dependence of membrane properties cannot be explained by only chemical structures and their primary properties, the effect of higher-order structural transition may be profound in the membrane. Thus, to clarify whether the expected structural change occurs or not, three AEMs with GDs of 8, 11, and 14% and four AEMs with GDs of 30, 42, 56, and 86%, which have lower and higher IECs than IEC_c, were selected to perform SANS measurements.

Figures 3(a) and 3(b) show the SANS profiles of these AEMs in dry and fully water-swollen states at room temperature, respectively. For water-swollen AEMs, D_2O was used as a solvent to obtain higher scattering intensity and lower incoherent scattering background. To catch the structural features at high-q range, the incoherent scattering intensity was removed for all profiles. The original scattering profiles before the incoherent scattering correction for AEMs in dry and wet states are shown in Figures S5(a) and S5(b) in the Supporting Information, respectively. According to the scattering features, as discussed in our previous papers, we expediently separate these SANS profiles into two q-regions. Region I at $q < 1.3$ nm^{-1} is related to the microphase separation between conducting/non-conducting phases, and Region II at $q >$ 1.3 nm^{-1} is related to the local structures in the conducting phase.[20]

III-2.1 Dry AEMs

In Region I, a broad correlation peak at approximately 0.15–0.25 nm^{-1} was observed for all dry AEMs in Figure 3(a). These typical broad peaks with a *d*-spacing of approximately 30 nm were well characterized as the microphase separation between ETFE base material and graft polymers constrained by the alternation of crystalline phase and amorphous phase, as mentioned in our previous studies.[18-20] The peak intensity increased with IEC at 0 < IEC < 0.95 mmol/g, and then kept as a constant or even slightly decreased level when IEC further increased. A similar phenomenon has been reported before in ETFE-based poly(styrene sulfonic acid)-grafted PEM, which was attributed to the possible formation of extra PS graft polymer domains when IEC was high.[16] Similar to our previous reports, the peak position shifted to the low *q*-range with an increase in IEC especially at IEC < 0.95 mmol/g (GD < 42%), and the broadness of the peak increased, which suggests that the incorporation of more graft polymers in amorphous domains expanded the stacking distance and perturbed the ordering arrangement.[18–20] At IEC > 0.95, the low-*q* shift of the peak was not clear, which confirmed that graft polymerization in lamellar stacks nearly stopped, and the polymerization proceeded most likely outside of lamellar stacks.[18] All profiles of dry AEMs at $q > 0.2$ nm^{-1} obeyed Porod's law, *i.e.*, $I(q) \sim q^{-4}$,[36] which characterizes the distinct phase separation between graft polymers and ETFE base materials with a sharp boundary.

At the high-*q* range of $q > 1.3$ nm^{-1} (Region II), no specific structure feature of $I(q)$ profiles was observed regardless of IEC or GD, even though there were many reports showing ionomer peaks in this *q*-region. This occurred probably because no obvious ion channels were formed without water. Thus, dry AEMs with different IECs show similar local structures and distribution of graft chains.

III-2.2 AEMs equilibrated in D_2O

At the *q*-range of 0.15–0.25 nm^{-1} (Region I), by comparing Figures 3(a) and 3(b), it is determined that D_2O-equilibrated AEMs exhibited the correlation peak at lower *q* compared to

the corresponding dry AEMs because the incorporation of water with the graft polymers in the amorphous domains expanded the periodic lamellar *d*-spacing of crystalline and amorphous phases. Because the scattering profiles of all wet AEMs also showed similar Porod's behavior to those of dry AEMs in this region, it can be concluded that the incorporation of water does not deteriorate the sharp boundary between hydrated graft polymers and hydrophobic ETFE base materials.

At the high-q range (Region II), a water-swelling-induced peak, which was not observed in dry AEMs, newly appeared. Specifically, all D_2O-equilibrated AEMs showed a clear scattering maximum (i.e., ionomer peak), which indicated the formation of ionic clusters in the conducting phase.[37-43] The ion clustering effect has been regarded as an effective factor for the fast diffusion of water and conduction of ions through the membrane.[44-51] The ionomer peak of AEM08 seemed to be slightly broader than other AEMs and had the lowest intensity. The peak position, q_2, is ~3.0 nm^{-1}, which indicated that the mean distance between two ionic domains, d_2 ($=2\pi/q_2$), was approximately 2.1 nm. The peak became sharper with higher intensity when IEC increased, which suggested the formation of more distinct well-separated nanodomains. We summarized all d_2 of wet AEMs in Table 2 and plotted them as a function of IEC in Figure 3(c). This result shows that d_2 barely changes at IEC < IEC_c (or GD < GD_c), and then steadily increases at IEC > IEC_c. Thus, the IEC (or GD) dependence of d_2 should also relate to the structural change across IEC_c, similar to what we observed in the WU and durability measurements.

III-3 Characteristic hierarchical structures interpreted by contrast variation method

III-3.1 Conducting/non-conducting two-phase feature and the distribution of graft polymers in both phases

To reveal the structural difference in these AEMs, the contrast variation SANS measurements were performed for AEMs with lower IECs (*i.e.*, AEM14) or higher IECs (*i.e.*, AEM42 and AEM86) than IEC_c. The scattering profiles of these three AEMs equilibrated in

different H_2O/D_2O mixtures are shown in Figure S6 in the Supporting Information. As mentioned in Scheme 1, the structural analysis in Region I allowed us to clarify the microphase separation characteristics of the membranes. Our recently reported structural model of "conducting/non-conducting two-phase system" can be used to describe microphase separation and the distribution of graft polymers in each phase for graft-type AEMs with Im/St copolymer grafts onto ETFE.[20] The model was verified by ruling out other possible structural models in ref. 20. Here, we apply this model to analyze the structure of current membranes. We omit the detailed description of the model and only mention the two important facts. Specifically, (1) the non-conducting phase (phase 1) is made of ETFE base polymers and non-conductive graft polymers. The conducting phase (phase 2) is made of conductive graft polymers and water. Phases 1 and 2 are clearly separated. (2) The volume fractions of graft polymers distributed in conducting ($\phi_{\text{c-graft}}$) and non-conducting ($\phi_{\text{nc-graft}}$) phases can be evaluated in a quantitative manner by the contrast variation and contrast matching SANS method, as shown in Figures S6 and S7 in the Supporting Information.

As listed in Table 2, we estimated $\phi_{\text{nc-graft}}$ and $\phi_{\text{c-graft}}$ of each AEM (the calculation methods were described in the Supporting Information) for the distribution of graft polymers in either conducting or non-conducting phases. With an increase in IEC, $\phi_{\text{c-graft}}$ increased from 0.133 (AEM14) to 0.274 (AEM86), whereas $\phi_{\text{nc-graft}}$ was relatively constant with a value of approximately 0.03.

III-3.2 Nanophase separated structure in the conducting phase

In Region II (q > 1.3 nm^{-1}), all SANS profiles of water-swollen AEMs showed a clear ionomer peak, which is the typical structural feature of the conducting phase, as shown in Figures 3(b) and S6. Compared to previously reported Im/St-AEMs,[20] the ionomer peaks of current StIm-AEMs are much sharp, which indicates a more distinct nanophase separation in the conducting phase owing to the linear chemical arrangement of St and Im moieties. The contrast variation experiments for the representative membranes AEM14, AEM42, and AEM86

showed that the profiles around the ionomer peak were superimposed with one another by the vertical shifting of the curves [Figures S8(a)–S8(c)], which confirmed that the conducting phase can be treated as a two-component system, *i.e.*, it consists of hydrophilic (water) and hydrophobic (graft polymer) components.

The origin of the ionomer peak is attributed to the correlation of one of these two components. According to Babinet's principle,[36] it is not possible to distinguish which component corresponds to the correlation peak from a scattering curve alone. Namely, for AEMs, it is not clear from only Figure 3 whether the hydrophilic domains are dispersed in the hydrophobic matrix ("reverse-micelles") or the opposite ("micelles"), as illustrated in Figures 4(a) and 4(b), respectively. However, considering the volume fraction of scattering objects and the matrix, which generally correspond to minor and major components in a system, one can estimate that either a hydrophilic or a hydrophobic domain is a sphere (*i.e.*, the exact component for the origin of the ionomer peak). In the following sections, we apply the hard-sphere liquid model and Porod limit analysis to assign the origin of the ionomer peak.

Hard-sphere liquid model analysis

First, we employ the hard-sphere (HS) liquid model developed by Kinning and Thomas using the Percus–Yevick correlation function, which describes the structure of ionic conducting materials.[20, 36, 52-58] In this model, scattering objects are assumed to be spherical particles with an average radius (R_S) randomly distributed in the conducting phase. The particles are considered to be liquid-like with isotropic spatial distribution, and the average distance between the nearest-neighbor pair (r_0) is larger than $2R_s$. In this study, d_2, which is determined from the ionomer peak maximum, is used as r_0. Thus, the observed scattering intensity, $I(q)$, is expressed as a function of the volume fraction of spheres in the conducting phase (V_S) and R_S.[20, 54-56] The details of how to apply this model to grafted AEMs for the determination of R_S and V_S can be found in ref. 20. The ionomer peaks in the scattering profiles in Figure 3(b) were fitted well by the HS-liquid model, as highlighted in Figure 5. The values of R_S and V_S, obtained by the best-

fitting curves for the scattering data, are listed in Table 3. The R_S values of AEMs increased from 10.2 Å to 12.6 Å with an increase in IEC from 0.24 to 1.72 mmol/g. V_S seemed to be a more constant value as a function of IECs with a slight increase from 0.33 to 0.41 in the low IEC range.

The component in the sphere can be specified as water or graft polymers by comparing their volume fractions in the conducting phase with V_S. Specifically, we first estimate the volume fractions of water (V_w) and graft polymers ($V_{graft} = 1-V_w$) and then check whether V_w or V_{graft} matches the value of V_S. V_w can be independently estimated from $\phi c-graft$, which is determined from contrast variation experiments (Method-1) or from λ_w, which is determined from the WU measurements (Method-2) using the following equations:

Method-1) $$V_{w1} = \frac{\phi w}{\phi w + \phi c-graft} \quad (7)$$

Method-2) $$V_{w2} = \frac{18\lambda_w}{18\lambda_w + M_{seg}} \quad (8)$$

where M_{seg} = 255 (g/mol) is the molecular weight of one repeating unit with an ionic imidazolium head on the graft polymer chain. As listed in Table 2, the V_{w1} values are almost the same as the values of V_{w2}, which confirms not only the correctness of V_w, but also validity of the quantitative analysis in the conducting/non-conducting microphase separation structure model using the contrast variation method in Section-III.3.1. The average value of V_{w1} and V_{w2} was defined as V_w for AEM14, AEM42, and AEM86, while the V_{w2} value was utilized as V_w for other AEMs, as listed in Table 3.

Similar to the IEC dependence of WU and λ_w shown in Figure 1, V_w exhibited minor (0.43–0.45) and major (0.61–0.65) components for StIm-AEMs with lower and higher IECs than IEC_c, respectively. The comparison of V_S with V_w or V_{graft} in Table 3 was plotted in Figure 7(a) as a function of GD. It shows that V_S is close to V_w for AEMs with low IEC < IEC_c and to V_{graft} for AEMs with high IEC > IEC_c. This result indicates that the structure of the conducting phase in these AEMs varies from “reverse-micelles” (water puddles dispersed in the polymer

matrix) to "micelles" (graft polymer aggregates dispersed in water) across the critical point of IEC (IEC_c). Note that V_S of AEM08 is slightly smaller than V_w probably because the spherical water domains in AEM08 are not well-developed and less connected due to the small number density of cation groups in the membrane. Instead, AEM30 with the IEC, close to transition value (IEC_c) showed larger V_w (~0.5) than the corresponding V_S, probably resulting from the mixed structures of "micelles" and "reverse-micelles" in the membrane.

Porod limit analysis

To confirm the component of the spheres in the conducting phase of AEMs and its GD dependence obtained above by the hard sphere liquid model in the last section, we apply the Porod limit analysis to estimate the component of the spheres and the averaged radius of spheres, defined as R_{Porod}, to distinguish it from R_S obtained by the hard sphere liquid model.[36, 58]

Because ideal two-component systems (e.g., charged colloidal system and an ionic membrane/solution) discussed in this study possess a clear interfacial boundary, $I(q)$ should decrease as $\sim q^{-4}$ for large q (so-called Porod law) with the proportionality constant, which is related to the total area of the graft polymer/water interface (A) in the scattering volume (V).[36, 58] Thus, as $q \to \infty$,

$$\lim_{q\to\infty} I(q) \to 2\pi\Delta b^2 \Sigma / q^4 \qquad (9)$$

where $\Sigma = A/V$, and Δb is the scattering length density difference between graft polymers and water (D_2O), which is $\sim 5.27 \times 10^{10}$ cm^{-2} in this study. In Figure 6, we plot Iq^4 versus q for all AEMs. All profiles exhibit a constant behavior at high-q range, which indicates the sharp polymer/water interface. Thus, Σ of each AEM was extracted using eq. (9) and is listed in Table 4.

Owing to the energetic requirement of the spherical shape to minimize the interfacial free energy, the spherical structures of "reverse-micelle" or "micelle" models are widely accepted as typical microscopic structures for polymers consisting of hydrophilic/hydrophobic units, as

illustrated in Figures 4(a) and 4(b), respectively. The size and component of spherical domains are related to Σ, as will be discussed in detail below. The mixed structures may exist in AEM30; thus, this analysis is not applied to the AEM30 membrane.

For the "reverse-micelles" model, the spherical domains are composed of water, as illustrated in Figure 4(a). Thus, the Porod radius of water spheres, $R_{\mathrm{Porod,w}}$, can be estimated from the interface quantity of Σ on the basis of the following equation[59–61]

$$R_{Porod,w} = \frac{3\phi_w}{\Sigma} \qquad (10)$$

$R_{\mathrm{Porod,w}}$ values for all AEMs are listed in Table 4. The $R_{\mathrm{Porod,w}}$ values of AEMs with low IECs < $\mathrm{IEC_c}$ are nearly constant at approximately 11.8 Å, which is comparable to R_{S} (approximately 10.5 Å) obtained from the HS-liquid model. Whereas, those of AEMs with high IECs > $\mathrm{IEC_c}$ are estimated to be 23.8–26.3 Å, which is much larger than the corresponding R_{S}, as shown in Figure 7(b). The values for AEMs with high IECs exceed the upper limit of the mean distance between two spheres (*i.e.*, d_2), which indicates that the "reverse-micelles" model does not match the case of AEMs with high IECs.

For the "micelles" model, the spherical domains are made of graft polymers, as illustrated in Figure 4(b). The Porod radius of graft polymer spheres, $R_{\mathrm{Porod,g}}$, can be estimated by the following equation:

$$R_{Porod,g} = \frac{3\phi_{c-graft}}{\Sigma} \qquad (11)$$

As listed in Table 4 and plotted in Figure 7(b), the resultant $R_{\mathrm{Porod,g}}$ values of AEMs with high IECs > $\mathrm{IEC_c}$ are in the range of 14.2–14.8 Å, which is comparable to R_{S} values and confirms the validity of the "micelles" model. Both $R_{\mathrm{Porod,w}}$ and $R_{\mathrm{Porod,g}}$ are larger than $d_2/2$, which means that spherical domains should be connected to one another and, thus, well-percolated. On the basis of the abovementioned comparison between R_{S} and R_{Porod} for all AEMs with various IECs, it is concluded that StIm-AEMs possess "reverse-micelles" and "micelles" model structures in low and high IEC ranges in the conducting phases, as schematically illustrated in Figures 8(a)

and 8(b), respectively.

Local structures around imidazolium ionic groups

Another important parameter possibly obtained from the Porod limit analysis is the interfacial area occupied per ionic head (*S*).[59-61] We assume that all ionic imidazolium groups with the total number of N_{ion} existing in the scattering volume of V are located at the graft polymer/water interface with an occupied area of *S*. Thus, the *S* value can be calculated using the following equation:

$$S = \frac{\Sigma}{N_{ion}/V} = \frac{v_0 \Sigma}{\phi c - graft} \qquad (12)$$

where v_0 is the volume of graft polymer associated with one ionic group, which can be calculated from the equivalent weight of the repeating unit and its mass density of approximately 424 Å^3, and $\phi_{c\text{-graft}}$ is the effective volume fraction of graft polymer in the conducting phase, as we quantitatively determined in the abovementioned section.

The resultant *S* values are shown in Table 4 and Figure 7(c). The obtained value shows that *S* is approximately constant (80–93 Å^2), regardless of IEC and WU. The *S* values of these StIm-AEMs are relatively larger than those obtained for long-pendant side chain PFSI (55–61 Å^2)[59, 60] or short-pendant side chain PFSI (70–74 Å^2)[61] partially because of the larger size of imidazolium cationic group compared to the sulfonic acid group in those systems, and partially because of the weaker interaction between the ion-pair of imidazolium cation and OH^- than that of sulfonic acid and H_3O^+, which has been confirmed by molecular dynamics simulation studies.[62]

It is possible to estimate the average number of ionic groups per spherical domain, n_{ion}, using the following equation:

$$n_{ion} = \frac{4\pi {R_{Porod}}^2}{S} \qquad (13)$$

Thus, the obtained n_{ion} values are shown in Table 4 and Figure 7(c). For AEMs with IECs < IEC_c, n_{ion} is approximately 19–22. For AEMs with IECs > IEC_c, n_{ion} increases to 28–32.

Because *S* is almost conserved, the larger value of n_{ion} is attributed to the larger particle size of micelles relative to reverse-micelles.

The structure inversion from "reverse-micelles" to "micelles" increases the total WU and λ_w and also lowers membrane stability in alkaline solutions. Because the ionic imidazolium groups in "reverse-micelles" and "micelles" face the inner and outer interface direction of spherical domains, the former one is surrounded by fewer free spaces in the water domain than the latter one, which leads to smaller λ_w, as schematically shown in Figures 8(c) and 8(d). In other words, even though the area of interface occupied by one ionic group (*S*) is conserved, with an increase in IEC, a higher reaction rate of hydrolysis around the ionic groups is expected owing to the increased number of water molecules around the ionic groups, which considerably decreases stability in alkaline solutions. Even though the structure evolution in these StIm-AEMs is similar to those of perfluorosulfonated ionomer membranes (*i.e.*, Nafion® and its derivatives), the chemical composition and size of hydrophobic domains in these StIm-AEMs are unique.[59-61]

III-3. Hydrazine hydrate fuel cell performance and durability

The fuel cell performance is strongly dependent on the property of AEMs, such as water permeability and fuel barrier property in addition to interaction with catalyst layers. We fabricated four MEAs using StIm-AEMs, with IECs of 0.54 mmol/g (AEM18), 0.78 mmol/g (AEM30) 0.95 mmol/g (AEM42), and 1.71 mmol/g (AEM98), and the most frequently-used organic cations BTMA powder as an ionomer with Ni–C (2.5 mg/cm^2) and NPC-2000 (1.6 mg/cm^2) as an anode and cathode, respectively. The single hydrazine hydrate fuel cell performance was shown in Figure S9. MEA with AEM42 showed the best performance and achieved the maximum power density of 38 mW/cm^2 at the current density of 90 mA/cm^2, at the optimal flow rate of 50 mL/min with a back pressure of 10 KPa at the cathode side. Contrary to AEM42, MEA with AEM18 and AEM30 presented nearly no performance, and with AEM98 achieved lower performance of 25 mW/cm^2 at the current density of 60 mA/cm^2.

According to the ex situ membrane durability test results in an alkaline solution shown in Figure 2 and the abovementioned structure analysis, AEM18 is regarded as the most suitable membrane with both good conductivity and alkaline durability owing to its reverse-micelle structure. However, MEA fabricated with AEM18 showed such poor fuel cell performance, although the ex situ membrane properties were good. This result indicates that the real fuel cell operation condition should be deviated from the ex situ alkaline solution. The structural analysis of the membranes required for the durability in the real fuel cells is not sufficient. However, so far, the membrane structures in the fuel cell cannot be analyzed clearly. Thus, we believe it is one of the promising methods to estimate them in fuel cell operating condition from the evidence of the membrane structures in ex situ solutions, which are clearly analyzed. It is known that the membrane under the fuel cell operation condition is relatively dry compared to that in an alkaline solution. The lower hydration increases the hydrophobicity of the membrane surface, which decreases surface adhesion to ionomers and catalyst layers and disconnects the network structure of ionic channels in the membrane. Consequently, the in situ conducting properties of AEM18 and even AEM30, are worse than those of the fully hydrated condition in the ex situ solution test, which leads to the poor fuel cell performance. In addition, the lower hydration effect in MEA possibly shifts the structure transition point of IEC_c toward higher IEC values; Thus, AEMs with relatively higher IEC, *i.e.*, AEM42, assembled in MEA may possibly keep the stable reverse-micelle structure, which is essential for the long-term in situ durability requirement.

It should be addressed that MEA fabricated with AEM98 showed worse fuel cell performance than AEM42 probably owing to the fact that AEM98 with a micelle structure is structurally too weak to exhibit good performance in either ex situ alkaline solutions or under severe hydrazine/KOH alkaline fuel cell conditions.

In order to improve the fuel cell performance, anion-conducting ionomers typically need to have a chemical structure that is similar to that of AEMs as well as higher anion conductivity

compared to that of AEMs to achieve good adhesion and connectivity of ion-paths at the molecular level. Therefore, we re-assemble MEA using AEM42 as membrane and fine-powdered AEM98 in chloride form as anion-conducting ionomer, which was prepared by pulverization using a freezer mill according to the literature.[63] The much improved fuel cell performance was achieved with the maximum power density of 80 mW/cm^2 at the current density of 140 mA/cm^2 as shown in Figure 9(a). It also exhibited a high OCV of 0.86 V, which indicated low fuel and gas permeability. The oxygen flow rate showed a considerable effect on the cell performance in which the performance was improved at the optimal flow rate of 100 mL/min with a back pressure of 10 KPa at the cathode side.

Since MEA fabricated with AEM42 exhibits the best fuel cell performance, the further durability test was performed at the constant current density of 8.0 mA/cm^2 at 80°C. As shown in Figure 9(b), this single cell exhibited excellent durability up to 455 h and maintained 64.7% (0.68 V) of the initial voltage. To our knowledge, this is one of the most durable alkaline-type fuel cells.[64–66] These results showed that Im/St-AEMs and their ionomer powders are promising materials for alkaline fuel cell applications in terms of performance and long-term durability. This result also confirms our previous presumption that AEMs under the in situ durability test condition are less hydrated than those in the ex situ (solution) test; thus AEMs with higher IEC, *i.e.* AEM42, still possess stable reverse-micelle structure and maintain long-term durability. It is essential and complicated to understand the membrane performance and in situ durability under the fuel cell conditions.[67] Therefore, the ex situ examinations of conducting properties, durability, and membrane morphologies are important to offer a mechanistic insight in the membrane properties–morphology relationships.

IV. Conclusions

In this study, we prepared new graft-type AEMs, composed of poly(2-(4-styryl)-N,N-dipropylimidazolium hydroxide) homopolymer graft chains containing different IECs, on ETFE films via the radiation-induced grafting technique. We investigated the effects of IEC on

electrochemical properties and durability in alkaline solutions. A critical IEC value, IEC_c (0.7–0.8 mmol/g) was observed. Below IEC_c, the membranes show low WU and very good alkaline stability in a 1 KOH solution at 80°C. Above this value, the membranes adsorb more water and are susceptible to hydrolysis.

This phenomenon was interpreted by structure evolution using the SANS technique with the contrast variation method. We proposed that at IECs < IEC_c, the structure of conducting phase in AEMs was characterized by the traditional "reverse-micelles" model. While at IEC > IEC_c, the structure changed to the network structure of "micelles". The further analysis using the hard-sphere liquid model and Porod limit analysis revealed that this structure inversion was dominated by the polymer/water interfacial energy, which imposed the conservation of interface area per ionic group. Thus, AEMs with the "reverse-micelles" structure were more alkaline-durable owing to the lower number of water molecules around one ionic group, which resulted in a slower hydrolysis reaction rate. The results in this study indicated that the molecular design in this type of AEMs to prevent ionic structure inversion from "reverse-micelles" to "micelles" is crucial to suppress WU and the susceptibility of the hydrolysis reaction. An increase in the hydrophobicity of the graft polymer backbone and the introduction of larger chemical hindrance around ionic groups might be a practical way to keep the "reverse-micelles" structure and improve the membrane stability in alkaline solutions.

MEA fabricated with AEM18 showed very poor fuel cell performance, although the ex situ membrane properties were good. However, AEM42 with the IEC of 0.95 mmol/g, with the maximum power density of 80 mW/cm^2 in the hydrazine hydrate fuel cell test, exhibited long-term durability under constant current (8.0 mA) up to 455 h, which thus far showed the best durability at 80°C compared to other platinum-free alkaline-type liquid fuel cells. In the typical platinum-free hydrazine hydrate fuel cell test, the membrane hydration level in MEA was less than that in an alkaline solution. Accordingly, IEC_c most likely shifted to higher IEC values, *i.e.*, > 0.95 mmol/g.

Notes

The authors declare no competing financial interest.

Acknowledgments

This work was partially supported by Grant-in-Aid for Scientific Research (A) from Japan Society for the Promotion of Science (JSPS) (KAKENHI Grant Number: 18H03850) and partially supported by “Advanced functional polymer materials alliance” project under QST innovation hub program in collaboration with participant companies.

References.

1. Steele, B. C. H.; Heinzel, A. Materials for fuel-cell technologies, *Nature* **2001**, *414*, 345-352.
2. Vielstich, W.; Lamm, A.; Gasteiger, H. *Handbook of Fuel Cells: Fundamentals, Technology, Applications*; John Wiley: 2004.
3. Peighambardoust, S. J.; Rowshanzamir, S.; Amjadi, M. Review of the proton exchange membranes for fuel cell applications, *Int. J. Hydrogen Energy* **2010**, *35*, 9349-9384.
4. Gasteiger, H. A.; Panels, J. E.; Yan, S. G. Dependence of PEM fuel cell performance on catalyst loading, *J. Power Sources* **2004**, *127*, 162-171.
5. Jacobson, M. Z.; Colella, W. G.; Golden, D. M. Cleaning the air and improving health with hydrogen fuel-cell vehicles, *Science* **2005**, *308*, 1901-1905.
6. Wee, J. H. Applications of proton exchange membrane fuel cell systems, *Renewable & Sustainable Energy Reviews* **2007**, *11*, 1720-1738.
7. Wang, Y.; Chen, K.; Mishler, J.; Cho, S. C.; Adroher, X. C. A review of polymer electrolyte membrane fuel cells: Technology, applications, and needs on fundamental research, *Appl. Energy* **2011**, *88*, 981-1007.
8. Varcoe, J. R.; Slade, R. C. T. Prospects for alkaline anion-exchange membranes in low temperature fuel cells, *Fuel Cells* **2005**, *5*, 187-200.
9. Si, Z; Qiu, L.; Dong, H.; Gu, F.; Li, Y.; Yan, F Effects of Substituents and Substitution Positions on Alkaline Stability of Imidazolium Cations and Their Corresponding Anion-Exchange Membranes, *ACS Appl. Mater. Interfaces* **2014**, *6*, 4346-4355.
10. Varcoe, J. R.; Atanassov, P.; Dekel, D. R.; Herring, A. M.; Hickner, M. A.; Kohl, P. A.; Kucernak, A. R.; Mustain, W. E.; Nijmeijer, K.; Scott, K.; Xu, T.; Zhuang, L. Anion-exchange membranes in electrochemical energy systems, *Energy Environ. Sci.* **2014**, *7*, 3135-3191.
11. Couture, G.; Alaaeddine, A.; Boschet, F.; Ameduri, B. Polymeric materials as anion-

exchange membranes for alkaline fuel cells, *Prog. Polym. Sci.* **2011**, *36*, 1521-1557.

12. Merle, G.; Wessling, M.; Nijmeijer, K. Anion exchange membranes for alkaline fuel cells: A review, *J. Membr. Sci.* **2011**, *377*, 1-35.
13. Wang, Y. J.; Qiao, J.; Baker, R.; Zhang, J. Alkaline polymer electrolyte membranes for fuel cell applications, *Chem. Soc. Rev.* **2013**, *42*, 5768-5787.
14. Balog, S.; Gasser, U.; Mortensen, K.; Gubler, L.; Scherer, G. G.; Ben youcef, H. Correlation between morphology, water uptake, and proton conductivity in radiation-grafted proton-exchange membranes, *Macromol. Chem. Phys.* **2010**, *211*, 635-643.
15. Iwase, H.; Sawada, S.; Yamaki, T.; Koizumi, S.; Ohnuma, M.; Maekawa, Y. Hierarchical structure analysis of graft-type polymer electrolyte membranes consisting of cross-linked polytetrafluoroethylene by small-angle scattering in a wide-Q range, *Macromolecules* **2012**, *45*, 9121-9127.
16. Tap, T. D.; Sawada, S.; Hasegawa, K.; Yoshimura, Y.; Oba, M.; Ohnuma, M.; Katsumura, Y.; Maekawa, Y. Hierarchical structure-property relationships in graft-type fluorinated polymer electrolyte membranes using small- and ultrasmall-angle X-ray scattering analysis, *Macromolecules* **2014**, *47*, 2373-2383.
17. Yoshimura, K.; Koshikawa, H.; Yamaki, T.; Shishitani, H.; Yamamoto, K.; Yamaguchi, S.; Tanaka, H.; Maekawa, Y. Imidazolium cation based anion-conducting electrolyte membranes prepared by radiation induced grafting for direct hydrazine hydrate fuel cells, *J. Electrochem. Soc.* **2014**, *161*, F889-F893.
18. Zhao, Y.; Yoshimura, K.; Shishitani, H.; Yamaguchi, S.; Tanaka, H.; Koizumi, S.; Szekely, N.; Radulescu, A.; Richter, D.; Maekawa, Y. Imidazolium-based anion exchange membranes for alkaline anion fuel cells: elucidation of the morphology and the interplay between the morphology and properties, *Soft Matter* **2016**, *12*, 1567-1578.
19. Yoshimura, K.; Zhao, Y.; Hasegawa, S.; Hiroki, A.; Kishiyama, Y.; Shishitani, H.;

Yamaguchi, S.; Tanaka, H.; Koizumi, S.; Appavou, M.-S.; Radulescu, A.; Richter, D.; Maekawa, Y. Imidazolium-based anion exchange membranes for alkaline anion fuel cells: (2) elucidation of the ionic structure and its impact on conducting properties, *Soft Matter* **2017**, *13*, 8463-8473.

20. Yoshimura, K.; Zhao, Y.; Hiroki, A.; Kishiyama, Y.; Shishitani, H.; Yamaguchi, S.; Tanaka, H.; Koizumi, S.; Houston, J.; Appavou, M.-S.; Radulescu, A.; Richter, D.; Maekawa, Y. Reverse relationships of water uptake and alkaline durability with hydrophilicity of imidazolium-based grafted anion-exchange membranes, *Soft Matter* **2018**, *14*, 9118-9131.
21. Zhao, Y.; Yoshimura, K.; Takamatsu, H.; Hiroki, A.; Kishiyama, Y.; Shishitani, H.; Yamaguchi, S.; Tanaka, H.; Koizumi, S.; Radulescu, A.; Appavou, M.-S.; Maekawa, Y. Imidazolium-based anion exchange membranes for alkaline anion fuel cells: interplay between the morphology and anion transport behavior, *J. Electrochem. Soc.* **2019**, *166 (8)*, F472-F478.
22. Li, N.; Yan, T.; Li, Z.; Thurn-Albrecht, T.; Binder, W. H. Comb-shaped polymers to enhance hydroxide transport in anion exchange membranes, *Energy Environ. Sci.* **2012**, *5*, 7888-7892.
23. Li, N.; Zhang, Q.; Wang, C.; Lee, Y. M.; Guiver, M. D. Phenyltrimethylammonium functionalized polysulfone anion exchange membranes, *Macromolecules* **2012**, *45*, 2411-2419.
24. Zhang, F.; Zhang, H.; Qu, C. Imidazolium functionalized polysulfone anion exchange membrane for fuel cell application, *J. Mater. Chem.* **2011**, *21*, 12744-12752.
25. Zhang, H.; Shen, P. Recent development of polymer electrolyte membranes for fuel cells, *Chem. Rev.* **2012**, *112*, 2780-2832.
26. Mortensen, K.; Gasser, U.; Guersel, S. A.; Scherer, G. G. Structural characterization of radiation-grafted block copolymer films, using SANS technique, *J. Polym Sci. Polym. Phys. Ed.* **2008**, *46*, 1660-1668.
27. Nasef, M. M.; Hegazy, E. A. Preparation and applications of ion exchange membranes by

radiation-induced graft copolymerization of polar monomers onto non-polar films, *Prog. Polym. Sci.* **2004**, *29*, 499-561.

28. Song, J. M.; Ko, B. S.; Sohn, J. Y.; Nho, Y. C.; Shin, J. A study on the morphology of polystyrene-grafted poly(ethylene-*alt*-tetrafluoroethylene) (ETFE) films prepared using a simultaneous radiation grafting method, *Rad. Phys. Chem.* **2014**, *97*, 374-380.
29. Okumura, N.; Ikeda, Y. *Japan Patent* **2015**, 2015-129100.
30. Radulescu, A.; Pipich, V.; Frielinghaus, H.; Appavou, M. S. KWS-2, the high intensity / wide Q -range smallangle neutron diffractometer for soft-matter and biology at FRM II, *Journal of Physics: Conference Series* **2012**, *351*, 012026.
31. Maekawa, Y.; Yoshimura, K.; Takeuchi, K.; Hiroki, A.; Watanabe, S.; Hagiwara, T.; Shishitani, H.; Yamaguchi, S.; Tanaka, H. Alkaline durable anion-conducting electrolyte membranes prepared by radiation induced grafting of 2-methyl-4-vinylimidazole for non-platinum direct hydrazine hydrate fuel cells, *ECS Trans.* **2017**, *80*, 979-987.
32. Wang, L.Q.; Brink, J. J.; Liu, Y.; Herring, A. M.; Ponce-Gonzalez, J.; Whelligan, D. K.; Varcoe, J. R. Non-fluorinated pre-irradiation-grafted (peroxidated) LDPE-based anion-exchange membranes with high performance and stability, *Energy Environ. Sci.* **2017**, *10*, 2154-2167.
33. Ponce-Gonzalez, J.; Whelligan, D. K.; Wang, L.Q.; Bance-Soualhi, R.; Wang, Y.; Peng, Y.Q.; Peng, H.Q.; Apperley, D. C.; Sarode, H. N.; Pandey, T. P.; Divekar, A. G.; Seifert, S.; Herring, A. M.; Zhuang, L.; Varcoe, J. R. High performance aliphatic-heterocyclic benzyl-quaternary ammonium radiation-grafted anion-exchange membranes, *Energy Environ. Sci.* **2016**, *9*, 3724-3735.
34. Amel, A.; Gavish, N.; Zhu, L.; Dekel, D. R.; Hickner, M. A.; Ein-Eli, Y. Bicarbonate and chloride anion transport in anion exchange membranes, *J. Membr. Sci.* **2016**, *514*, 125-134.
35. Zhang, M.; Kim, H. K.; Chalkova, E.; Mark, F.; Lvov, S. N.; Chung, T. C. M. New polyethylene based anion exchange membranes (PE-AEMs) with high ionic conductivity,

Macromolecules **2011**, *44*, 5937-5946.

36. See for example, Roe, R. J. *Methods of X-ray and neutron scattering in polymer science*; Oxford Uni. Press: New York, 2000.
37. Wang, W. Q.; Liu, W. J.; Tudryn, G. J.; Colby, R. H.; Winey, K. I. Multi-length scale morphology of poly(ethylene oxide)-based sulfonate ionomers with alkali cations at room temperature, *Macromolecules* **2010**, *43*, 4223-4229.
38. Hsu, W. Y.; Gierke, T. D. Ion-transport and clustering in Nafion perfluorinated membranes, *J. Membr. Sci.* **1983**, *13*, 307-326.
39. Kim, S. Y.; Park, M. J.; Balsara, N. P.; Jackson, A. Confinement effects on watery domains in hydrated block copolymer electrolyte membranes, *Macromolecules* **2010**, *43*, 8128-8135.
40. Kusoglu, A.; Modestino, M. A.; Hexemer, A.; Segalman, R. A.; Weber, A. Z. Subsecond morphological changes in Nafion during water uptake detected by small-angle X-ray scattering, *ACS Macro Lett.* **2012**, *1*, 33-36.
41. Seitz, M. E.; Chan, C. D.; Opper, K. L.; Baughman, T. W.; Wagener, K. B.; Winey, K. I. Nanoscale morphology in precisely sequenced poly(ethylene-*co*-acrylic acid) zinc ionomers, *J. Am. Chem. Soc.* **2010**, *132*, 8165-8174.
42. Yarusso, D. J.; Cooper, S. L. Microstructure of ionomers: interpretation of small-angle x-ray scattering data, *Macromolecules* **1983**, *16*, 1871-1880.
43. Ertem, S. P.; Tsai, T. H.; Donahue, M. M.; Zhang, W.; Sarode, H.; Liu, Y.; Seifert, S.; Herring, A. M.; Coughlin, E. B. Photo-Cross-Linked Anion Exchange Membranes with Improved Water Management and Conductivity, *Macromolecules* **2016**, *49*, 153-161.
44. Elabd, Y. A.; Hickner, M. A. Block copolymers for fuel cells, *Macromolecules* **2011**, *44*, 1-11.
45. Li, N.; Wang, C.; Lee, S. Y.; Park, C. H.; Lee, Y. M.; Guiver, M. D. Enhancement of proton transport by nanochannels in comb-shaped copoly(arylene ether sulfone)s, *Angew. Chem.* **2011**, *123*, 9324-9327.

46. Chen, D.Y.; Hickner, M. A. Ion clustering in quaternary ammonium functionalized benzylmethyl containing poly(arylene ether ketone)s, *Macromolecules* **2013**, *46*, 9270-9278.

47. Liu, L.; Ahlfield, J.; Tricker, A.; Chu, D.; Kohl, P. A. Anion conducting multiblock copolymer membranes with partial fluorination and long head-group tethers, *J. Mater. Chem. A* **2016**, *4*, 16233-16244.

48. Pan, J.; Chen, C.; Li, Y.; Wang, L.; Tan, L.; Li, G.; Tang, X.; Xiao, L.; Lu, J.; Zhuang, L. Constructing ionic highway in alkaline polymer electrolytes, *Energy Environ. Sci.* **2014**, *7*, 354-360.

49. Dang, H. S.; Weiber, E. A.; Jannasch, P. Poly(phenylene oxide) functionalized with quaternary ammonium groups *via* flexible alkyl spacers for high-performance anion exchange membranes, *J. Mater. Chem. A* **2015**, *3*, 5280-5284.

50. Dang, H. S.; Jannasch, P. Exploring different cationic alkyl side chain designs for enhanced alkaline stability and hydroxide ion conductivity of anion-exchange membrane, *Macromolecules* **2015**, *48*, 5742-5751.

51. Dang, H. S.; Jannasch, P. Alkali-stable and highly anion conducting poly(phenylene oxide)s carrying quaternary piperidinium cations, *J. Mater. Chem. A* **2016**, *4*, 11924-11938.

52. Kinning, D. J.; Thomas, E. L. Hard-sphere interactions between spherical domains in diblock copolymers, *Macromolecules* **1984**, *17*, 1712-1718.

53. Percus, J. K.; Yevich, G. J. Analysis of classical statistical mechanics by means of collective coordinates, *Phys. Rev.* **1958**, *110*, 1-13.

54. Kaler, E. W.; Bennett, K. E.; Davis, H. T.; Scriven, L. E. Toward understanding microemulsion microstructure: A small-angle x-ray scattering study, *J. Chem. Phys.* **1983**, *79*, 5673-5684.

55. Seguchi, T.; Tamura, N. Mechanism of decay of alkyl radicals in irradiated polyethylene on exposure to air as studied by electron spin resonance, *J. Phys. Chem.* **1973**, *77*, 40-44.

56. Seguchi, T.; Tamura, N. Electron spin resonance studies on radiation graft copolymerization in polyethylene. II. Grafting initiated by allyl radicals trapped in irradiated polyethylene, *J. Polym. Sci. Polym. Chem. Ed.* **1974**, *12*, 1953-1964.

57. Smit, I.; Bezjak, A. Structural changes in the grafted copolymer polyethylene-styrene, *Polymer* **1981**, *22*, 590-596.

58. Porod, G. X-ray low angle scattering of dense colloid systems. Part I., *Kolloid Zeit* **1951**, *124*, 83-114.

59. Gebel, G.; Moore, R. B. Small-angle scattering study of short pendant chain perfuorosulfonated ionomer membranes, *Macromolecules* **2000**, *33*, 4850-4855.

60. Gebel, G. Structural evolution of water swollen perfluorosulfonated ionomers from dry membrane to solution, *Polymer* **2000**, *41*, 5829-5838.

61. Loppinet, B; Gebel, G. Rodlike colloidal structure of short pendant chain perfluorinated ionomer solutions, *Langmuir* **1998**, *14*, 1977-1983.

62. Han, K. W.; Ko, K. H.; Abu-Hakmeh, K.; Bae, C.; Sohn, Y. J.; Jang, S. S. Molecular dynamics simulation study of a polysulfone-based anion exchange membrane in comparison with the proton exchange membrane, *J. Phys. Chem. C* **2014**, *118*, 12577-12587.

63. Omasta, T. J.;, Park, A. M.; LaManna,J. M.; Zhang,Y.; Peng, X.; Wang, L.; Jacobson, D. L.; Varcoe, J. R.; Hussey, D. S.; Pivovar, B. S. ; Mustain,W. E. *Energy Environ. Sci*, **2018**, 11, 551-558.

64. Holdcroft, S.; Wright, A.; Britton, B, Weissbach, T.; Peckham, T. J.; Ward, J. W. *US Patent* **2019**, 2019/0382353 A1.

65. Huang, T.; He, G.; Xue, J.; Otoo, O.; He, X.; Jiang, H.; Zhang, J.; Yin, Y.; Jiang, Z.; Douglin, C. J.; Dekel, D. R.; Guiver, M. D. Self-crosslinked blend alkaline anion exchange membranes with bi-continuous phase separated morphology to enhance ion conductivity, *J. Membr. Sci.*, **2020**, 597, 117769.

66. Zhang, X.; Cao, Y.; Zhang, M.; Wang, Y.; Tang, H.; Li, N. Olefin metathesis-crosslinked,

bulky imidazolium-based anion exchange membranes with excellent base stability and mechanical properties, *J. Membr. Sci.*, **2020**, 598, 117793.

67. Liu, L., Chu, X., Liao, J., Huang, Y., Li, Y., Ge, Z., Hickner, M. A., Li, N. Tuning the properties of poly(2,6-dimethyl-1,4-phenylene oxide) anion exchange membranes and their performance in H_2/O_2 fuel cells, *Energy Environ. Sci.*, **2018**, 11, 435-446.

Figure caption

Scheme 1 Schematic illustration of conducting/non-conducting two-phase system

Scheme 2 Preparation procedure for AEMs

Figure 1 Plots of (a) OH^- conductivities (σ_{OH^-}); (b) WU; (c) hydration number (λ_w) at RT as a function of effective IEC_{exp}

Figure 2 Time-dependence of relative OH^- conductivity (σ_t/σ_0) of AEMs with different IECs after immersion in a 1-M KOH solution at 80°C

Figure 3 SANS profiles measured for AEMs with different IECs (a) at dry condition and (b) equilibrated in D_2O at room temperature. The vertical dashed line indicates the boundary between two *q*-Regions. (c) Plot of d_2 as a function of IEC

Figure 4 Schematic illustrations of the structure model for the ideal two-component system (a) "reverse-micelles", and (b) "micelles"

Figure 5 Highlighted SANS profiles (symbols) in Region II of Figure 3(b) for AEMs with different IECs. The best-fitted theoretical profiles (solid line), which are based on the HS-liquid model analysis, are also shown in the figure.

Figure 6 Porod plot of SANS profiles shown in Figure 3(b)

Figure 7 Plots of (a) V_S, V_w, and V_{graft}; (b) R_S, $R_{Porod,w}$, and $R_{Porod,g}$; and (c) S and n_{ion}, as a function of GD. The regions marked with dotted circles indicate good consistency of V_S with V_w or V_{graft} (part a), and of R_S with $R_{Porod,w}$ or $R_{Porod,g}$ (part b) to verify the applicability of "reverse-micelles" or "micelles" models.

Figure 8 Schematic illustrations of the structure models in the conducting phase of (a) "reverse-micelles" model for AEMs with IEC < IEC_c; (b) "micelles" model for AEMs with IEC > IEC_c; and the correlations of water uptake and membrane alkaline stability in the structure models of (c) "reverse-micelles" and (d) "micelles"

Figure 9 Performance tests of MEA fabricated with AEM42 as a membrane, and AEM98 as an ionomer: (a) Polarization curve and power density at 80°C, 100 mL/min oxygen

flow rate, and 20 mL/min hydrazine hydrate with 10 KPa backpressure at the cathode side; (b) OCV-hold test at 80°C, 100 mL/min oxygen flow rate, and 20 mL/min hydrazine hydrate without backpressure

Table 1 Characteristics of AEMs equilibrated in water at 25°C

AEMs	Grafting time (h)	GD (%)	WU (%)	λ_w	IEC_{cal} (mmol/g)	IEC_{exp} (mmol/g)	IEC_{exp} /IEC_{cal}	σ_0 (mS/cm) 60°C RT		Time of σ_t /σ_0 ~ 20% (h)
AEM08	0.67	8	5.0	10.6	0.34	0.26	0.76	17	9	>600[1)]
AEM11	0.8	11	7.5	11.2	0.45	0.37	0.82	23	12	>600[1)]
AEM14	1.0	14	9	11.6	0.56	0.43	0.77	39	18	>600[1)]
AEM18	1.2	18	10	10.3	0.63	0.54	0.85	50	24	>600[1)]
AEM30	2.0	30	20	14.4	1.0	0.78	0.78	60	43	450
AEM42	4.0	42	42	24.6	1.15	0.95	0.83	97	56	320
AEM56	5.0	56	53	22.9	1.54	1.29	0.84	116	78	200
AEM86	10.0	86	74	26.8	1.8	1.53	0.85	156	92	< 72[1)]
AEM98	16.0	98	80	25.8	1.88	1.72	0.91	181	100	< 72[1)]

[1)] AEM08, AEM11, AEM14 and AEM18 did not show visible conductivity decrease during the durability test up to 600h. AEM86 and AEM98 were physically damaged after immersing in 1 KOH solution at 80 °C for 3 days.

Table 2 d_2, ϕ_x of component x (x: graft, c-graft, and nc-graft) and V_w of AEMs equilibrated in water

AEMs	d_2 (Å)	ϕ_{graft}	$\phi_{c\text{-}graft}$[2)]	$\phi_{nc\text{-}graft}$[2)]	$\phi_{c\text{-}graft}$ /ϕ_{graft}	ϕ_{ETFE}	ϕ_w	V_{w1}	V_{w2}
AEM08	21.0	0.111	-	-	-	0.814	0.075	-	0.43
AEM11	21.0	0.141	-	-	-	0.753	0.106	-	0.44
AEM14	21.0	0.169	0.133	0.036	0.79	0.708	0.123	0.45	0.45
AEM30	22.0	0.261	-	-	-	0.513	0.226	-	0.50
AEM42	22.5	0.262	0.238	0.024	0.9	0.367	0.371	0.61	0.63

AEM56	23.4	0.284	-	-	-	0.298	0.418	-	0.62
AEM86	26.1	0.304	0.275	0.029	0.9	0.208	0.488	0.64	0.65

[2)] $\phi_{c\text{-graft}}$ and $\phi_{nc\text{-graft}}$ are obtained from eqs. (S1)–(S4) in the Supporting Information

Table 3 R_S and V_S, obtained from the hard-sphere liquid model, and estimated V_w and V_{graft}

AEMs	R_S (Å)	V_S	V_w[3)]	V_{graft}
AEM08	10.2	0.33	0.43	0.57
AEM11	10.5	0.39	0.44	0.56
AEM14	10.7	0.41	0.45	0.55
AEM30	11.0	0.38	0.50	0.50
AEM42	11.2	0.40	0.61	0.39
AEM56	11.6	0.40	0.62	0.38
AEM86	12.6	0.36	0.64	0.36

[3)] Average value of V_{w1} and V_{w2} for AEM14, AEM42 and AEM86, and the value of V_{w2} for other AEMs shown in Table 3

Table 4 Parameters obtained from the Porod limit analysis

AEMs	$R_{Porod,w}$ (Å)	$R_{Porod,g}$ (Å)	Σ(Å^{-1})	S (Å^2)	n_{ion}
AEM08	11.9 Yes[4)]	-	0.019	81	22
AEM11	11.8 Yes[4)]	-	0.027	84	21
AEM14	11.7 Yes[4)]	-	0.032	89	19
AEM30	-	-	0.029	93	-
AEM42	25.2 No[4)]	14.8 Yes[4)]	0.044	86	32
AEM56	23.8 No[4)]	14.6 Yes[4)]	0.053	87	31
AEM86	26.3 No[4)]	14.2 Yes[4)]	0.056	90	28

[4)] Consistency with HS liquid model.

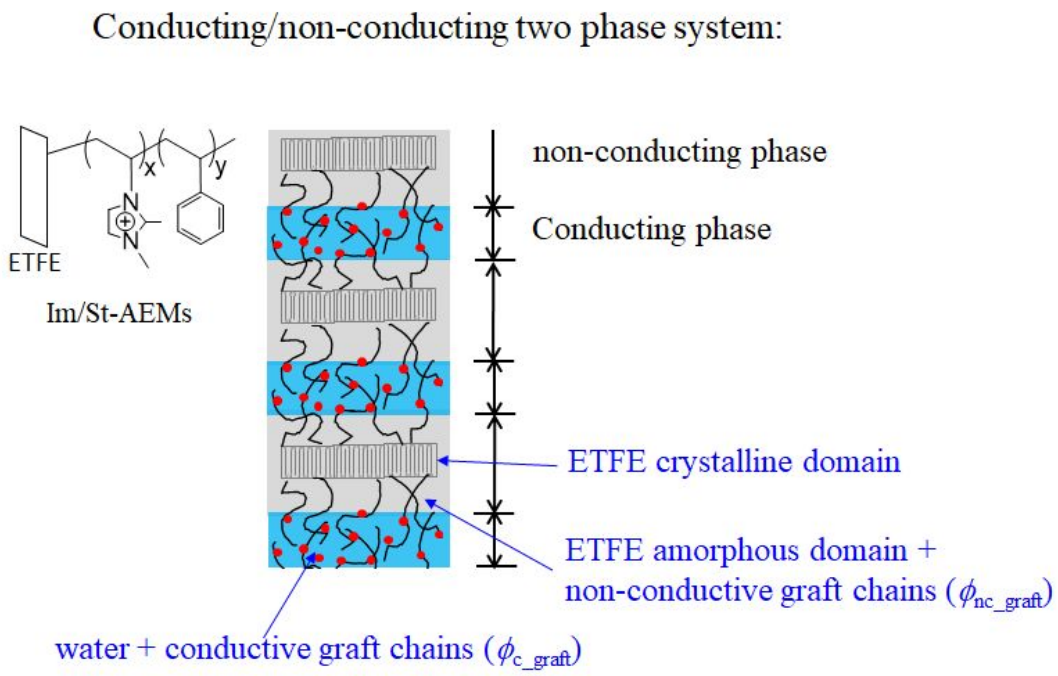

Scheme 1

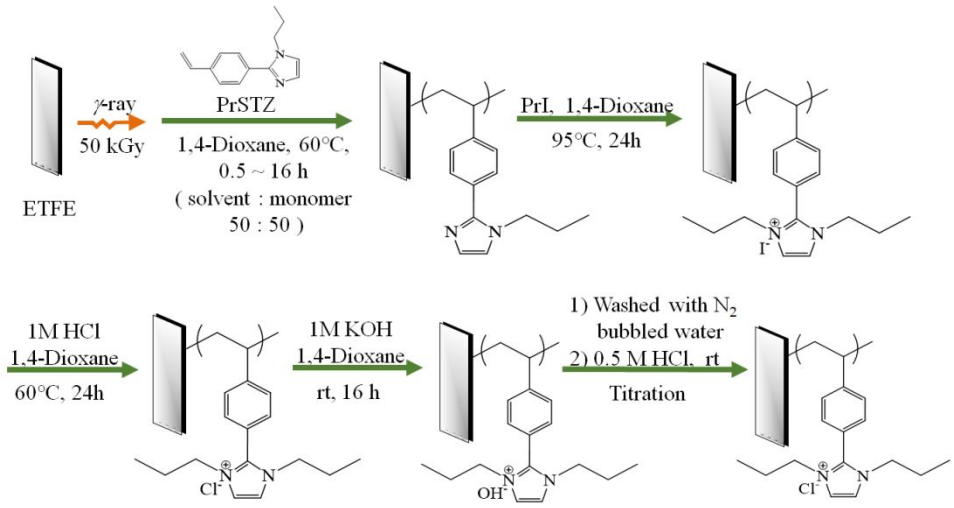

Scheme 2

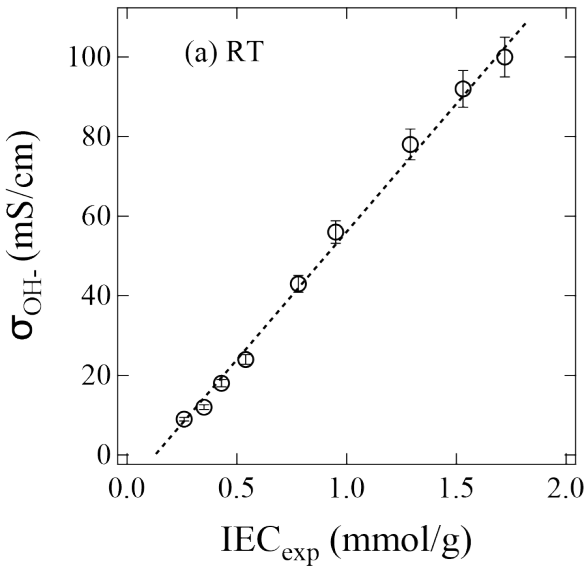
(a) RT
σ_{OH^-} (mS/cm)
IEC_{exp} (mmol/g)

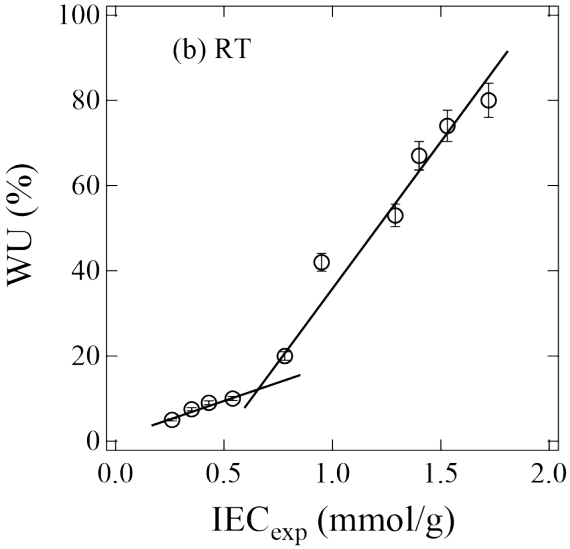
(b) RT
WU (%)
IEC_{exp} (mmol/g)

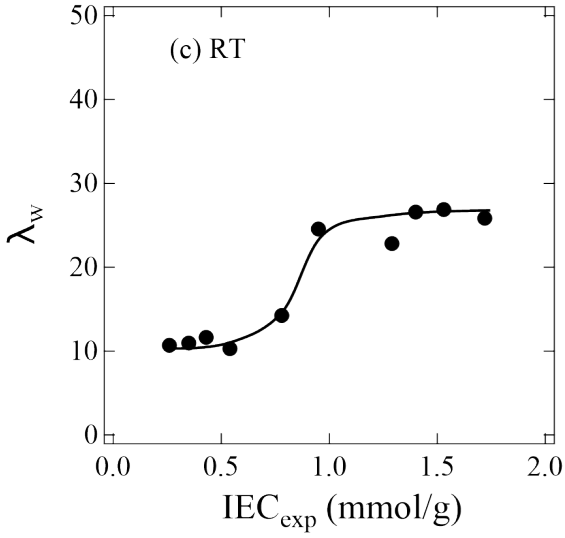
(c) RT
λ_w
IEC_{exp} (mmol/g)

Figure 1

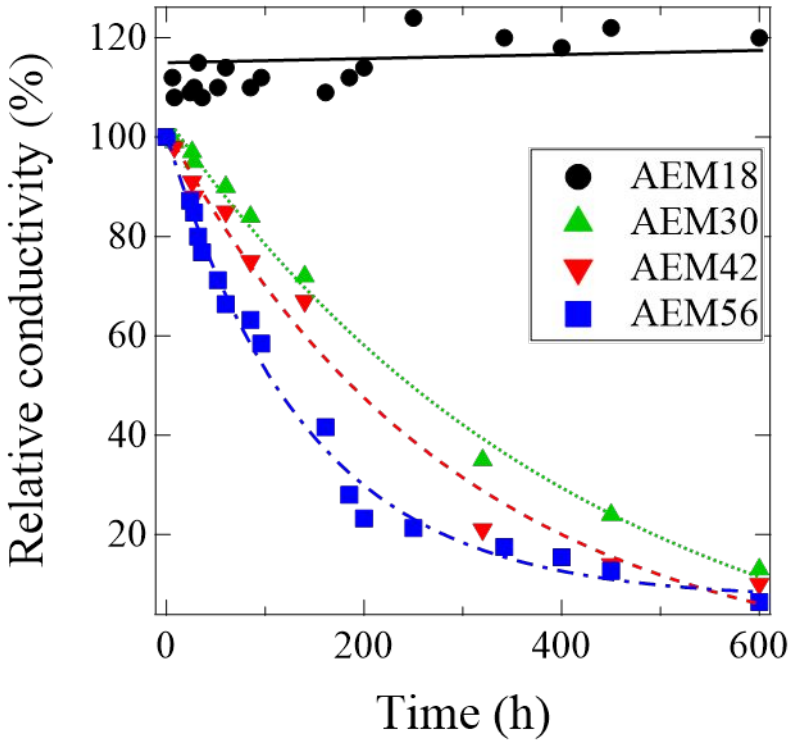
Relative conductivity (%)
120
100
80
60
40
20
0
200
400
600
Time (h)
AEM18
AEM30
AEM42
AEM56

Figure 2

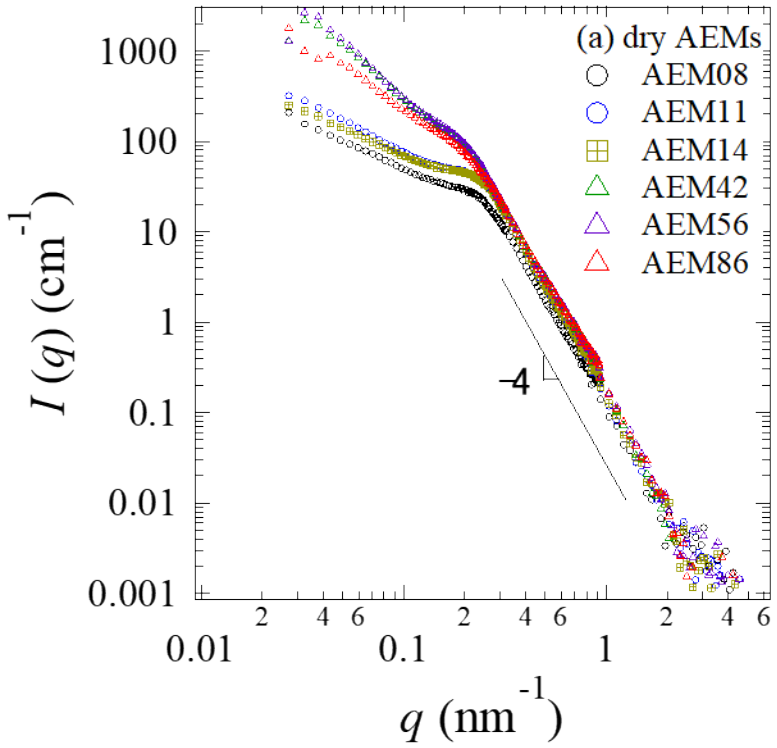
(a) dry AEMs
AEM08
AEM11
AEM14
AEM42
AEM56
AEM86
-4
I (q) (cm-1)
q (nm-1)
1000
100
10
1
0.1
0.01
0.001
0.01
0.1
1

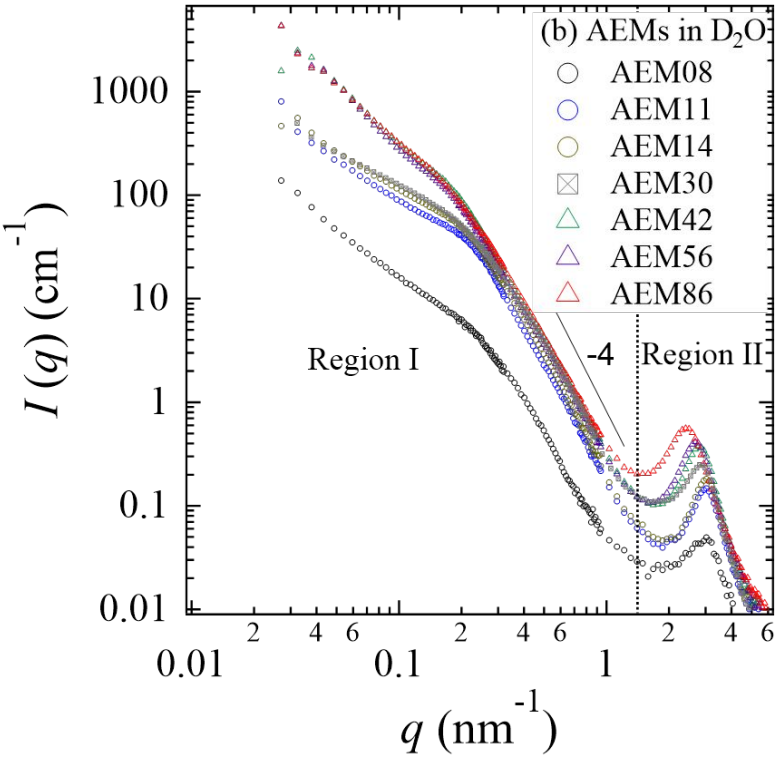
(b) AEMs in D2O
AEM08
AEM11
AEM14
AEM30
AEM42
AEM56
AEM86
Region I
-4
Region II
I (q) (cm-1)
q (nm-1)
1000
100
10
1
0.1
0.01
0.01
0.1
1

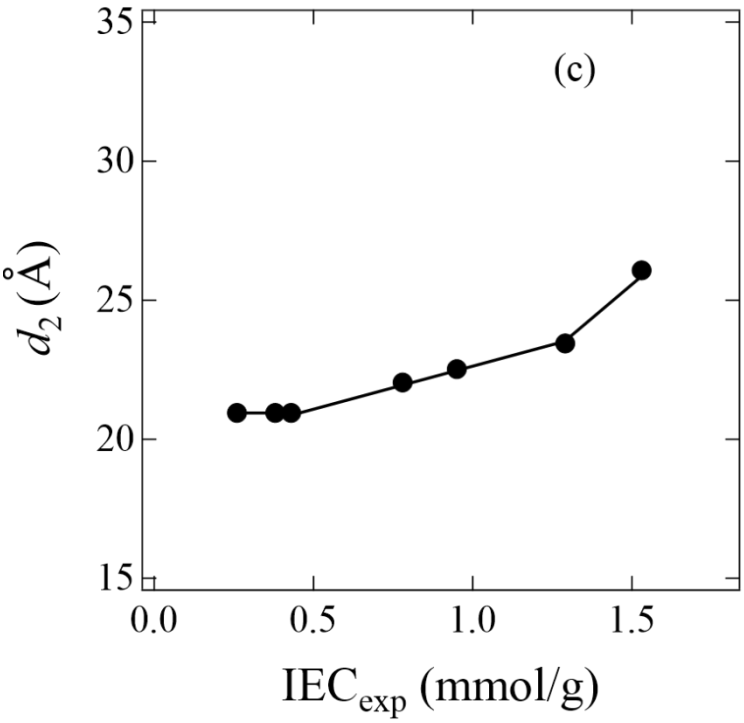

Figure 3

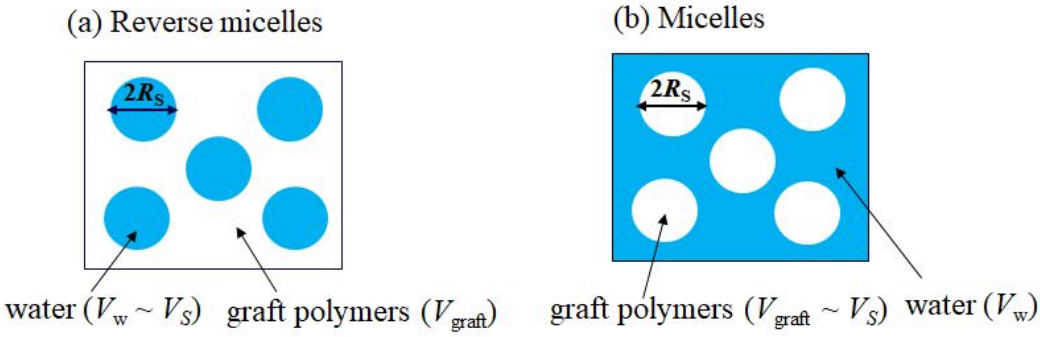

Figure 4

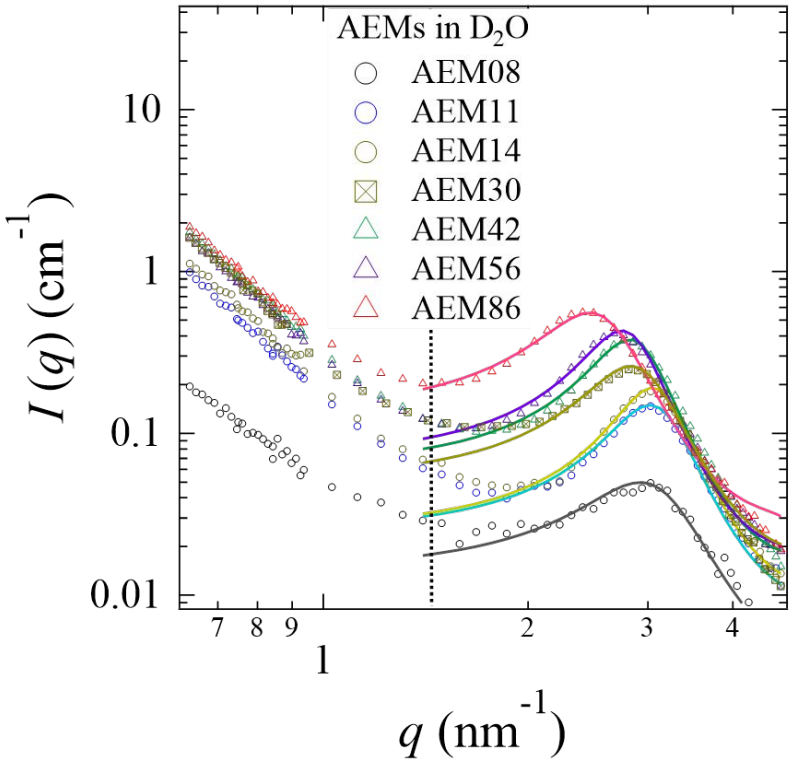
AEMs in D2O
AEM08
AEM11
AEM14
AEM30
AEM42
AEM56
AEM86
10
1
0.1
0.01
I (q) (cm-1)
7 8 9
1
2
3
4
q (nm-1)

Figure 5

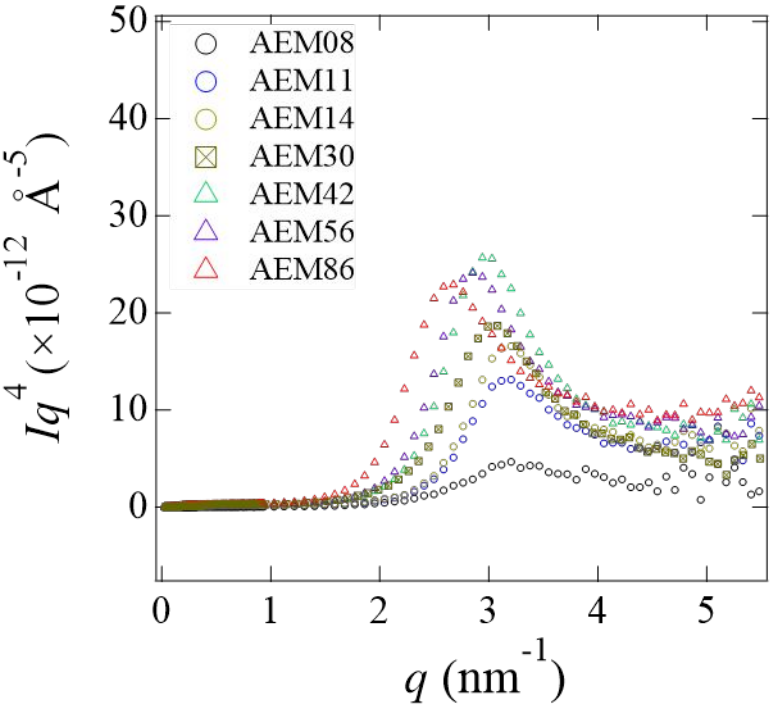
AEM08
AEM11
AEM14
AEM30
AEM42
AEM56
AEM86
Iq^4 ($\times 10^{-12}$ Å^{-5})
q (nm^{-1})
0
10
20
30
40
50
0
1
2
3
4
5

Figure 6

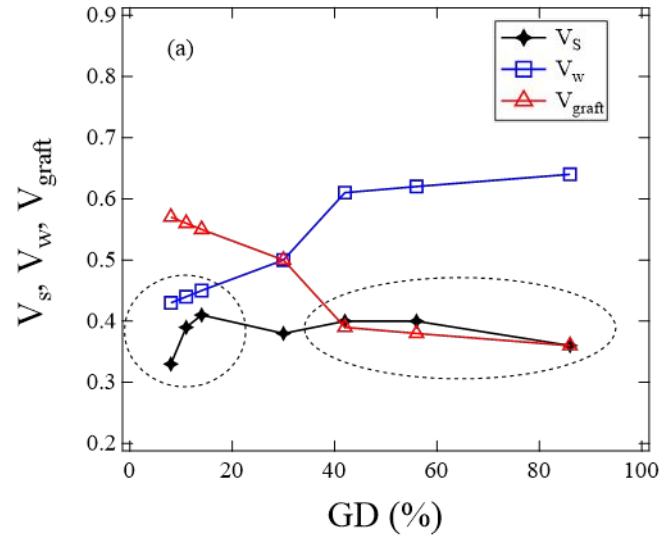
(a)
V_S
V_w
V_{graft}
V_S, V_w, V_{graft}
GD (%)

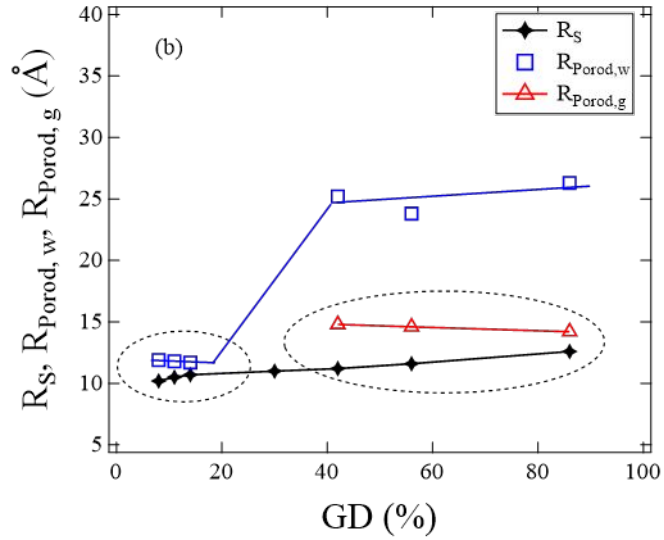
(b)
R_S
$R_{Porod,w}$
$R_{Porod,g}$
R_S, $R_{Porod,w}$, $R_{Porod,g}$ (Å)
GD (%)

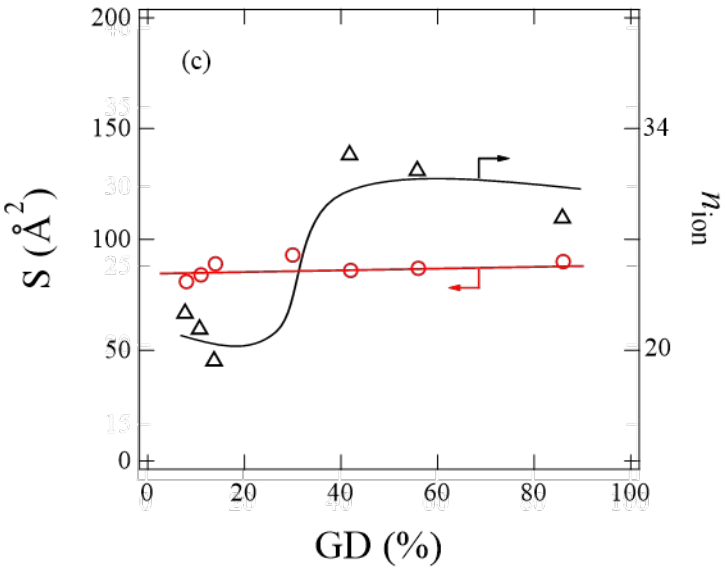
(c)
S (Å^2)
η_{ion}
GD (%)

Figure 7

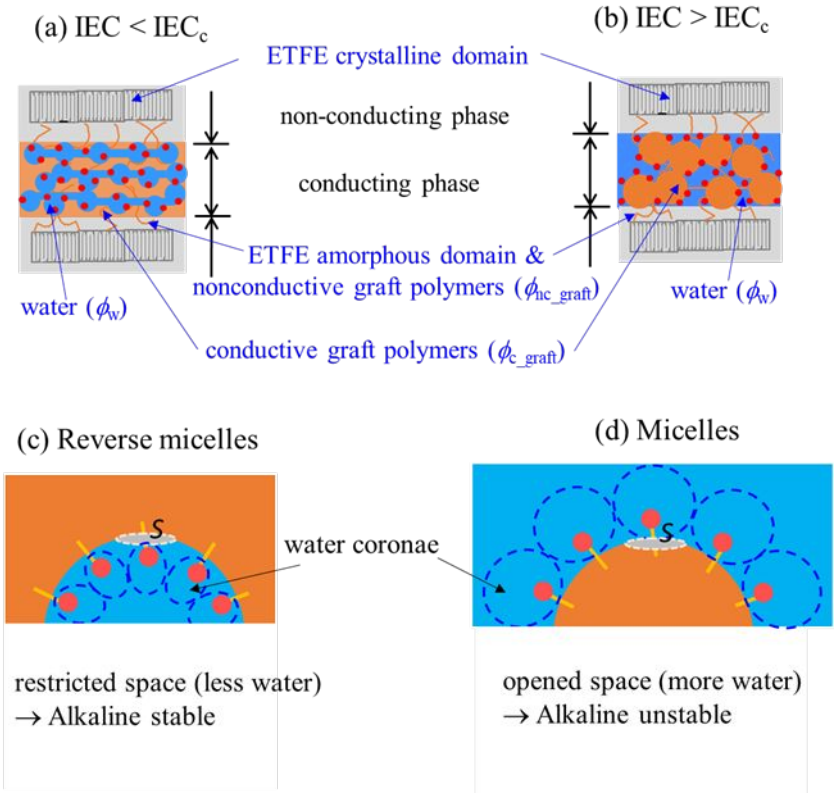
(a) IEC < IEC$_c$
(b) IEC > IEC$_c$
ETFE crystalline domain
non-conducting phase
conducting phase
ETFE amorphous domain &
nonconductive graft polymers (ϕ_{nc_graft})
conductive graft polymers (ϕ_{c_graft})
water (ϕ_w)
water (ϕ_w)
(c) Reverse micelles
(d) Micelles
water coronae
S
S
restricted space (less water)
→ Alkaline stable
opened space (more water)
→ Alkaline unstable

Figure 8

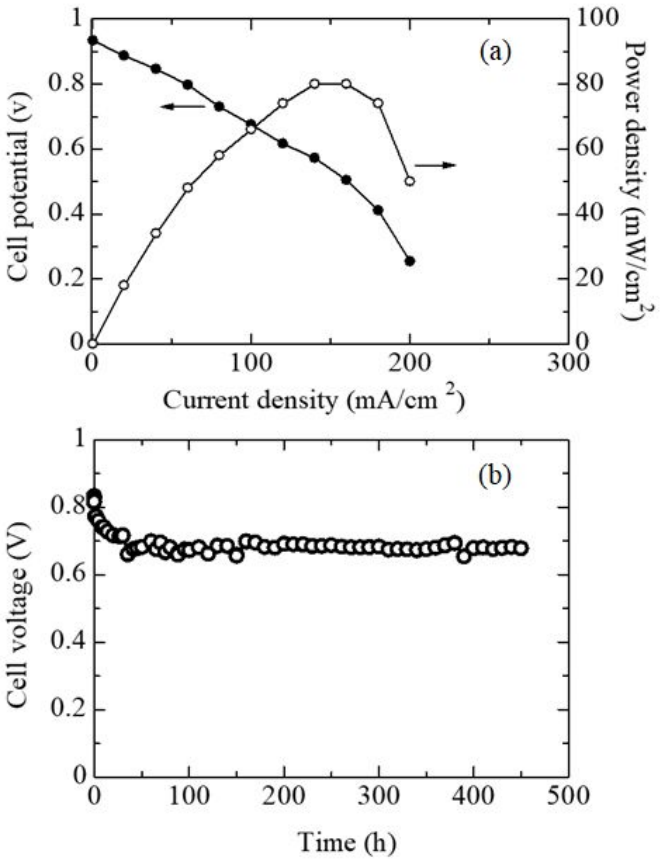
(a)
Cell potential (v)
Power density (mW/cm^2)
Current density (mA/cm ^{2})
0
0.2
0.4
0.6
0.8
1
0
20
40
60
80
100
0
100
200
300
(b)
Cell voltage (V)
Time (h)
0
100
200
300
400
500

Figure 9

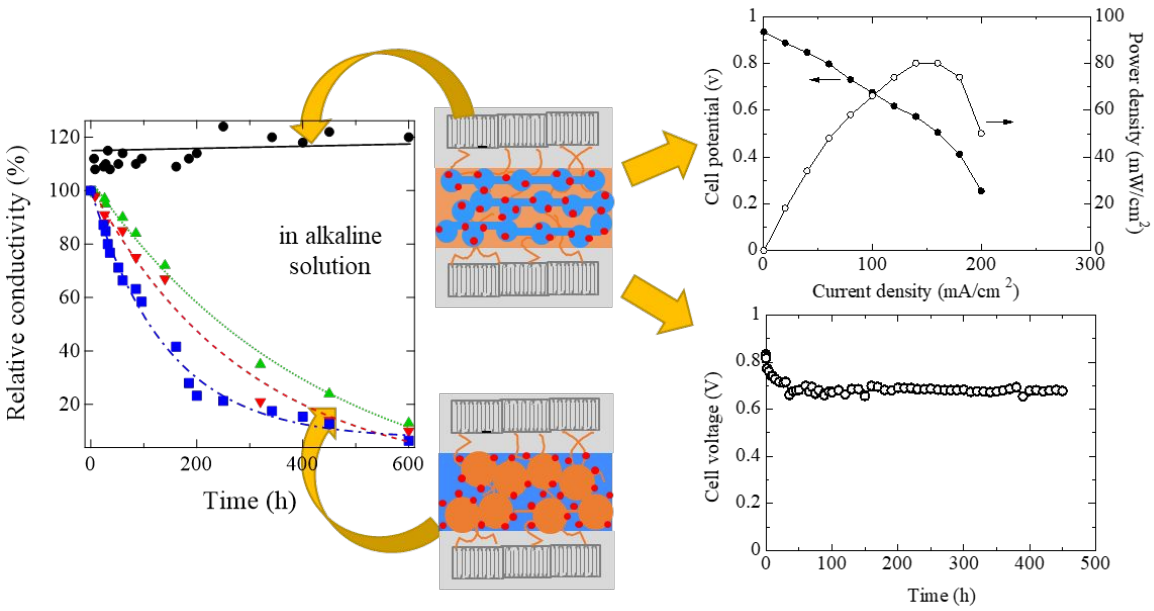

Structure-property relationships of newly developed AEMs were studied. Hydrazine-hydrate fuel cell tests show good performance and thus far best durability.